EXPERIMENTAL INVESTIGATION OF TURBULENT FLOW IN A PIPE BEND USING PARTICLE IMAGE VELOCIMETRY

EXPERIMENTAL INVESTIGATION OF TURBULENT FLOW IN A PIPE BEND USING PARTICLE IMAGE VELOCIMETRY

By

AKSHAY JAIN, B.TECH

B.Tech (Indian Institute of Technology, Jodhpur, India)

A Thesis

Submitted to the School of Graduate Studies

In Partial Fulfillment of the Requirements

For the Degree

Master of Applied Science

McMaster University

Master of Applied Science (2017) McMaster University

(Mechanical Engineering) Hamilton, Ontario

TITLE:	Experimental Investigation of Turbulent flow in a Pipe Bend using Particle Image Velocimetry
AUTHOR:	Akshay Jain, B.Tech(IITJ)
SUPERVISOR(S):	Professor Chan Y. Ching
NUMBER OF PAGES:	xii, 133

Abstract

The turbulent flow through a 90° pipe bend is complex with secondary flow that can affect pressure drop and heat/mass transfer. The mean and unsteady flow is studied using refractive index matched two-dimensional two-component (2D2C) Particle Image Velocimetry in a single 90° bend with Rc/D = 1.5 and at Re = 34800. The measurements were performed in a closed loop using a 1-inch diameter test section that was machined out of acrylic. The flow is imaged in the symmetric plane parallel to the axial flow and at different cross sectional planes including 0.25D and 1D upstream, 10°, 20°, 70°, 80° from the bend inlet and 0.25D and 1D downstream of the bend.

The axial flow accelerates on the inner wall at the inlet and then moves towards the outer wall at 40°-50°. A shear layer is formed between high velocity fluid near the outer wall and the slower moving fluid at the inner wall side in the second half of the bend. The axial turbulent kinetic energy $(\overline{u^2} + \overline{v^2})$ is found to be high in regions corresponding to high velocity gradient regions: (i) at the outer wall near the inlet that extends up to the outlet, (ii) near the inner wall at 40°-50°, and (iii) at the shear layer formed near the inner wall. In the cross sectional planes, two vortices are formed and have a maximum strength at 80° from the bend inlet. The cross sectional turbulent kinetic energy $(\overline{v^2} + \overline{w^2})$ is found to be highest on the inner wall at the 80° plane.

The snapshot Proper Orthogonal Decomposition (POD) technique is used to study the unsteady flow structures within the flow. There are long and short flow structures in the upstream pipe which can be related to Very Large Scale and Large Scale Motions. The secondary flow at 20° and further downstream cross sectional planes show evidence of unsteadiness as two vortices oscillate about the symmetry axis with low frequencies of St ~ 0.07, 0.13 and higher frequency at St ~ 0.3-0.6. The low frequency oscillations can be related to Very Large Scale Motions while high frequency oscillations are related to separation of the flow on the inner wall side. Evidence of swirl switching in the high frequency range (St ~ 0.3-0.5) is found at cross sectional plane 1D downstream.

Acknowledgements

I would like to express gratitude towards my supervisor Dr. Chan Ching for providing me opportunity to work on independent experimental research work. Dr. Ching's support and faith in me throughout the period helped a lot for completion of this work. I would also like to thank Dr. Ewing for his technical guidance at each and every step of the research. I appreciate his dedication and perfection towards the research. The weekly discussion with him helped in learning new aspects of fluid mechanics and expand my knowledge.

I would take this opportunity to thank Dr. Cotton and members of TMRL group for their suggestions during weekly meetings and for bringing the positivity in the lab. I greatly appreciate the help and guidance provided by Mechanical Engineering department technicians while machining and setting up the experiments. I would also like to thank Dr. Fang and Eric Mahoney for providing optical accessories.

Lastly, I would like to thank my parents and family for supporting me in my every decision.

Table of Contents

List of Tables

List of Figures

Nomenclature

U	Local instantaneous axial velocity
V	Local instantaneous transverse/ radial velocity
W	Local instantaneous circumferential velocity
$\bar{U}$	Mean axial velocity
$\bar{V}$	Mean transverse/ radial velocity
u	Axial fluctuations
v	Transverse fluctuations
u'	RMS of axial fluctuations
v'	RMS of transverse fluctuations
U_o	Bulk velocity
U_c	Centerline velocity
t	Instantaneous time
X	Axial direction
R	Radius of the bend
D	Diameter of the bend (2R)
Rc	Radius of curvature of the bend
τ	Dimensionless time
Φ	Bend angle
St	Strouhal Number
Re	Reynolds Number
ρ	Density
μ	Dynamic viscosity
ν	Kinematic viscosity
M	magnification
pix	Pixels
d_i	Interrogation spot size
U_r	Reconstructed velocity

Symbols

B	Eigen vector
Λ	Eigen value
ψ	Modes
C	Correlation matrix of fluctuations
c	POD mode coefficients
I	Total number of grid points in horizontal direction
J	Total number of grid points in vertical direction
K	Total number of time instants/snapshots
M	Total number of modes
P	Number of modes used for reconstruction
N	Total number of valid realization at any spatial location

Chapter 1. Introduction

Flow in pipe bends is ubiquitous in many thermal engineering systems, such as in oil and gas piping systems, power generation plants and HVAC systems. Understanding and modeling the flow is important to determine the pressure drop and heat/mass transfer in pipe bends, which are of significant engineering interest. For example, the pipe wall thinning due to Flow Accelerated Corrosion (FAC) commonly observed in power generation plants is directly related to the wall mass transfer of the Ferrous ions. The pressure drop and heat/mass transfer is enhanced in pipe bends relative to that in a straight pipe. The flow in bends is complex and inherently unsteady, with strong secondary flows. The unsteadiness in the flow can also lead to flow induced vibrations and resultant mechanical fatigue of the piping system and failure.

Secondary flows in the form of two counter rotating vortices are developed as the flow passes through a 90° bend. This is due to the centrifugal forces which drive the flow in the core region towards the outer wall of the bend. The flow is driven back towards the inner wall due to the resultant pressure gradient, thus resulting in counter rotating vortices within the cross section of the bend. There can also be flow reversal and separation along the inner wall due to the adverse pressure gradient that develops in the second half of the bend. The strength of the secondary flows and the flow separation will depend on a number of parameters, such as the radius of curvature of the pipe bend and Reynolds number. When the flow is turbulent, a phenomenon referred to as “swirl switching” has been observed. In this instance, a single swirl is observed downstream of the bend, where the direction of rotation changes periodically. This phenomenon and the resulting turbulent flow field within the bend is not fully understood.

The objective of this thesis is to experimentally investigate the flow field, in particular the swirl switching phenomenon, within a 90° bend with a radius of curvature of 1.5 times the diameter. Heretofore, this phenomenon has been studied by performing measurements downstream of the bend, with no measurements available within the bend.

Therefore, the secondary flow at cross sectional planes (10°, 20°, 70° and 80°) within the bend is captured using refractive index matched time-resolved 2-dimensional 2-component (2D2C) Particle Image Velocimetry (PIV). The experiments were performed in a closed flow loop using a test section fabricated from acrylic and a 64.2 percentage by weight solution of Sodium Iodide as the working fluid at a Reynolds number of 34800. The flow field measurements were obtained on the axial plane and at several cross sectional planes upstream and downstream of the bend, in addition to those within the bend.

The snapshot Proper Orthogonal Decomposition (POD) technique was used to identify the structures within the flow. The POD technique represents the flow field with a series of modes that are arranged in decreasing order of energy content. The power spectra of POD coefficients are considered to characterize the frequencies associated with each mode/structure. Low order reconstructions of velocity and fluctuations with a limited number of the modes are used, to understand the dynamics of the large scale motions.

This thesis consists of 5 chapters, including this introductory chapter. A comprehensive literature review on the mean and unsteady flow in pipe bend is given in Chapter 2. This is followed by Chapter 3 that provides details of the experimental facility, methodology and data reduction procedures. The results are presented and discussed in Chapter 4. Finally, Chapter 5 presents the conclusions and recommendations for future work.

Chapter 2. Literature Review

Investigations of flow through 90° pipe bends have considered a number of different factors including the pressure drop through the bend, the heat and mass transfer in the bend and the mean and unsteady flow in the bend. In this chapter, previous research on these topics is reviewed and important studies are summarized in Table 2.1.

2.1. Pressure Loss in 90° Bends

The flow through pipe bends results in a relatively higher pressure drop compared to that in straight pipes. Pressure loss through pipe bends was found to be largely affected by the radius of curvature of the bend (Yarnell 1937; Beij 1938; Weske 1943; Itō 1960; Miller 1971; Spedding, Benard, and Mcnally 2004; Crawford, Cunningham, and Spence 2007). In a single 90° bend, Miller (1971) identified four ranges of curvature ratio (Rc/D) on the basis of the pressure losses. In the first region of Rc/D < 0.8, there is a flow separation at the inner wall and losses here are the result of flow expansion just after the bend. For bends in the range 0.8 < Rc/D < 1.5, most of the losses occur in the bend and 1D downstream of the bend. In bends with 1.5 < Rc/D < 3.0, about 40 percent of the losses occur in the downstream pipe. For the bends with Rc/D > 3.0, the main loss is due to increased wall friction in the bend and losses in the downstream pipe are a small percentage of total loss. The minimum pressure loss was found to occur for Rc/D = 2.5 (Itō 1960; Crawford, Cunningham, and Spence 2007). Crawford et al. (2003) proposed an equation for predicting losses due to separation for the low Rc/D ratios. The pressure loss coefficient was found to have little dependence on Reynolds number in the turbulent region (Beij 1938; Itō 1960; Spedding, Benard, and Mcnally 2004).

The flow in a bend experiences centrifugal force due to curvature which results in redistribution of the pressure within the bend. A typical pressure distribution along the inner, outer and side walls of the bend from Itō et al. (1960) is shown in Figure 2.1. The pressure along the outer wall increases due to turning of the flow while it decreases on

the inner wall, resulting in axial pressure gradients. (Itō 1960; Spedding, Benard, and Mcnally 2004; Sudo, Sumida, and Hibara 1998; El-Gammal et al. 2010). Dutta et al. (2015) found from numerical simulation that the pressure coefficient on the inner wall decreases slightly up to Re = 3 x 10^5 and then remains constant for higher Reynolds number while at the outer wall side it slightly increases with Reynolds number. The pressure drop coefficient was found to decrease and increase on the outer and inner walls respectively up to Rc/D = 2 and remained essentially constant for higher curvature ratios.

2.2. Heat and Mass Transfer in 90° Bends

The heat and mass transfer in pipe bends have importance in various industrial applications. The total heat and mass transfer within the bend is higher than in a straight pipe (Achenbach 1976; Coney 1981; Wilkin, Oates, and Coney 1983; Chrysler and Sparrow 1986; Poulson 1993; Mazhar et al. 2013). The difficulty in measuring local heat transfer in a bend was overcome by measuring local mass transfer and using the analogy between the two (Chrysler and Sparrow 1986; Ohadi and Sparrow 1989). The mass transfer in pipe bends is important in applications such as pipe wall thinning due to Flow Accelerated Corrosion (FAC) in power plant piping systems (Poulson 1999; El-Gammal et al. 2010; Ahmed 2010; Mazhar 2013; Lin and Ferng 2014; Ikarashi et al. 2017). The mass transfer in a 90° pipe bend depends on various parameters including curvature ratio (Rc/D), Reynolds number (Re), Schmidt number (Sc), and surface roughness. The mass transfer enhancement, defined as the ratio of local Sherwood number to the Sherwood number in a fully developed pipe flow, was found to increase with decreasing curvature ratio and was attributed to higher turbulence in low Rc/D bends (Coney 1981; Bergstrom et al. 1998; J. Wang and Shirazi 2001). The mass transfer enhancement was found to be independent of Reynolds number for smooth walled bends (Poulson and Robinson 1988; Coney 1981; Mazhar et al. 2013) and scaled as $Re^{0.12}$ for rough walls (Poulson and Robinson 1988). However, Wang et al. (2001) showed an inverse relationship with Reynolds number in the correlation proposed using various CFD simulation results. Numerical simulation results also showed the mass transfer enhancement slightly decreased with Schmidt number (Sc) (Bergstrom et al. 1998; J. Wang and Shirazi 2001).

Within the bend, the maximum local mass transfer location was found to be on the outer wall at the bend outlet and extending to some distance downstream (Achenbach 1976; Wilkin, Oates, and Coney 1983; Mazhar et al. 2013). Two additional higher mass transfer locations were identified: (a) on the inner wall at the bend inlet and (b) on the side walls near the inner wall in the middle of the short radius bends (Rc/D = 1.5) (Achenbach 1976; Wilkin, Oates, and Coney 1983; El-Gammal et al. 2010; Mazhar et al. 2013). Achenbach et al. (1976) reported a decrease in mass transfer coefficient on the inner wall side at inlet for low Reynolds numbers ($Re < 1.4 \times 10^5$) which was also seen by Wilkin et al.(1983) at $Re = 0.08 - 6.5 \times 10^5$ and Ikarashi et al.(2017) at $Re = 0.5 \times 10^5$. The lower enhancement on the inner wall at low Reynolds numbers was attributed to shift of point of separation upstream for low Reynolds number. However, Mazhar et al. (2013) reported local mass transfer enhancement on the inner and outer walls that was independent of Reynolds number in the range $Re= 0.4 – 1.3 \times 10^5$. This was attributed to surface roughness and high Schmidt (Sc) number in their experiments. The wear patterns inside the bend were found as streaks directed towards centerline whereas the streaks on the outer wall at the bend outlet were directed in the axial direction, suggesting a strong role of the secondary flow in the mass transfer in bends (Wilkin, Oates, and Coney 1983; El-Gammal et al. 2010; Mazhar et al. 2013; Ikarashi et al. 2017).

2.3. Mean flow and Turbulent Stresses in Pipe Bends

The mean flow field within 90° bends have been studied experimentally using hot wire anemometry (HWA), Laser Doppler Velocimetry (LDV) and Particle Image Velocimetry (PIV) (Enayet et al. 1982; Sudo, Sumida, and Hibara 1998; Ono et al. 2011; Kalpakli 2012; Mazhar et al. 2016; Ikarashi et al. 2017) and numerically using RANS based models, LES and DES (Al-Rafai, Tridimas, and Woolley 1990; Rütten, Schröder, and Meinke 2005; Tanaka 2009; El-Gammal et al. 2010; Eguchi et al. 2011; Tan et al. 2014; J. Kim, Yadav, and Kim 2014; Röhrig, Jakirlić, and Tropea 2015; Y. Wang, Dong, and Wang 2015; S. Wang et al. 2016; Dutta et al. 2016) . There have also been several studies on 180° bends (Rowe 1970; Azzola et al. 1986; Anwer, So, and Lai 1989; Sudo, Sumida, and Hibara 2000; Lee, Choi, and Han 2007). The flow characteristics in a 180°

bend was found to be similar to that in a 90° bend up to about 60-70° from the bend inlet (Sudo, Sumida, and Hibara 2000).

The axial flow in a pipe bend accelerates near the inner wall at the inlet due to the favorable pressure gradient. This results in a shift of high velocity towards the inner wall side which remains until a bend angle of about 30° (Enayet et al. 1982; Sudo, Sumida, and Hibara 1998; Mazhar et al. 2016). The flow, however, experiences deceleration on the outer wall due to adverse pressure gradient and may have separation or recirculation for sharp bends (Achenbach 1976; Rütten, Schröder, and Meinke 2005). In the second half of the bend, the axial flow experiences an adverse pressure gradient on the inner wall resulting in deceleration and flow separation depending on the curvature ratio. Ono et al. (2011) reported a constant flow separation for Rc/D = 1.0 and an intermittent separation for Rc/D = 1.5 at Re=1.8-5.4 x 10^5 while Sudo et al. (1998) reported no flow separation on the inner wall for a bend with Rc/D = 2.0. The numerical LES results by Tan et al. (2014) found a similar effect of curvature ratio on the flow. The flow in a bend with Rc/D = 1 was found to have separation both in Reynolds averaged and instantaneous flow while for a bend with Rc/D = 2 there was a very weak separation on the inner wall at some instance and no separation in the Reynolds averaged flow. The high velocity flow was shifted towards the outer wall side and remained on the outer wall in the downstream pipe. The secondary flow in pipe bends was studied by (Azzola et al. 1986; Fiedler 1997; Sudo, Sumida, and Hibara 1998; El-Gammal et al. 2010; Mazhar et al. 2016; Sudo, Sumida, and Hibara 2000). Sudo et al.(1998) and Tan et al. (2014) found that the secondary flow was directed towards the inner wall at the inlet cross sectional plane due to the presence of a cross sectional pressure gradient. Further downstream, at the 30° plane, two counter rotating vortices were formed with flow in the central region directed outwards and that near the side walls directed inwards (Azzola et al. 1986; Sudo, Sumida, and Hibara 1998; Tan et al. 2014). The secondary flow in the form of two counter rotating vortices strengthened until the bend outlet and then weakened in the downstream pipe (Sudo, Sumida, and Hibara 1998; Tan et al. 2014; J. Kim, Yadav, and Kim 2014; Y. Wang, Dong, and Wang 2015). Tan et al. (2014) found the Reynolds averaged secondary

flow in a bend with Rc/D = 2.0 to be symmetric about the symmetry plane for all cross sections in and downstream of the bend while for Rc/D = 1.0, the secondary flow was found asymmetric in cross sectional plane 3 diameters downstream of the bend. This asymmetry in the secondary flow was attributed to the more complex flow in sharper bends due to separation that results in unsteadiness and oscillation of the two vortices (Rütten, Meinke, and Schröder 2001; Rütten, Schröder, and Meinke 2005; Tan et al. 2014). The effect of the Reynolds number on the flow was studied by (Tanaka 2009; Ono et al. 2011; Takamura et al. 2012; Dutta et al. 2016; Y. Wang, Dong, and Wang 2015). The flow separation location was found to move upstream and the reattachment location shifted downstream with increasing Reynolds number for a sharp bend with Rc/D =1 (Takamura et al. 2012; Dutta et al. 2016). Wang et al. (2015) reported a gap between the two vortices of the secondary flow and the inner wall at the 60° plane due to separation of the primary flow. This gap was found to reduce with increasing Reynolds number.

The turbulence intensities, turbulent kinetic energy and Reynolds stresses in pipe bends have been presented in the studies of (Enayet et al. 1982; Sudo, Sumida, and Hibara 1998; El-Gammal et al. 2010; Ono et al. 2011; Takamura et al. 2012; Tan et al. 2014; Röhrig, Jakirlić, and Tropea 2015; Mazhar et al. 2016; Dutta et al. 2016). The turbulent kinetic energy averaged over the whole cross section, was found to be maximum in between the bend outlet and 0.5 diameter downstream of the bend (Sudo, Sumida, and Hibara 1998; Y. Wang, Dong, and Wang 2015). The local axial turbulence intensity was found higher in areas of high axial velocity gradients ($\frac{dU}{dy}$), as near the outer wall at $\phi = 30^o$ and near the inner wall at $\phi = 60^o$ (Enayet et al. 1982; Sudo, Sumida, and Hibara 2000). The turbulence in the symmetry plane was found to be highest on the inner wall in the second half of the bend. Ono et al. (2011) reported high levels of turbulence intensity in the shear layer and on the inner wall for a sharp bend (Rc/D = 1) whereas for a long radius bend it was found only on the inner wall. Similarly, Tan et al. (2014) found the axial turbulence intensity on the inner wall to be sensitive to the curvature ratio. The turbulence intensity was found to increase slightly with Reynolds number but the location of maxima remains the same (Mazhar et al. 2016; Dutta et al. 2016). Takamura et al.

(2012) found that the cross sectional turbulent intensities were higher in the flow separated region near the inner wall at the bend outlet. The turbulence intensities becomes higher on the cross section plane 0.2 diameter downstream of the bend and suggested this was due to enhanced flow recovery in the downstream pipe. Dutta et al. (2016) reported an increase in transverse fluctuations on the symmetry plane at the bend outlet and shifting of the peak location towards the pipe center with increase in Reynolds number.

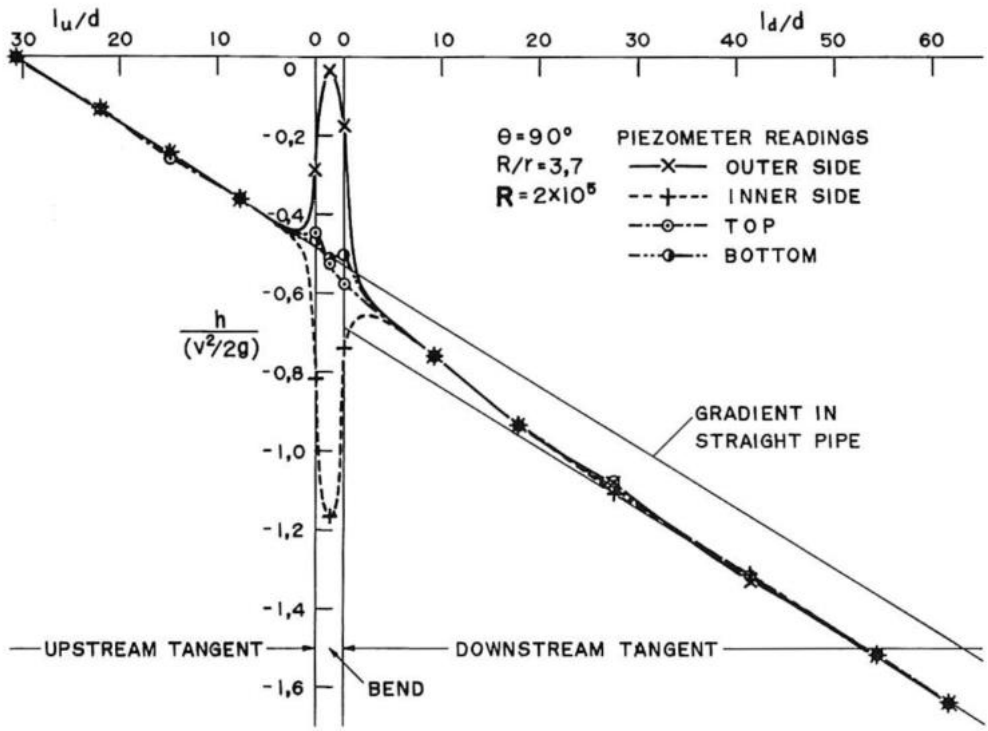

Figure 2.1 Typical pressure distribution along the bend with Rc/D = 1.85 (Itō 1960).

Author , Year	Quantity measured	Parameters	Technique Used	Observations
Pressure Loss				
(Yarnell 1937)	Pressure losses	Bend angles Configurations Cross sections Rc/D = 1.375 Re = 0.92 – 6.5 x 10^5	Piezometers	Losses depends on all the parameters and coefficients are tabulated for each case
(Beij 1938)	Pressure losses	Rc/D = 1-20 Re = 3-30 x 10^4	Differential Manometer	Minimum at Rc/D ~ 5. Small change with Reynolds number.
(Weske 1943)	Pressure losses Velocity	Cross sections, configurations, Rc/D = 0.75,1.5,4.0 Re = 2-8 x 10^5	Manometers	Rc/D is important parameter for pressure losses; Slight non uniform change with Reynolds number; Separation seen for the sharpest bends.
(Itō 1960)	Pressure losses	Bend angle, Rc/D = 1.0 – 7.3 Re = 0.2 – 4 x 10^4	Piezometers	Minimum coefficient at Rc/D = 2.5; Correlation for pressure loss depending on value of $Re(D/2Rc)^2$.
(Miller 1971)	Pressure losses			
(Coffield, Hammond, and Koczko 1998)	Pressure losses for high Reynolds number	Rc/D = 1.2 Re = 0.5-40 x 10^6	Differential Pressure cells	Pressure loss coefficients at high Reynolds number
(Spedding, Benard, and Mcnally 2004)	Pressure losses	Rc/D = 0.06 Re = 0.1-5 x 10^4	Manometer	Review of literature showed Dean number as important parameter Re_{cr}(bend) > Re_{cr}(str. Pipe) Correlation for pressure loss in elbow bends

(Crawford, Cunningham, and Spence 2007)	Pressure loss due to separation	Rc/D = 0.65, 2.5, 10 Re = 0.04 – 5 x 10^5	Strain Gauge transducers; dry capacitance cell transducers	Minimum pressure loss in bend with Rc/D = 2.5. Predicted new empirical relation for bend loss with separated flow.
(Dutta and Nandi 2015)	Pressure losses numerically	Rc/D = 1-5 Re =0.1 – 1 x 10^6	$RNG\ k-\epsilon$	Little change with Re;
Mass (Heat) Transfer				
(Achenbach 1976)	Mass transfer	Rc/D = 1.5 Re = 0.5- 4 x 10^5 Sc = 2.53	Naphthalene Sublimation technique	Maximum mass transfer is found on the outer wall side at 0.7D downstream of the bend. Low enhancement on inner wall at inlet for low Re (<1.4x10^5)
(Bergstrom et al. 1998)	Numerical prediction of mass transfer in 2D bend	Rc/D = 1, 1.5, 3 Re = 2 x 10^4, 10^5, 10^6 Sc = 500 - 5000	Low Reynolds number $k-\epsilon$	Effect of curvature on mass transfer decreases with increase in Rc/D; Slight decrease with Sc; Significant increase in mass transfer on inner wall for low Re = 20000;
(J. Wang and Shirazi 2001)	Mass transfer correlation using CFD	Rc/D = 0.5 – 10 Re = 2 x 10^4 - 10^7 Sc = 2.5 - 300	Low Reynolds number $k-\epsilon$	Proposed correlation for predicting maximum mass transfer coefficients (MTCRE) in elbows; MTCRE decreases slightly with Re, Sc, Rc/D for moderate Rc/d values.
(El-Gammal et al. 2010)	Mass transfer and flow simulation	Rc/D = 1.5 Re = 40000 Sc = 1280	Plaster Dissolution Reynolds Stress Model	Maximum wear on inner wall at inlet; Time evolution wear on inner and outer wall reported; Flow simulation reporting surface friction coefficient, TKE, primary and secondary flow.

(Mazhar et al. 2013)	Mass transfer	Rc/D = 1.5 Re = 0.4 – 1.1 x 10^5 Sc = 1280	Plaster Dissolution	Mass transfer enhancement found to be Re independent;
(Ikarashi et al. 2017)	Mass transfer and flow visualization and velocity measurements (SPIV)	Rc/D = 1.5 Re = 0.5 x 10^5 Sc = 680	Plaster Dissolution SPIV	Low enhancement on inner wall at inlet;
Flow Measurements and Simulations				
(Enayet et al. 1982)	Axial flow measurements	Rc/D = 2.8 Re = 500, 1093, 43000	Laser Doppler Velocimetry	Evolution of axial velocity and its fluctuations in the 90° bend
(Sudo, Sumida, and Hibara 1998)	Flow measurements	Rc/D =2.0 Re = 60000	Hot Wire Anemometry	Evolution of axial velocity, Reynold stresses in the 90° bend
(Ono et al. 2011)	Flow measurements	Rc/D = 1.0, 1.5 Re = 1.8-5.4 x 10^5	Particle image velocimetry	Continuous separation on inner wall for the sharp bend (Rc/D =1) ; Intermittent separation for Rc/D =2 bend; Secondary flow in clockwise and counter clockwise direction flow alternately towards inside wall
(Takamura et al. 2012)	Flow measurements	Rc/D = 1.0 Re = 0.3-1.0 x 10^6	2D – Particle Image Velocimetry	Separation point was found to move upstream and reattachment point downstream with increasing Re; Three dominant structures were identified. Of them circumferential structure with oscillations at St ~0.5 were strongest.

(Mazhar et al. 2016)	Flow measurements	Rc/D =1.5 Re = 40000, 70000	2D - Particle Image Velocimetry	Flow evolution in 90° and S-bend; Comparison of velocity mag., TKE near the walls with mass transfer enhancement along the bend
(Tanaka 2009)	Flow simulation	Rc/D = 2.0 Re = 60000	Large Eddy Simulation	Consistency of flow through pipe bend with small Rc/D using numerical LES.
(Tan et al. 2014)	Flow Simulation	Rc/D = 1.0, 2.0 Re = 60000	Large Eddy Simulation with characteristic-based split scheme	Effect of Rc/D on flow structure; An additional pair of vortices observed for long radii bend Rc/D =2 having same rotation direction as that of main vortex.
(J. Kim, Yadav, and Kim 2014)	Flow Simulation	Rc/D = 2.0 Re = 60000	Different turbulence models	RNG $k-\epsilon$ model was found to give good results than other models
(Y. Wang, Dong, and Wang 2015)	Flow Simulation	Rc/D = 0.8 Re = 0.5 – 2.0 x 10^4	Detached Eddy Simulation	Turbulence intensity found to be in inverse relationship with Re;
(Dutta et al. 2016)	Flow Simulation	Rc/D =1.0 Re = 0.1-1.0 x 10^6	Standard $k-\epsilon$	Separation point was found to move upstream while reattachment moves downstream on in the inner wall with increasing Re; Maximum axial fluctuation on bend outlet increases slightly with Re at same location; Transverse fluctuation increases in mag. and moves towards pipe center with Re.

Table 2.1 Summary of some important literature of flow and its effects in 90° pipe bends.

2.4. Unsteady flow in pipe bends

Tunstall and Harvey (1968) performed visualization experiments in mitered bends using wool tufts, talcum powder and dye with air and water as the flow medium. It was shown that the secondary flow did not consists of twin vortices for turbulent flow in sharp bends. Instead, there was a single circulation that switched its rotation abruptly between anti-clockwise and clockwise directions. The switching of the secondary flow was coherent with the asymmetric vortex trail from the separation at the inner wall. The flow also had a separation at the outer wall but was found to not induce the switching. They concluded that turbulent flow and separation on the inner wall was necessary conditions for swirl switching. Brücker (1998) used DPIV measurements to study swirl switching phenomenon in a sharp bend with Rc/D = 1 at Reynolds numbers of 2000 and 5000. The authors found that the secondary flow at Re = 5000 had strong asymmetry while it was absent at Re = 2000. At Re = 5000, two vortices were found to alternatively dominate suggesting switching as oscillation of the plane of symmetry rather than a single vortex changing its rotational direction. Rutten et al. (2001;2005) using LES analyzed spectra of different quantities like vorticity, circumferential velocity and force integral on bend walls for bends with Rc/D = 1, 3 at Re = 5 – 27 x 10^3. The results showed a similar frequency in secondary flow oscillations for both bends suggesting separation was not necessary for the low frequency oscillations as presumed by Tunstall and Harvey (1968).

More recently, there have been several experimental (Sakakibara and Hashimoto 2010; Hellström et al. 2013; Kalpakli and Örlü 2013) and numerical (Rütten, Meinke, and Schröder 2001; Rütten, Schröder, and Meinke 2005; Carlsson, Alenius, and Fuchs 2015) studies on the swirl switching phenomenon downstream of the bend, which are reviewed by Kalpakli Vester et al. (2016). Many of these studies used the snapshot Proper Orthogonal Decomposition (sPOD) technique to identify large scale motions in the secondary flow at cross section planes downstream of the bend with Rc/D in the range 0.66-3.57 and Reynolds number in the range 2.3-12 x 10^4 (Sakakibara and Hashimoto 2010; Hellström et al. 2013; Kalpakli Vester, Ramis, and Alfredsson 2015; Carlsson,

Alenius, and Fuchs 2015). The snapshot POD is an orthogonal decomposition technique more efficient for data with large number of velocity data points and smaller number of realizations. This is different from standard POD which is more efficient for data with fewer measurement locations and large number of realizations (Tropea, Yarin, and Foss 2007). The results from snapshot POD in these studies revealed that the first two mode structures of the fluctuations are single swirl spanning the whole cross section and two vortices tilted from the symmetric axis. The time spectra of different flow quantities like transverse velocity (Brücker 1998; Kalpakli and Örlü 2013), POD coefficients (Hellström et al. 2013; Kalpakli Vester, Ramis, and Alfredsson 2015), swirl number (Carlsson, Alenius, and Fuchs 2015) and stagnation point (Rütten, Meinke, and Schröder 2001) identified a range of frequencies related to the secondary flow oscillations as shown in Table 2.2. Brücker (1998) found peaks in the power spectrum of transverse velocity near the inner wall at reduced frequencies ($St = \frac{fD}{U_o}$) of 0.03, 0.12 and 0.2 and suggested this to be related to the oscillations of the transverse flow. Rutten et al. (2001) analyzed the spectrum of force integral on the bend walls in directions parallel and perpendicular to the flow for bends with Rc/D = 1, 3 and at Re ranging from 5 – 27 x 10^3 from their numerical results using LES. There were peaks at St ~ 0.2-0.3 for each case that was found to be related to shear layer instabilities. Additional dominant low frequencies were identified at St of 0.0055, 0.014 which were related to the oscillation of the two vortices. Hellström et al.(2013) analyzed the spectra of the first three modes at a location 5 diameters downstream from the bend and found peaks at reduced frequencies, St = 0.16 and 0.33. The lower frequency was related to oscillation of two vortices while the higher one with the swirl switching mode and the two modes were found to interact at lower frequency. Kalpakli Vester et al.(2015) found a similar trend in the spectra of first two POD coefficients but at lower values of reduced frequencies (St = 0.04, 0.1) associated with the two modes. Carlsson et al. (2015) analyzed the spectrum of swirl number, obtained from the flow calculated using LES on the bends with Rc/D = 0.5 – 1.5 and at Re = 34000. The results suggested swirl switching composed of a high frequency

switching with St ~ 0.5-0.6 and low frequency switching with St ~ 0.01, 0.13. The high frequency was found to be prominent in the sharper bend (Rc/D =0.5).

Flow visualizations using PIV by Takamura et al. (2012) on a 90° bend with Rc/D = 1.0 and at Reynolds number of 0.3-1.0 x 10^6 found three periodic flow structures: (i) vortices shedding in the shear flow region with St of 1.0, (ii) vortices shedding near the separation region with St of 0.5 and (iii) circumferential motion with St of 0.5. The circumferential motions are found to be similar to that found by Ono et al. (2011) but were not termed as swirl switching. These circumferential motions are dominant out of the three structures and influence the structures in the separation region.

Tunstall and Harvey (1968) proposed that the swirl switching is caused by turbulent circulations from the upstream pipe entering the bend occasionally. Further studies for the origin of swirl switching were studied by (Sakakibara and Machida 2012; Carlsson, Alenius, and Fuchs 2015). Sakakibara and Machida (2012) performed simultaneous cross sectional PIV flow measurements upstream and downstream of a 90° bend with Rc/D = 1.0 to investigate the correlation between structures upstream and downstream of the bend. They found evidence of 7-8 diameter long streaks in the upstream pipe that appear with the change in azimuthal location of stagnation point or switching in the downstream pipe. The streaks were considered to be part of Very Large Scale Motions (VLSMs) observed in straight pipe flow that can have lengths up to 15 diameter (Smits, McKeon, and Marusic 2011). Carlsson et al. (2015) performed LES of the flow in bends with Rc/D = 0.5-1.5 and in the upstream straight pipe. The POD mode structures and spectra of its coefficients in the upstream pipe showed evidence of VLSMs with peaks at reduced frequency of St ~ 0.01, 0.13, which were also identified as low frequency switching downstream of the bend. However, high frequency switching (St ~0.5-0.6) which was less prominent in long radius bend (Rc/D = 1.56) was related to structures generated in the bend. Additional arguments were provided by high pass filtering the upstream flow for long radius bend (Rc/D =1.56) and plotting the spectra of POD coefficients in the downstream cross sectional plane. The low frequency peaks were

absent from the spectra confirming that the low frequency in the upstream pipe was propagated in the secondary flow oscillations.

Hellstrom et al. (2011) investigated the influence of a bend with Rc/D = 0.5 on upstream VLSMs. The VLSMs identified in the upstream pipe were found to exist downstream of the bend with azimuthal frequency slightly reduced and streamwise frequency slightly increased. Kalpakli Vester et al.(2015) using a honeycomb at the inlet found that suppression of unsteady upstream structures reduces or delays the swirl switching in the downstream pipe.

Author, year	**Re x 10^4**	**Rc/D**	**X/D**	**St**	**Technique**
(Tunstall and Harvey 1968)	4-22	0.5	2.2	0.001 - 0.004	Gold – shim flag
(Brücker 1998)	0.5	1	1.5	0.03 , 0.12, 0.2	2D2C PIV
(Rütten, Schröder, and Meinke 2005)	0.5-2.7	1 , 3	2.5	0.0055,0.014,0.2,0.3	LES
(Sakakibara and Hashimoto 2010)	12	0.667	2 , 10 , 15 , 25	0.07	2D3C PIV
(Hellström et al. 2013)	2.5	1	5, 12, 18	0.16, 0.33	2D3C PIV
(Takamura et al. 2012)	30-100	1	-	0.5, 1.0	2D2C PIV
(Kalpakli and Örlü 2013)	3.4	1.61	0.67	0.04, 0.12, 0.18	2D3C PIV
(Kalpakli Vester, Ramis, and Alfredsson 2015)	2.3	1.26	2	0.04,0.1	2D3C PIV
(Carlsson, Alenius, and Fuchs 2015)	3.4	0.5-1.5	0.67	0.01, 0.13, 0.5-0.6	LES

Table 2.2 Studies related to unsteady secondary flow in the bend and the Strouhal number described.

Chapter 3. Experimental Setup and Data Processing

The flow measurements were performed in a closed flow loop facility shown schematically in Figure 3.1. The fluid is pumped using a centrifugal pump from a 50L reservoir. Flexible hoses are used for the pump piping connections to minimize vibrations. The flow rate is kept constant at 2.58 m^3/hr to achieve Re = 34800 and measured using a turbine flow meter with an accuracy of $\pm 1\%$ of the flow reading. The flow passes through 25.4 mm diameter stainless steel piping and then turned 180° before entering a flow conditioning section consisting of a honey-comb. The flow then passes through a 25.4 mm diameter acrylic pipe with a length of 2.3 m (90D) before it enters the test section. The test section consists of a 4D long transparent acrylic straight pipe followed by the 90° bend with radius of curvature (Rc) of 1.5D. The bend is followed by a 3.5D long acrylic straight pipe section. The flow then enters a 10D long acrylic pipe and then a flexible hose before it returns to the reservoir. A bag filter is used at the outlet to filter out impurities. The fluid temperature is measured in the reservoir and maintained at 25 ± 0.5℃ using a compensation cooling loop. Distilled water from a chiller (Lytron Model RC045) is passed through a copper coil within the reservoir to cool the working fluid. A T-type thermocouple is placed in reservoir and temperature is monitored before and during the experiments.

The 90° bend is machined in two halves from acrylic rectangular blocks. The machined halves were polished to be optically clear and then adhered carefully (Mazhar et al. 2016). The straight transparent test sections were machined by drilling holes in rectangular acrylic blocks and then polished on a lathe to make the inside surfaces optically clear. All sides of the test sections are machined and polished to be optically clear. The inside diameter of test sections was machined to be 25.4 mm. The straight optically clear sections are attached to the bend section with an O-ring for sealing between the sections.

The flow measurements are performed to investigate the essential flow features in a single 90° bend and upstream and downstream of the bend section. The measurements were performed for the cross sectional planes shown in Figure 3.6. The axial cross section refers to the cross section containing axial flow and lies at symmetric plane of the bend. AUP (Axial plane in upstream pipe) plane covers axial cross section of upstream pipe from 2 D to 0.2 D, similarly ABP, AUBP, ADP are axial planes covering bend, upstream-bend inlet and downstream pipe section respectively. Cross section planes are the planes perpendicular to the axial flow and images are captured at 1D and 0.25D upstream, and at angles 10°, 20°, 70°, 80° and 0.25D and 1D downstream cross sections. To visualize cross section planes, the test section is turned 90° from vertical configuration to horizontal and the light sheet is rotated to coincide with cross section plane of the bend. The sign convention and the nomenclature used for representing the results is shown in Figure 3.7. The distance towards inner wall side is positive for axial flow. In the cross sectional plane, the inner wall side is on the left and outer wall side on the right.

3.1. Particle Image Velocimetry Setup

The velocity field was measured using two-dimensional refractive indexed matched Particle Image Velocimetry. Figure 3.2 shows the typical setup used to acquire data. A typical PIV setup uses a pulsed laser and a CCD camera with the timing diagram shown in Figure 3.3(a). In present experiments, a continuous laser and high speed CMOS camera is used which allows the flow to be continuously imaged as in Figure 3.3(b) and can achieve a temporal resolution of 0.055 ms of the flow. The continuous laser (Coherent Verdi 2.0) outputs a beam with a diameter of approximately 2 mm at a wavelength of 532 nm with maximum power of 2.20 W. The beam is redirected using right angle prisms and cylindrical lenses of focal length -4 mm and -12.5 mm are used to form a light sheet of approximately 2mm thick for imaging the axial cross section and transverse cross sections.

The images are captured using a high speed CMOS camera (Photron Fastcam SA4) that can capture images at frame rates up to 3600 Hz at 1024x1024 pixel resolution. The camera is focused for each experiment using a Nikkor lens (model AF micro-nikkor

60mm f/2.8d) on the illuminated plane. The magnification so obtained is different for each experiment/cross section captured. The camera is mounted on a scissor jack fixed at a position using step clamps on optical table and has the flexibility to be fixed at different angles. The two different sets of images are captured for the Reynolds average and unsteady flow respectively. The timing diagram for obtaining statistically independent fields by imaging 500 realizations at 5Hz (~10 integral time scale) is shown in Figure 3.3(c) and that for capturing unsteady flow by imaging 5459 realizations continuously at 1800Hz is shown in Figure 3.3(b).

The imaging of the flow in the test section is affected due to the curvature of the pipe as it distorts the particle images. To resolve this, a refractive index matching technique is used. A 64.2 wt.% solution of Sodium Iodide is prepared and used as the working fluid in order to match the refractive index of the acrylic test sections (Bai and Katz 2014; Mazhar et al. 2016). The properties of the solution calculated using equations from (Bai and Katz 2014) are tabulated in Table 3.1.

Properties	**Values Calculated**
Viscosity (μ)	1.8337×10^{-3} kg/(m s)
Density (ρ)	1772.35 kg/m^3
Refractive Index	1.4917

Table 3.1 Properties of 64.2wt% Sodium Iodide solution at 25°C from (Bai and Katz 2014)

The images are also distorted due to the air-acrylic interface when the image plane is not parallel to the test section face. To remove this distortion, acrylic wedges of matching angles are machined, polished and attached to the viewing surface as shown in Figure 3.4. Figure 3.5 shows the comparison in images of the calibration plate placed at a 10° plane of the bend, with water (image a,b), refractive index matched solution (image c,d), without 10° wedge (image a,c) and with 10° wedge (image b,d). The working fluid for the measurements was seeded with hollow spheres of size (~ 14 µm) coated with

silver (TSI model # 10089 silver) for the flow visualizations. The density of the particles is 1.65 g/cc (TSI Incorporated 2012) which is similar to the density of the solution resulting in negligible inertial effects of the particles on the flow (Raffel et al. 2007).

The PIV parameters like magnification, sampling rate and interrogation spot size for correct prediction of velocity of the flow are optimized using criterion given by (Keane and Adrian 1992)

1. The seeding particle should not travel more than a quarter of the interrogation spot in both dimensions namely length and width, between the two exposures. Thus,

$$MU_o \frac{\Delta t}{d_i} < 0.25$$

   where M is magnification (in pix/mm), U_o is (longitudinal/transverse) velocity (in m/s) , Δt is time between two frames and d_i is longitudinal/transverse dimension of interrogation spot.
2. The seeding particles should travel less than quarter of light sheet thickness between two exposures.
3. The duration of exposure should be small enough so that motion of a particle is frozen in the time duration.

Using the first criteria, the interrogation spot size is calculated to be greater than 40 pix taking into the account the maximum magnification achieved for the axial plane is 19.68 (pix/mm) with the Reynolds number of 34800 for the images captured at 3600 fps. The second criteria result in minimum thickness of sheet to be greater than 0.8 mm. The third criteria is used to set the electronic shutter speed at $\frac{1}{17000\,s}$.

3.2. Data Processing

The images are processed using a commercial PIV software (Insight 3G). The images are paired up to form the realizations. A background image obtained by averaging 50 pairs of images is subtracted from each frame to remove noise due to reflection and light scattered at the wall.

The images are divided into interrogation spots based on the quarter rule. The displacement is determined using a correlation analysis (Keane and Adrian 1992; Raffel et al. 2007). In the present study, image deformation is used with recursive grid and multiple passes in order to increase accuracy and spatial resolution (Raffel et al. 2007). The image deformation algorithm, deforms the image for the successive passes based on the flow calculated in the previous pass. The first pass for starting spot uses no offset and 2nd pass uses integer offset based on vector field from first pass, while the 3rd and subsequent passes uses sub pixel offset with image deformation. A minimum of 3 passes are used for image deformation. The offsetting and deformation increases the signal-to-noise ratio. Based on the achievable magnification, calculations as shown above that the interrogation spot greater than 40 X 40 (pixels) is required in first pass, so 64 x 64 (pixels) is chosen. The final pass is selected as 16x16, in order to correctly resolve the turbulence intensities and Reynolds stress near the wall (van Doorne and Westerweel 2007; Takeuchi et al. 2005).

The post processing of the data includes the validation and replacement of vectors in the field. For local validation, each vector is compared with neighboring vectors and if it differs by a pre specified value of displacement then it is replaced by the median of all neighboring vectors. The replacement scheme or vector conditioning includes the filling up of the areas which have wrong vectors or missing vectors or holes. The missing vectors are filled by median of 3x3 neighborhood values for axial plane processing and 9x9 for cross section plane images. The recursive filling option allows for multi pass conditioning in which holes are sorted by number of valid neighbors. In first pass, holes with most number of valid neighbors are filled and then in the next pass the holes with second most valid neighbors. In second pass and subsequent passes, the vectors filled in previous passes are considered as valid vectors.

A MATLAB code is developed and used for obtaining the mean and unsteady flow information from the velocity vectors from the PIV images. For the mean flow statistics, the mean velocity, turbulence intensities and Reynolds stresses are calculated at each spatial point using 500 realizations (or image pairs) for each cross section sampled

at 5 Hz. A global validation at each spatial location is performed over all realizations to remove velocity outliers that fall more than three standard deviations from the mean. Maximum number of outlier at any location is found to be ~30 out of all 500 vectors at that location.

The velocities are averaged over all the realizations to obtain the mean velocity (Sciacchitano and Wieneke 2016)

$$\overline{U}(x,y) = \frac{1}{N}\sum_{i=1}^{N} U\,(x,y) \tag{1}$$

where U is instantaneous velocity at i^{th} realization and N is total number of valid realizations at each point. The same is done with the other component of velocity.

The r.m.s of the velocity fluctuations are calculated by first subtracting the computed mean velocity from the instantaneous velocity for each realization

$$u = U - \overline{U} \tag{2}$$

and the root mean square and Reynolds shear stress are computed as (Sciacchitano and Wieneke 2016)

$$u' = \sqrt{\frac{1}{N-1}\sum_{i=1}^{N} u^2} \tag{3}$$

$$\overline{uv} = \frac{1}{N}\sum_{i=1}^{N} uv \tag{4}$$

where u and v are the velocity fluctuations of the two components. The unsteady flow analysis was performed for realizations measured at 3600 Hz continuously for 3 seconds for a total of 5459 realizations. The instantaneous images are analyzed using the snapshot proper orthogonal decomposition (POD) technique as in (Kalpakli and Örlü 2013;

Hellström et al. 2013; Carlsson, Alenius, and Fuchs 2015) to identify modes in the flow. In a flow field, fluctuations can be expressed as summation of product of modes which are function of space and the corresponding coefficients which are function of time. For example, streamwise component can be written as

$$U(x,y,t) = \bar{U}(x,y) + u(x,y,t) = \bar{U}(x,y) + \sum_{k=1}^{K} c_k(t)\varphi_{u,k}(x,y) \tag{5}$$

The fluctuations obtained by subtracting local mean velocity from each velocity vector of the measurements are rearranged into matrices. The correlation matrix, C is then calculated from fluctuation matrices as

$$C = \frac{1}{K}(u.u^T + v.v^T) \tag{6}$$

where u and v are the matrix of fluctuating velocities. The POD technique requires to find the solution of the eigenvalue problem

$$C\beta_m = \lambda_m \beta_m \tag{7}$$

where β is matrix of eigenvectors of C and λ is matrix of corresponding eigenvalues. The POD modes are obtained by projecting u and v onto the eigenvector β_m. For example

$$\varphi_{u,m} = \sum_{k=1}^{K} u^{(k)}\beta_{k,m} \tag{8}$$

Similarly, φ_v can be obtained. Modes are orthogonal to each other and typically normalized to be orthonormal. The time coefficient c_m can be obtained by projecting original fluctuating fields onto the modes and summing both u- and v- coefficients.

$$c_m = \sum u.\varphi_u + v.\varphi_v \tag{9}$$

The velocities can be reconstructed from few energetic modes which effectively discards the small structures and reconstruct the flow showing the effect of large scale structures. The velocity field is reconstructed as

$$u^r(x,y,t) = \bar{U}(x,y) + \sum_{m=1}^{P} c_m \varphi_{u,m} \tag{10}$$

where P is the number of modes of interest. The reconstruction in many cases is performed to examine the contribution of the modes to the fluctuating velocity field which is done by a similar approach but without adding the contribution of mean velocity field. The present study adopted from Chen et al.(2012) modified to obtain the POD modes for the fluctuating velocities. The POD modes are arranged in decreasing order of energy content or Eigen values since the function are orthonormal, the first mode contains maximum energy and contributes most to the mean square energy to the fluctuating field on the plane of interest.

The power spectra of the coefficients of the POD modes are determined using the Welch method (Kalpakli Vester, Ramis, and Alfredsson 2015). A window covering 2000 sample time is used with 50% overlap. The window size is determined such that a Strouhal number ($St = fD/U_o$) resolution of ~0.0166 can be captured with maximum data points in a window.

3.3. Uncertainty Analysis

The density of seeding particle in an interrogation spot, camera focal and zoom are adjusted such that vector validation rate should be more than 99% in each realization of axial cross section. However, in cross section planes due to the presence of background noise a validation rate of approximately 80% can be reached. The uncertainty in PIV measurements is due to various sources like equipment, particle lag, sampling size, processing algorithm etc. The uncertainty due to particle lag is small considering the density matched particles are used in a moderately accelerated flow. Therefore, the other three sources are considered for assessing uncertainty in mean flow experiments. For calculations the 500 realizations used for measuring the mean statistics are used here. The velocity can be expressed as $U = M\frac{\Delta X}{\Delta t}$ where M is magnification (in mm/pix), ΔX particle displacement (in pixels), Δt is change in time. The uncertainty in axial velocity from equipment is calculated with values given in Table 3.2, to be 0.4% using the

approach described in (Lazar et al. 2010). For the uncertainty from processing algorithm, effect of particle image diameter, particle density, displacement and gradients are taken into account (Wilson and Smith 2013). The values used for uncertainties are obtained from the curves generated by simulation results for these parameters (Raffel et al. 2007) as shown in Table 3.3. The uncertainty due to sampling in mean velocity, turbulence intensity and Reynolds shear stress is (Benedict and Gould 1996)

$$\Delta_U = \frac{u'}{\sqrt{N}}$$

$$\Delta_{u'} = \sqrt{\frac{\overline{u^4} - \overline{u^2}^2}{4N\overline{u^2}}}$$

$$\Delta_{uv} = \sqrt{\frac{\overline{u^2v^2} - \overline{uv}^2}{N}}$$

where Δ is absolute uncertainty in subscript quantity, u' is standard deviation, ρ_{uv} is cross correlation coefficient between u and v and N is the number of samples.

The relative uncertainty ($\epsilon_U = \Delta_U/U$) due to sampling in mean axial velocity calculated as 0.75% near the wall and 0.16% in pipe center. The relative uncertainty in turbulence intensities is 18% while that in Reynolds shear stress is 15% in the core and increases up to 35% in the wall region (Figure 3.8 and Figure 3.9).

The total relative uncertainty is given by $\epsilon_{total} = \sqrt{\epsilon_{equip}^2 + \epsilon_{proc}^2 + \epsilon_{sampling}^2}$. Hence, the total relative uncertainty in mean velocity measurements is 1.9% near the wall and 0.66% in the pipe center.

Parameter	Value	Uncertainty in value
Calibration scale physical length, l	25.4 mm	0.1 mm
Calibration in pixels, L	500 pix	3.5 pix
Distance from calibration scale to lens, λ	500 mm	1 mm
Timing by camera, Δt	277.78μs	~ O(ns)
Uncertainty equipment, $\epsilon_{equipment}$	0.4%	

Table 3.2 Summary of uncertainty parameters and values.

Parameter	Value	Uncertainty in value
Particle image diameter, d_τ	2.4 pix (Warner and Smith 2014)	0.015 pix (Raffel et al. 2007)
Particle Density, d_ρ (per interrogation area)	7.68/pix (Warner and Smith 2014)	0.035 pix
Displacement, Δx	5 – 9 pix	0.01 pix
Gradients, grad	0.01 – 0.1 pix/pix	0.11 pix
Uncertainty processing, ϵ_{proc}	1.7 % (near wall) 0.5% (pipe center)	

Table 3.3 Uncertainty due to processing algorithms.

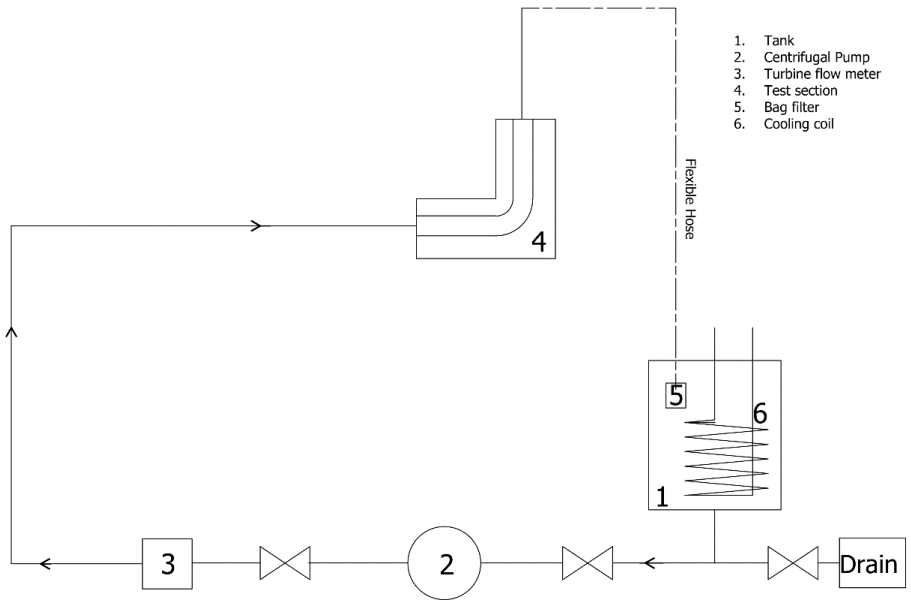

Figure 3.1 Schematic of the flow loop used for the PIV measurements in a 90° bend.

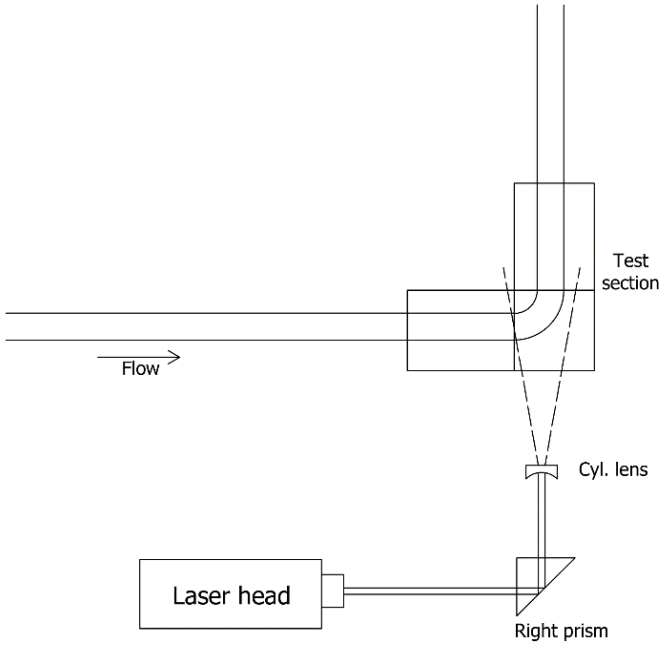

Figure 3.2 Schematic of PIV setup for measurements on centerline in axial cross section.

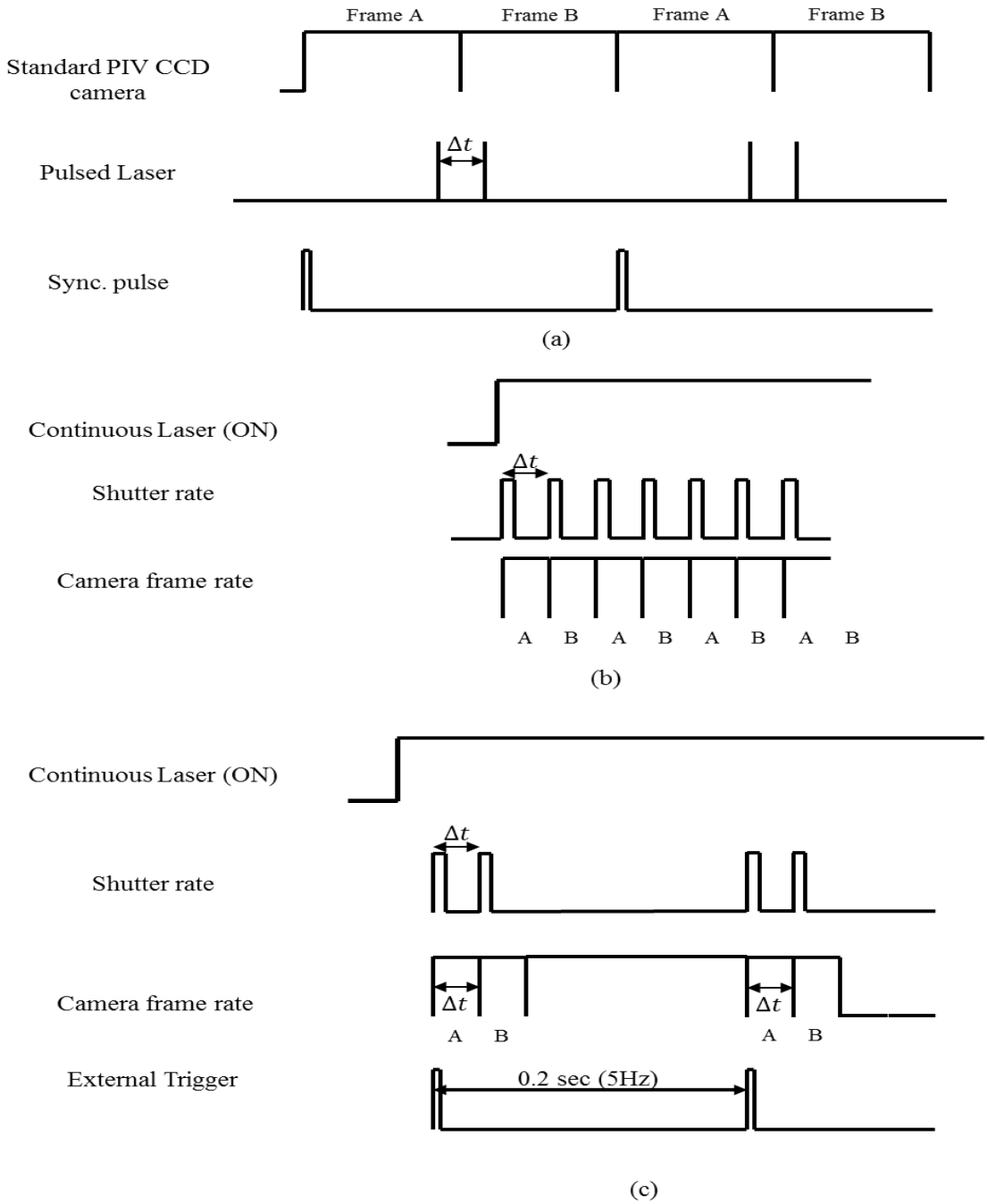

Figure 3.3 Timing diagram for (a) Standard PIV (b) continuous imaging for unsteady flow (c) Imaging at 5Hz for mean flow.

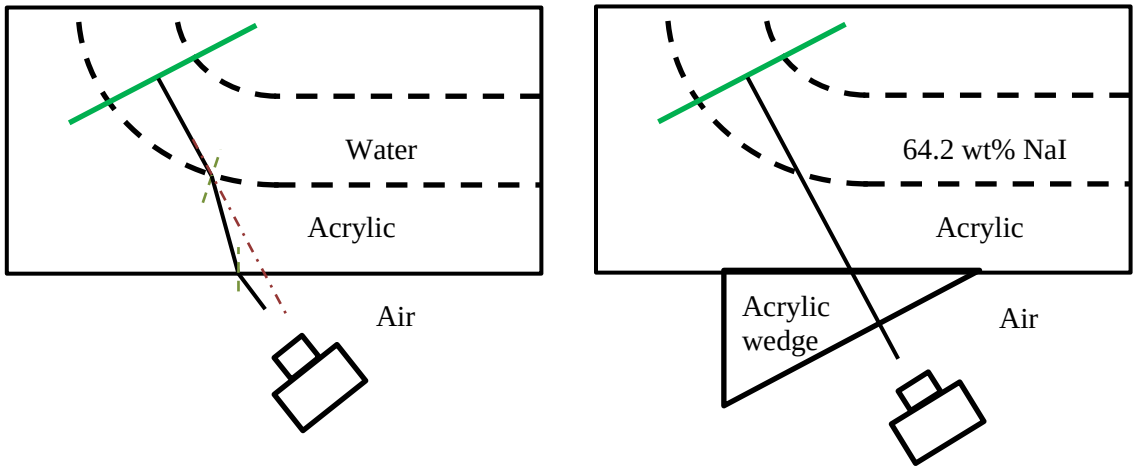

Figure 3.4 Schematic showing ray diagram from cross section plane without and with NaI solution and acrylic wedge.

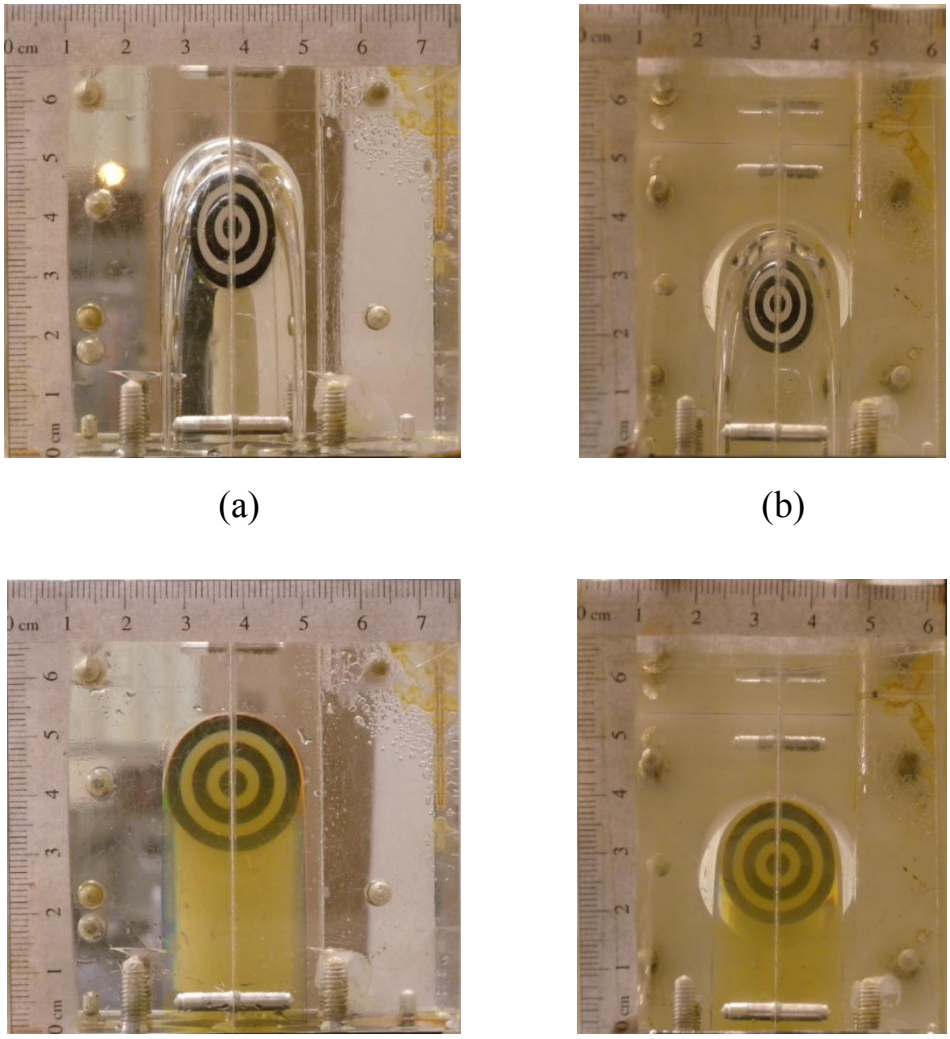

Figure 3.5 Calibration plate place in image plane at 10° cross section (a) water without wedge (b) water with the wedge and (c) NaI without wedge (d) NaI with the wedge.

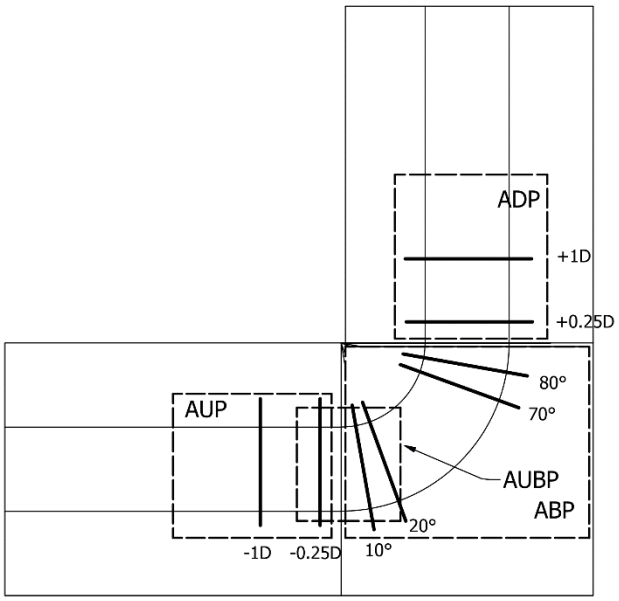

Figure 3.6 Schematic showing imaged planes.

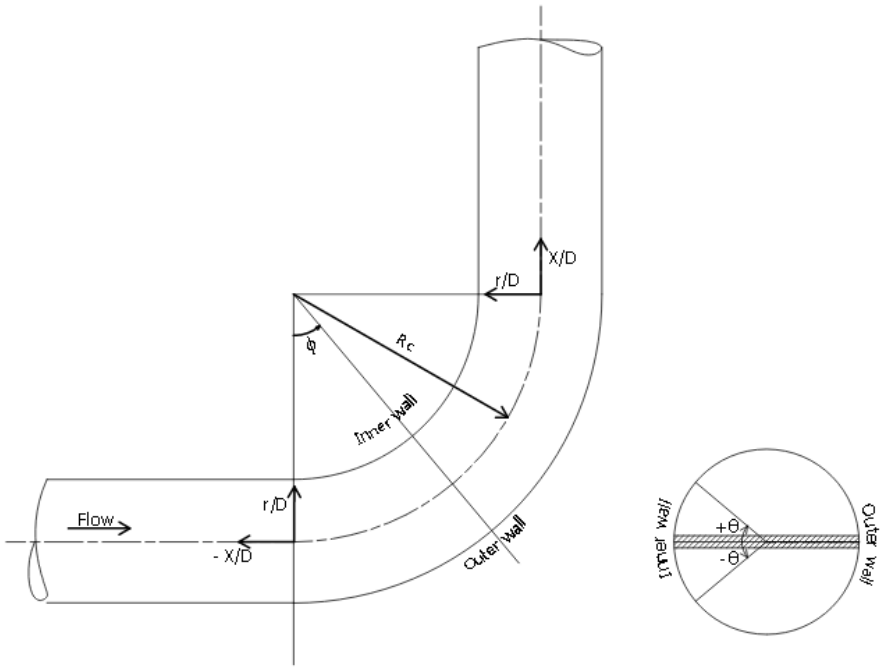

Figure 3.7 Schematic defining the nomenclature of 90º bend.

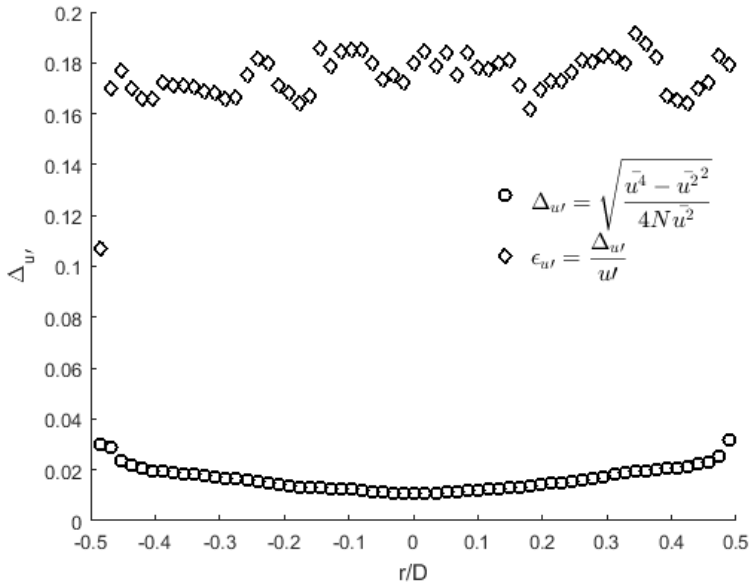

Figure 3.8 Uncertainty in axial turbulence intensity

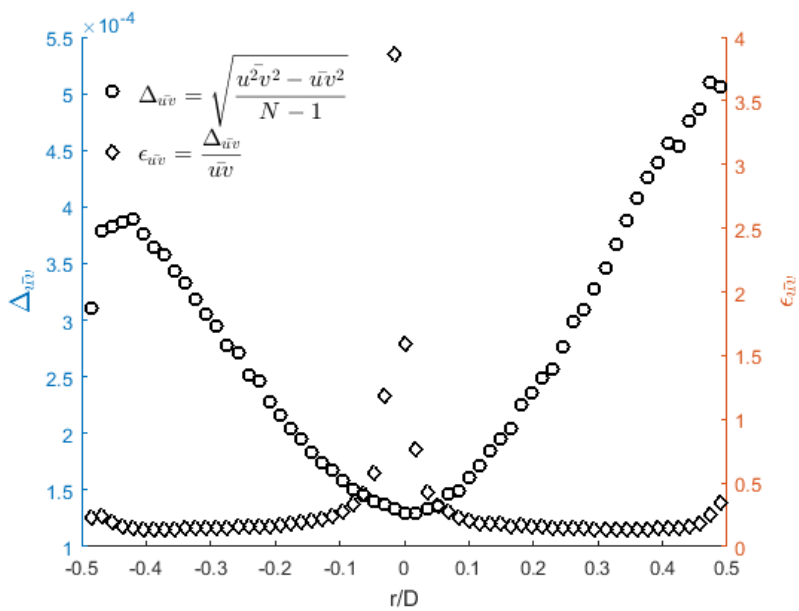

Figure 3.9 Uncertainty in Reynolds shear stress.

Chapter 4. Results and Discussions

The measurements reported here are all for bend with Rc/D =1.5 and Reynolds number of 34800. The Reynolds averaged flow measurements are presented first. This is followed by the unsteady results.

4.1. Reynolds Averaged Flow Measurements

The mean velocity profile in the pipe upstream of the bend normalized by the centerline velocity is shown in Figure 4.1. The results are the average of the profiles measured between 2D and 1D upstream of the bend. The results are compared with the power law velocity profile given by

$$\frac{U}{U_c} = \left(1 - \frac{r}{R}\right)^{1/n}$$

$$n = -1.7 + 1.8\, log(Re_{Umax})$$

for a value of n = 6.6. The profiles are symmetric and agrees with the power law profile. The mean velocity profile in wall units ($y+ = yu*/\nu\,, U+= U/u*$) are shown in Figure 4.2 and compared with LDV measurements at Re = 24600 (Toonder and Nieuwstadt 1997). Here the friction velocity, $u^*_{(1)}$ = 0.072 m/s was determined using the Fanning friction factor. The present PIV results are consistent with the LDV results for y+ > 40. The near wall region is not well resolved and the data for y+ < 30 is likely unreliable. The variation of Reynolds shear stress across the pipe is shown in Figure 4.3. The variation in profile is linear as expected except near the walls. Estimates of viscous stress shows it is small over the region where mean velocity field is well resolved. The near wall peak in the viscous stress could not be resolved but is not responsible for the roll off in the Reynolds shear stress since it is the total stress that varies linearly with position across the pipe i.e.$-\overline{uv} + \nu\, dU/dr = \tau_w/\rho$ (Tennekes and Lumley 1972). The value of τ_w and u* determined by fitting the profile of total shear stress is smaller than the friction velocity used to fit the mean velocity. This was observed earlier by Takeuchi et al. (2005) and van Doorne et al.(2007) and attributed to spatial averaging due to the resolution

acting to low pass filter the fluctuating velocity field. The filtering would be more significant at the wall where the motions are expected to be smaller scale. The total stress profile is extrapolated to the wall to obtain friction velocity, $u^*_{(2)}$ = 0.064 m/s for the filtered field. The axial and transverse turbulence intensities and Reynolds shear stress profiles normalized by the friction velocity, $u^*_{(2)}$ are compared with the turbulence intensities from LDV measurements by Toonder and Nieuwstadt (1997) in Figure 4.4 and Figure 4.5. The profiles are within measurement uncertainties in the core region as expected. The asymmetry in intensity profile near the wall can be attributed to the fact that the inner wall side is farther from the laser which results in lower illumination. The results for mean velocity, turbulence intensities and Reynolds shear stress obtained from 5000 realizations at 1800 Hz compared with the profiles that are obtained from the 500 statistically independent fields measured at 5Hz are presented in Figure 4.6. The convergence of profiles suggest that the measurements obtained for unsteady analysis of the flow are accurate.

Contours of mean velocity magnitude on the symmetry plane of the bend and upstream and downstream pipes are presented in Figure 4.7, while profiles of normalized mean streamwise axial and transverse velocities are shown in Figure 4.8 and Figure 4.9. Positive values for the radial distance are towards the inner wall side. The results show that the high velocity region of the flow on the symmetry plane shifts from the central region towards the inner wall of the bend as the flow enters the bend and then moves towards the outer wall at $\phi \sim 40^o$. This high velocity region remains at the outer wall side as the flow exits the bend into the downstream pipe. At 2D and 1D upstream of the bend, the axial profiles show that the flow is not affected by the bend and the velocity profiles are consistent with the fully developed profile in a pipe. The transverse velocity is nearly zero implying no significant secondary flow. The flow near the inner wall is accelerated from 0.25D upstream until $\phi = 30^o$, while that near the outer wall decelerates due to axial pressure gradients developed on the inner and outer wall. At 0.25D upstream of the bend, the transverse velocity is positive which changes to negative at $\phi = 10^o$ implying that the mean transverse flow on the symmetry plane is directed towards the inner wall at 0.25D

upstream of the bend and then towards outer wall in most of the bend and downstream pipe. Further downstream in the bend at ϕ of 40° to 60°, the high velocity region shifts away from the inner wall. The decrease in mean velocity in this region may indicate an unsteady separation of the flow at the inner wall. The velocity near the inner wall increases again in the last part of the bend and downstream of the pipe with an inflection in the velocity profile between the near inner wall region and the high velocity region that appears to be a shear layer which is also reported by Ono et al.(2011). The transverse velocity profiles develop an inflection point at a similar position as the mean axial velocity profiles. At the outer wall the axial flow starts accelerating around ϕ of 70° and the high velocity at the outer wall persists in the downstream pipe. In the downstream pipe, the mean transverse velocity is higher near the inner wall side. The velocity profiles here are similar to those of Mazhar et al.(2016) in the same bend at a Reynolds number of 40000. The differences in part are because the results here are for axial velocity while Mazhar et al.(2016) presented the velocity magnitude. The results here are also consistent with the data of Sudo et al.(1998) for a bend with Rc/D = 2.0 at Reynolds number of 60000. The differences at ϕ of 50-70° near the inner wall can be attributed to the larger radius of curvature of the bend used by Sudo et al. (1998).

Contours of the averaged turbulent kinetic energy ($\frac{\overline{u^2}+\overline{v^2}}{U_o^2}$) on the symmetry plane within the test section are shown in Figure 4.10 while the streamwise profiles at different locations are shown in Figure 4.11. The magnitude of ($\overline{u^2}+\overline{v^2}$) increases near the outer wall at the bend inlet. This increase extends further away from the wall as the flow goes through the bend. High values of ($\overline{u^2}+\overline{v^2}$) are found along two regions near the inner wall. The high ($\overline{u^2}+\overline{v^2}$) on the inner wall starts at ϕ ~ 30-40° and extends up to 0.5D downstream. The other region corresponds to the shear layer and can be seen as an inflection point in the profiles starting from ϕ ~ 60° and extending into the downstream pipe. The value ($\overline{u^2}+\overline{v^2}$) remains higher in the separation region than on the outer wall side. The results are consistent with axial turbulence intensity seen by (Ono et al. 2011; Mazhar et al. 2016) which was attributed to movement of the separation region.

Figure 4.12 shows the contour plot of Reynolds shear stress ($\overline{uv}$) in the axial planes and Figure 4.13 show the streamwise profile of the same at different locations along the test section. Three high shear regions can be identified in the symmetry plane. A high shear stress region is formed at the outer wall in the inlet region which exist at the outer wall throughout the bend and decreases in the downstream section. The other two high Reynolds shear stress regions can be identified as one on the inner wall and other in the shear layer, both of which can be seen emanating from a point on the inner wall near $\phi \sim 40^o$ which is a point of unsteady separation. The profiles in the upstream pipe are symmetric about the center and have relatively low values. The values increases slightly near the inner and outer wall until $\phi \sim 50^o$. At $\phi = 60^o$, the inflection point in the profile near the inner indicating the shear layer is found and the sign of Reynolds shear stress on the inner wall changes. In the downstream pipe, the inflection point moves towards the outer wall while the shear stress on outer wall vanishes.

The change in the mean secondary flow in the cross sectional planes is shown in Figure 4.14. The results in cross sectional planes upstream and first half of the bend are plotted on different scale. The inner wall side is on the left and outer wall side on the right for all the cross sectional plane results. The secondary flow at the 1D and 0.25 D upstream cross sections is very small in magnitude and radial in nature. At the bend inlet, which cannot be captured in the present study, Sudo et al.(1998) found that the secondary flow is directed towards the inner wall which changes into twin vortices by $\phi = 30^o$. In the present results, at $\phi = 10^o$, a secondary flow is seen to be developing into two counter rotating vortices, which are developed with centers near the side walls at $\phi = 20^o$. The transition between 20° and 70° is not captured in the present study. At 70° and 80° from the bend inlet, the two vortices have strengthened with relatively high magnitude secondary velocities on the side walls at $\theta \sim \pm 45^o$. In the downstream planes of 0.25 D and 1D, the secondary flow weakens.

Cross sectional contours of the turbulent kinetic energy ($\overline{v^2} + \overline{w^2}$) at the different locations along the test section are shown in Figure 4.15. The contours of turbulent

kinetic energy ($\overline{v^2} + \overline{w^2}$) in the upstream cross sections and in first half of the bend is plotted with different scales. The kinetic energy is axi-symmetric at 1D and 0.25D upstream planes with low values in the core region and higher values at the wall regions as in the profiles of transverse turbulence intensity in the upstream pipe. At the 10° and 20° planes, an increase in the ($\overline{v^2} + \overline{w^2}$) is observed near the outer wall side. The ($\overline{v^2} + \overline{w^2}$) value increases slightly on the outer wall side as the flow evolves through the bend until 0.25D downstream. The planes at 70° and 80° from the bend inlet show higher values of ($\overline{v^2} + \overline{w^2}$) near the inner wall side which can be attributed to unsteady separation on the inner wall. In the cross section planes downstream of the bend, the high ($\overline{v^2} + \overline{w^2}$) region near the inner wall spreads further towards the center of the pipe. Two distinct regions of high ($\overline{v^2} + \overline{w^2}$) appear to occur on the cross section plane 1D downstream of the bend. The one more in the core of the pipe while the second appears related to the flow near the wall like the axial turbulence intensity observed on symmetry plane. The results are consistent with the studies of Sudo et al.(1998) and El-Gammal et al.(2010).

4.2. Unsteady flow

The Proper Orthogonal Decomposition (POD) technique is used to examine the large scale structures within the flow. The results presented here will, in general, include the first five POD mode structures along with the mean flow structure, percentage of total fluctuation energy content in first 20 modes, time series of the first five POD coefficients and the spectra of the POD coefficients plotted in linear and log-log scales. The results for the axial symmetric plane in the upstream pipe from 2D to 0.2D are shown in Figure 4.16. Here, the contours of axial components of the POD modes are presented, where red and blue represent positive and negative values respectively. In the upstream pipe, the first mode can be seen as long streaks of positive and negative values of u on either side of the pipe. These may be associated with the so-called Very Large Scale Motions (VLSM) in the pipe, which are known to extend up to

15D in length (Smits, McKeon, and Marusic 2011). The subsequent 2nd, 3rd and 4th modes have structures of length scale on the order of the pipe diameter. The histogram of energy shows that the first and second mode contributes 7.8% and 5% of total fluctuation energy while next four modes contains 2-2.5% of total fluctuation energy. The spectra of the coefficients for the first mode has peaks at frequencies corresponding to St $(= fD/U_o)$ ~ 0.01, 0.07, 0.1. The time series of the coefficients of the first POD mode shows that the contribution of this mode is intermittent. There are periods where the coefficient is large and the variation nearly periodic (these are shown by the red lines on the time trace). In other periods, the coefficient is small and the variation is more complex. The time scale of the large amplitude nearly periodic motions corresponds to non-dimensional time $\tau(= tU_o/D)\ of\ 10\ (St{\sim}0.1)$ and occur for τ of 30. The full cycle (on and off) has a time scale of 60 to 80 corresponding to a nominal St of 0.014. The spectra for the 2nd mode has peaks at St ~ 0.07 and St ~ 0.13. These results are consistent with 3-dimensional LES data of Carlsson et al.(2015) in the upstream pipe, where the first two modes were reported as long and short streaks respectively with St of 0.01 and 0.13. The spectra of coefficients of the higher modes 3rd, 4th and 5th shows peaks at St ~ 0.1 with some peaks at St ~ 0.3 to 0.6 implying existence of smaller scale and higher frequency structures.

The analysis of a section that includes the upstream pipe and bend inlet (Figure 4.17) shows that the first POD mode consists of high and low velocity streaks moving towards the center of the pipe. The 2nd most energetic mode includes structures similar to the first mode in the upstream pipe. The energy histogram shows that the first mode contributes 5%, 2nd and 3rd modes contributes around 2% while next three modes contributes 1-1.5% of the total fluctuation energy. The spectra of the first POD coefficient shows peaks at frequencies corresponding to the St ~ 0.01, 0.05 and 0.13. The other modes also show peaks at the low frequencies i.e. St ~ 0.01 to 0.2 but the amplitude relative to the first mode is small. The time signal for the coefficients of the first POD mode shows an intermittent behavior though not as distinct as in the upstream pipe. The two regions of high amplitude identified persist for a time $\tau\ of\ 30$ and the time between

start of the different periods is again $\tau\ of\ 60 - 80$ that corresponds to St of 0.014 (represented by the red lines).

The POD analysis results for the downstream pipe (0.2D – 2D) are shown in Figure 4.18. The contours of the axial component of modes reveals that the most energetic mode consists of structures corresponding to motions in the core of the pipe while the other modes reveals small structures near the walls. The energy content of first mode is around 6.5% while that of next four modes is between 2-3.5% of total fluctuation energy. The spectrum of the coefficients of first POD mode shows frequencies corresponding to St of 0.03, 0.07 and 0.13. The time series of the coefficient of first mode shows the intermittency and time scale of change from lower amplitude to higher one is $\tau{\sim}30$ ($St{\sim}0.03$). The time scale during both high and low amplitude periods is $\tau{\sim}8$ ($St{\sim}0.13$). The spectra plotted on the log scale show a rapid decay beyond a frequency corresponding to St of approximately 0.5 to 0.6. This change in the spectra is often taken as a shedding frequency (Ebara et al. 2010; Takamura et al. 2012). This is similar to the frequency observed by Takamura et al.(2012) in the downstream pipe suggesting there may be a higher frequency mode in the downstream pipe.

The results of the POD analysis on the cross-sectional planes along the test section are shown in Figure 4.19-Figure 4.26. Here the modes are represented using streamlines. The results for the cross sections in the upstream pipe at X = -0.25D and -1D show POD mode shapes as multiple vortex structures extending from the wall to the pipe center. The structures are consistent with structures seen in fully developed straight pipe flow that are thought to be related to the VLSM (Dennis and Sogaro 2014; Hellström, Sinha, and Smits 2011; Carlsson, Alenius, and Fuchs 2015). The contribution of the first five modes for the location X = -1D to the total fluctuations is quite similar and small ranging from 1.1% - 1.3%. The time spectra for the first POD coefficients at the -1D cross section shows a peak at St ~ 0.8, which is also seen for the 2nd mode indicating an interaction between the two modes. The 2nd, 3rd and 4th modes along with 1st mode shows peaks in range of St ~ 0.05 to 0.2. The cross sectional analysis at -0.25D reveals similar structures in the POD modes. The peak in the spectra of the coefficients for the first mode

is again at St of 0.8 and peaks for higher modes occur at St of 0.05 and 0.1. Thus, the results suggest that the turbulence in the upstream pipe have both a high and low frequency components related to Large Scale Motions (LSM) and VLSM respectively (Kim and Adrian 1999). The time series of coefficients in these planes is complex and no single cycle of events can be identified.

The results at the 10° and 20° planes are shown in Figure 4.21 and Figure 4.22. The POD modes at these planes consist of organized motions near the outer wall. At the 10° plane, the first mode contributes around 2% of total fluctuation energy (see the energy histogram) while each of the next four modes contribute 1.1-1.5%. The spectra of the coefficients of the first POD mode on the 10° plane reveals a distinct peak at a frequency corresponding to St ~ 0.07. The corresponding time series of the first mode coefficients reveals periodic behavior which was not seen in the time series of the POD coefficients in the cross sectional planes upstream of the bend. The time series have multiple frequencies ranging from $\tau = 10(St{\sim}0.1)$ to 15 (St ~0.07) which is also seen in the frequency spectra. At the 20° plane, the first POD mode contributes around 2.8% whereas the next four modes have relative energy content ranging from 1.5-2.5%. The time spectra of the first POD mode at the 20° plane also shows a distinct peak at St ~ 0.07. The second and third mode shows additional peaks at St of 0.03 and 0.18, respectively. The time series for coefficients of the first POD mode shows a range of frequencies for its periodic behavior. The distinct peak at St ~ 0.07 at both 10° and 20° planes suggests that the VLSM with frequencies of St ~ 0.07 and 0.13 from the upstream pipe imparts the oscillation to the secondary flow on these planes while the effect of the high frequencies motion from the upstream pipe related to LSM may not.

The results at cross section planes at ϕ of 70° and 80° show the evidence of prominent modes (Figure 4.23 and Figure 4.24). The first mode shape at both planes shows two vortices with one dominating and spanning most of the cross section whereas the second POD mode is two vortices of equal strength slightly tilted from the symmetry line. The third mode shows a single dominant structure and the higher modes show more than two structures in a complex orientation. The histogram of the energy shows that the

relative energy of the first mode in these planes has increased to ~8% and the second mode contributes 6.5% and 7.8% of total fluctuation at 70° and 80° planes, respectively. The frequency spectra of the first POD mode coefficients at ϕ=70° plane shows a peak corresponding to St ~ 0.07. The time signal also shows fluctuations with a period approximately corresponding to this frequency. The peak for the first mode coefficient at ϕ=80° also occurs at St ~ 0.07. There are additional peaks in the spectra of the coefficients of the first, second and third modes in the Strouhal number range 0.05 to 0.2, reflecting more variability in the time signal. The frequency spectra of POD mode coefficients at the 70° plane show small peaks at higher frequency which are more distinct on the 80° plane. The spectra plotted on log-log scale shows a distinct roll off at St ~ 0.5, similar to seen for the spectra of coefficients on the downstream plane in downstream pipe. The locations of the motions in the measurements on the symmetry plane downstream plane suggest that this frequency corresponds to the structures related to the flow separation from the inner wall. The role of these frequencies will explored further in the flow field reconstructions.

The results for the cross sectional planes downstream of the bend at $X = 0.25\ D\ and\ 1D$ are shown in Figure 4.25 and Figure 4.26. The first POD mode shows a single swirling structure spanning the whole cross section, while the second and third mode depicts two vortices tilted at different angles from the centerline, consistent with the results of Sakakibara et al.(2010), Hellström et al.(2013) and Kalpakli Vester et al.(2015). The histogram of energy shows that the first mode contributes ~9% and ~11% of total of the fluctuation energy at the 0.25D and 1D planes, respectively. The first five modes contribute nearly 30% to the total fluctuations indicating that much of the large scale fluctuations can be captured by the first few modes. At the 0.25D plane, the spectra of time coefficients show peaks at frequencies corresponding to St ~ 0.07 and St ~ 0.13 for both the first and second mode, suggesting that the two modes complement each other. Prominent peaks at higher frequency with St ~0.2-0.4 can also be seen. At the 1D plane, the spectra of the POD coefficients reveals peaks at frequencies related to St of 0.03 and 0.13, which are similar to that found by Brücker (1998), Kalpakli Vester et

al.(2015) and Carlsson et al.(2015). The lower frequency changes from the 0.25D plane. The spectra of the first mode at 1D also showed evidence of peaks at frequencies of 0.4 to 0.6. The log scale spectra shows the rapid decay from St ~ 0.5 on both the planes similar to 70° and 80° planes.

The energy content of the POD mode reflects the amount of energy that is contained by the mode over the total plane. The contour plots of ($\overline{v^2} + \overline{w^2}$) showed three regions of elevated fluctuations in the cross sectional plane in the downstream pipe. Thus it is important to consider the local reconstruction of the turbulent kinetic energy ($\overline{v^2} + \overline{w^2}$) on the planes. The turbulent kinetic energy is reconstructed from the first 25 modes shown as successive group of five modes and cumulative reconstruction in step of five modes at downstream cross sections of 0.25D and 1D in Figure 4.27-Figure 4.30. The plots show that at 0.25D downstream cross section, the first five modes primarily capture the region near the outer wall and the region nearest the inner wall. Higher modes are required to capture the region in the core flow. Spectra of the coefficients for the sixth mode (Figure 4.31) show broad peaks centered about St of 0.43 and 0.7. However, at 1D downstream, the reconstruction shows that the first five modes captures all the three regions and higher modes adds more features to them. The spectra in Figure 4.32 shows peaks at wide frequency range but most of energy content is in frequencies of St < 0.5. The reconstruction of turbulent kinetic energy for planes of 20° and 80° are shown in Appendix A.

The contribution of the POD modes to the total energy on the plane can be calculated by adding the energy associated with the mean flow field to that associated with the fluctuations. The relative contribution of the fluctuation to the total energy of the flow and the contribution by first six modes to the energy associated with the fluctuations for the latter part of the bend and downstream pipe are shown in Table 4.1. The results show that the energy content of the fluctuations increases from the cross sectional plane at 70° to 1D downstream of the bend implying an increase in the unsteadiness of the flow.

The contribution from the first six modes is ~30% of the total fluctuation suggesting that six modes are sufficient for reconstruction of the total velocity.

Cross section plane	**Percentage of total energy contributed by fluctuations**	**Percentage of total fluctuation energy contributed by first six modes**
70º	23.65	31
80º	24.18	34
0.25D downstream	28.2	33
1D downstream	36.8	32

Table 4.1 Contribution of fluctuations to the total flow and contribution by first six modes to the total fluctuations.

4.3. Reconstruction of the flow from the POD modes

The secondary motions on the different planes can be better understood by reconstructing the flow with a smaller number of POD modes. This reflects the effect of the interaction between the different modes. Reconstruction of the fluctuations and total velocity using the first six modes for different cross section planes every 0.138 s corresponding to frequency of 7.2Hz (St ~ 0.13) are shown in Figure 4.33 through Figure 4.48. The results here cover approximately 92% of the total time record and represent 20 realizations of the flow at different times.

The reconstructed fluctuations at the cross sectional planes 1D and 0.25D upstream of the bend (Figure 4.33 and Figure 4.35) show multiple structures extending from the wall to the center of the pipe that can be seen changing orientation with time. The effect of this change in orientation on the total velocity (Figure 4.34 and Figure 4.36), which is reconstructed from the fluctuations and mean velocity, can be seen as

movement of the center of the flow and may be interpreted as precession of the bulk flow related to the effect of LSM and VLSM.

The fluctuations reconstructed at 10° and 20° cross sectional planes (Figure 4.37 and Figure 4.39) shows some organization and differ from the structures in the upstream cross sectional planes. The total velocity reconstructed at the 10° plane (Figure 4.38) shows change from the radial velocity to two developing vortices and the flow can be seen recirculating towards the inner wall with movement in the flow center similar to planes 0.25D and 1D upstream. The total velocity reconstructed at the 20° plane (Figure 4.40) show the presence of two vortices. Here, the addition of the fluctuations to mean velocity imparts unsteadiness in total velocity. Structures near the outer wall shows up at τ = 14.7, 29.4, and 58.7 in the total velocity.

Further downstream at 70° and 80°, the reconstruction of the fluctuations (Figure 4.41 and Figure 4.43) shows two vortices oscillating about the symmetry plane and dominating in most realizations but this changes to a single swirl at different times. At the 70° plane, the single swirl can be seen dominant in clockwise direction at the τ=36.7 which changes to a single swirl in the counter-clockwise direction at τ=95.5. Similar structures in the fluctuations can be identified in the 80° plane at τ=36.7 and τ=125. The effect of these fluctuating structures on total velocity (Figure 4.42 and Figure 4.44) can be seen as an oscillation of the symmetric axis between two vortices associated with the mean secondary flow that increases modestly in amplitude in these planes.

The reconstructed fluctuating field in the downstream cross sectional planes at 0.25D and 1D (Figure 4.45 and Figure 4.47) shows similar oscillating and dominating structures as that in 70° and 80° planes. However, the effect of these fluctuations on total velocity (Figure 4.46 and Figure 4.48) is more complex. The total velocity at the 0.25D plane is found to oscillate about the symmetry plane with a higher amplitude than on the 70° and 80° planes. At the 1D downstream plane, the two vortices of total velocity dominate one another at some instances in addition to oscillating about the symmetry plane.

The dynamics of motions can be further examined by reconstructing the flow fields at higher frequencies in order to visualize multiple realizations in each cycle. Therefore, the total velocity is reconstructed at 72Hz, 360Hz and 1800 Hz to investigate the events at low and high frequencies. The total velocity on cross sectional planes 0.25D upstream, 20°, 80°, 0.25D and 1D downstream, reconstructed at frequency of 72Hz corresponding to St ~ 1.3 along with contours of magnitude of transverse velocities are shown in Figure 4.49 through Figure 4.54. The results for the reconstructions at the higher frequencies of 360 Hz and 1800 Hz are included in Appendix B and Appendix C, respectively. At 0.25D upstream of the bend, the reconstructed total velocity contours (Figure 4.49) shows higher velocity near the wall and lower velocity near the pipe center. The contours can be seen to change in every realization suggesting high frequency LSM imparts a range of frequencies to the cross sectional flow, which is also seen in the high frequency reconstructions. The results at 20° plane (Figure 4.50) shows a high velocity region near the outer wall side oscillating about the symmetry plane. A cycle can be identified from τ = 0.7344 to 7.344 corresponding to a low frequency of approximately St~ 0.15 and high frequency events are not present. The low velocity structures near the outer wall occurs occasionally at τ = 4.4, 9.55. Further downstream, at the 80° plane the reconstructed velocity (Figure 4.51) shows two vortices oscillating about the symmetry plane with small amplitude. The results show evidence of St ~ 0.07 and St ~ 0.13 as seen in half cycle at τ = 0 and 5.87 (Figure 4.51) and a cycle from τ = 24.97 to 33.05 (Figure 4.52). The results in the plane 0.25D downstream of the bend (Figure 4.53) show that the two vortices oscillate with higher amplitude than that in the 80° plane as seen in τ = 2.94 to 11.02 suggesting low frequency oscillations at approximately St ~ 0.13. The high velocity region can be seen changing in strength on shorter time scale and may be related to flow separation on the inner wall. The flow at the cross sectional plane 1D downstream of the bend is more complex. The high velocity flow is found to sweep the inner wall alternatively as seen by Kalpakli et al. (2013). A similar secondary flow is also reported by Ono et al. (2011) and Carlsson et al.(2015). The high velocity regions on either side of

the symmetry plane dominates alternatively at high frequency, while the low frequency oscillations can be seen as movement of low velocity region on the outer wall side.

The reconstruction at the higher frequencies in the cross sectional planes upstream of the bend and at 20° bend angle showed no distinct high frequency events suggesting that high frequency LSM does not affect the secondary flow. The results in the latter half of the bend and in the downstream pipe show high frequency events which are related to high frequency (St ~ 0.5) flow separation on the inner wall. The low frequency oscillation on the cross sectional planes at 80° bend angle, 0.25D and 1D downstream seems to be extension of that found at 20° bend angle as the frequencies are similar at around St~ 0.07 and 0.13. The high frequency events in these planes show up as change in high velocity region in the 80° and 0.25D downstream cross sectional planes and as sweeping of high velocities on the inner wall from either side of the symmetry plane alternatively in the cross sectional plane 1D downstream. This sweeping high velocity leads to alternate domination of one vortex in the pair of vortices and nearly resembles the swirl switching described in the literature. The frequency related to this alternative domination of vortex is about St ~ 0.3 - 0.5. Thus, the unsteadiness in the secondary flow in the bend can be considered to have both low and high frequency structures. The oscillations of two vortices about the symmetry plane constitutes low frequency events which are found to be present in all planes from the 20° bend angle to the 1D downstream plane. The high frequency structures are related to the flow separation on the inner wall and are present in the planes beyond the separation point (from the 70° cross sectional plane). These high frequency events are dominant at the cross sectional plane 1D downstream and leads to the alternate domination of one vortex between the pair of vortices resulting in swirl switching.

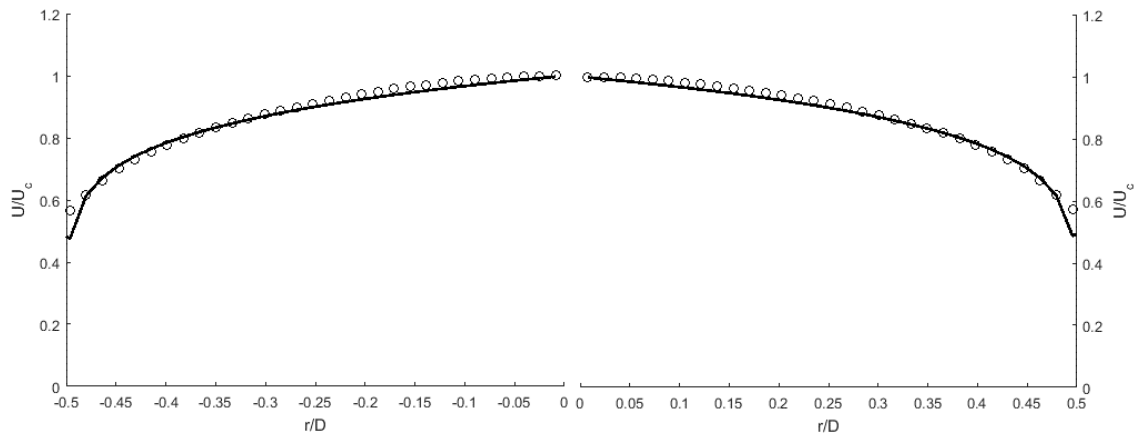

(a) (b)

Figure 4.1 Spatially averaged mean velocity profile compared with the power law profile for (a) Outer wall side (b) Inner wall side.

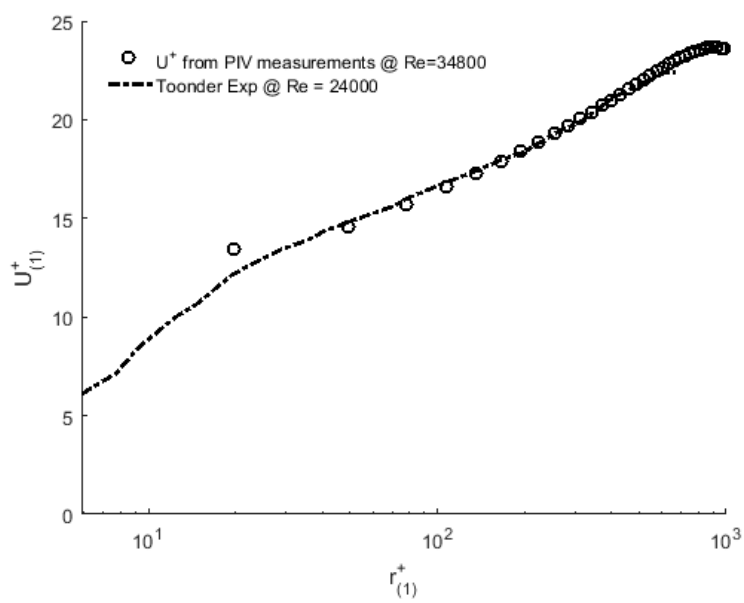

Figure 4.2 Mean velocity profile in wall units compared with LDV data.

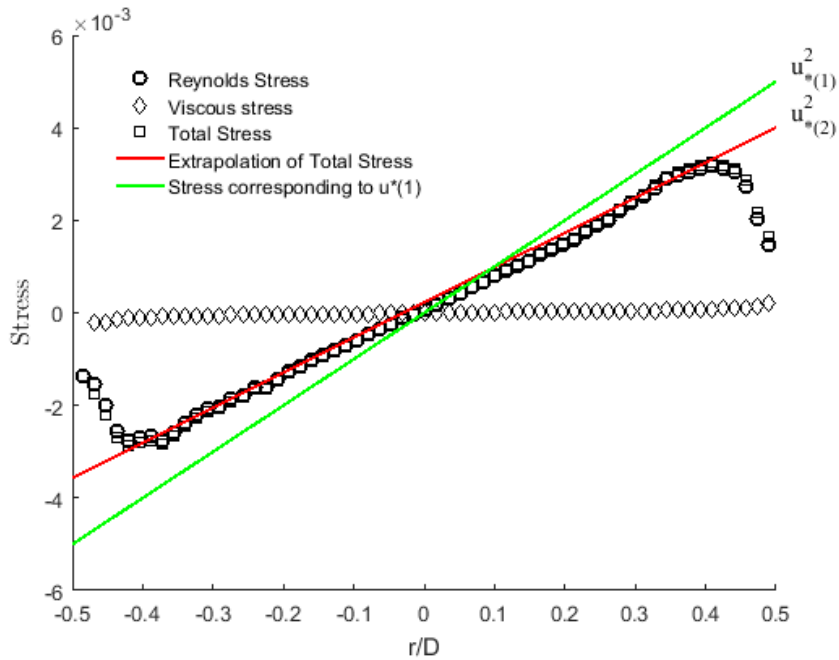

Figure 4.3 Reynolds stress, Viscous stress, total stress profiles and linear fit to find $u^*_{(2)}$.

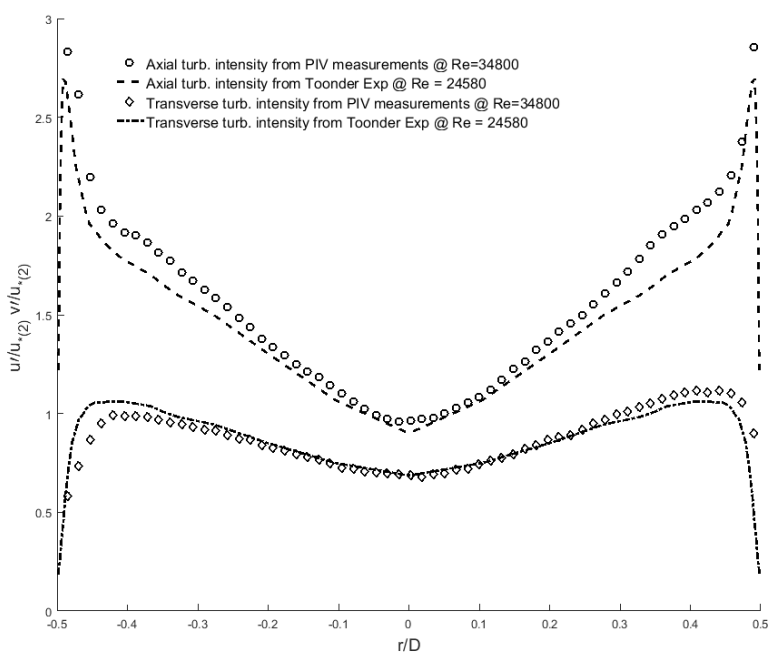

Figure 4.4 Turbulence intensity profiles normalized by the $u^*_{(2)}$.

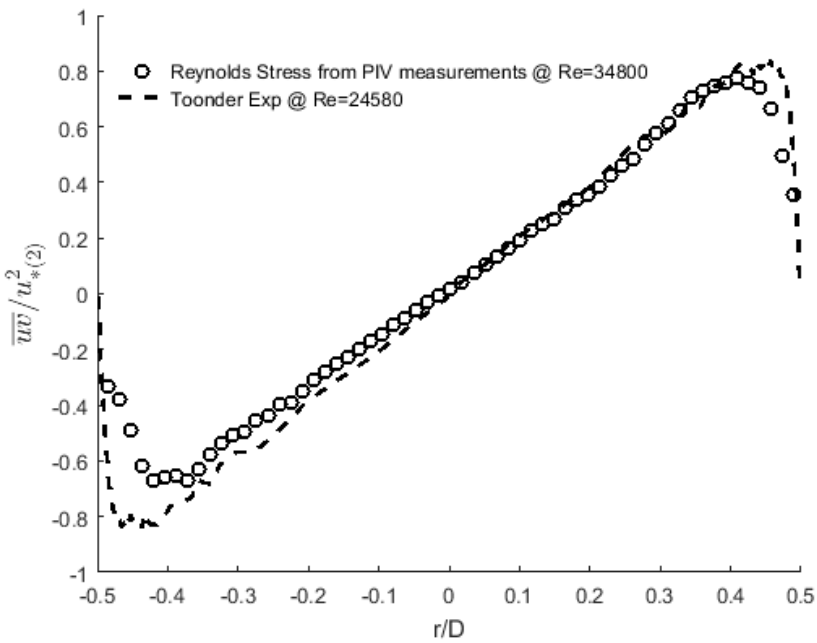

Figure 4.5 Reynolds stress profiles normalized by $u^*_{(2)}$.

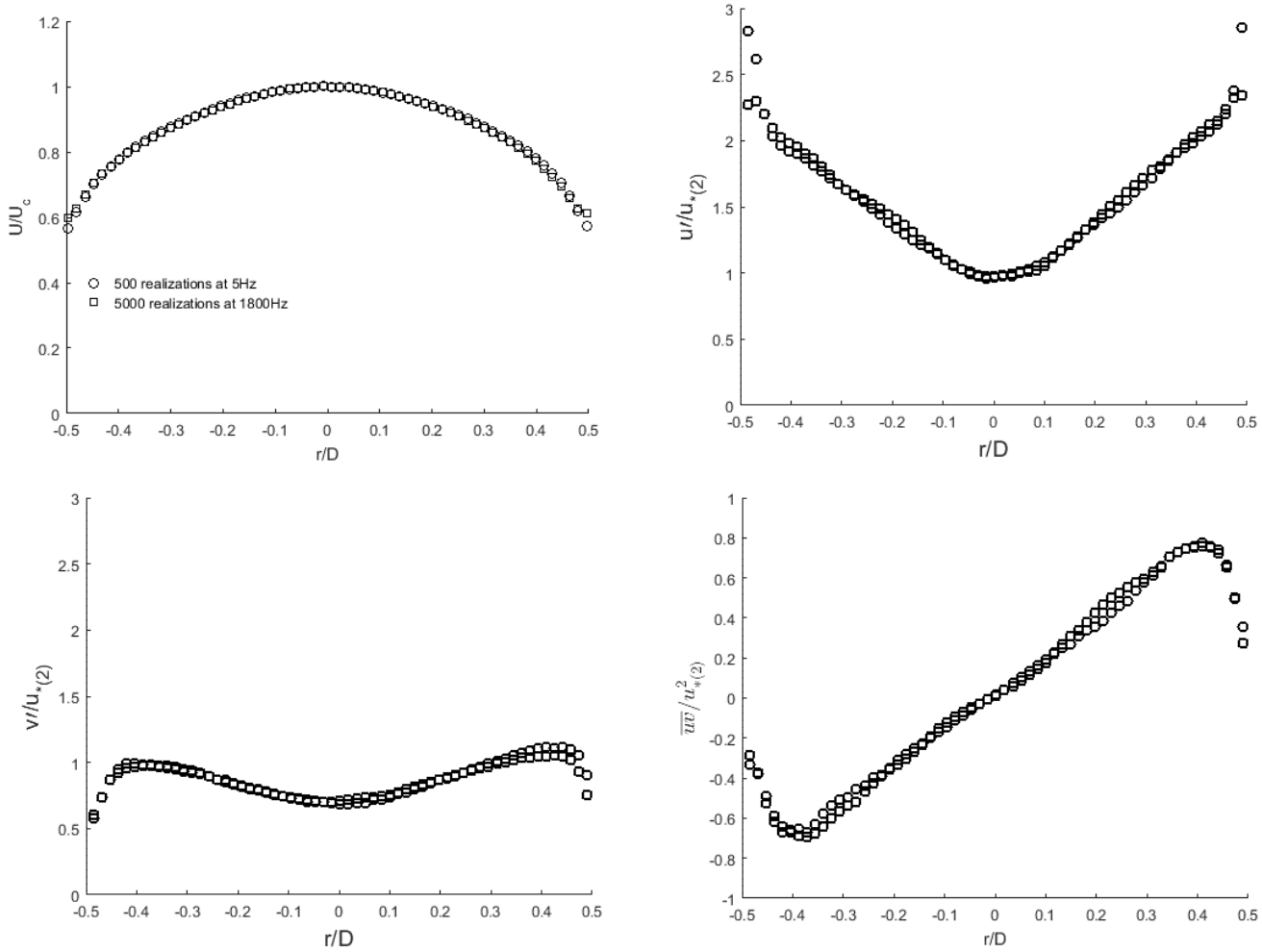

Figure 4.6 Comparison of Reynolds average measurements obtained from 500 realizations at 5Hz and 5000 realizations at 1800Hz.

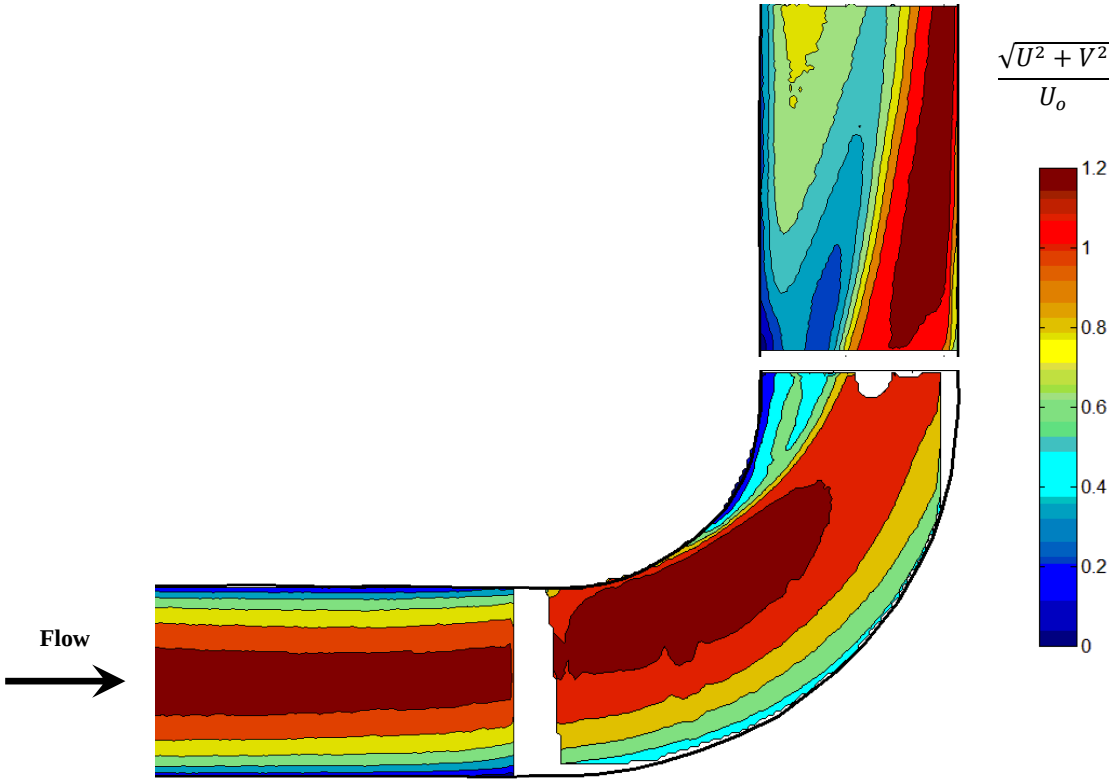

Figure 4.7 Contours of velocity magnitude in axial symmetric plane

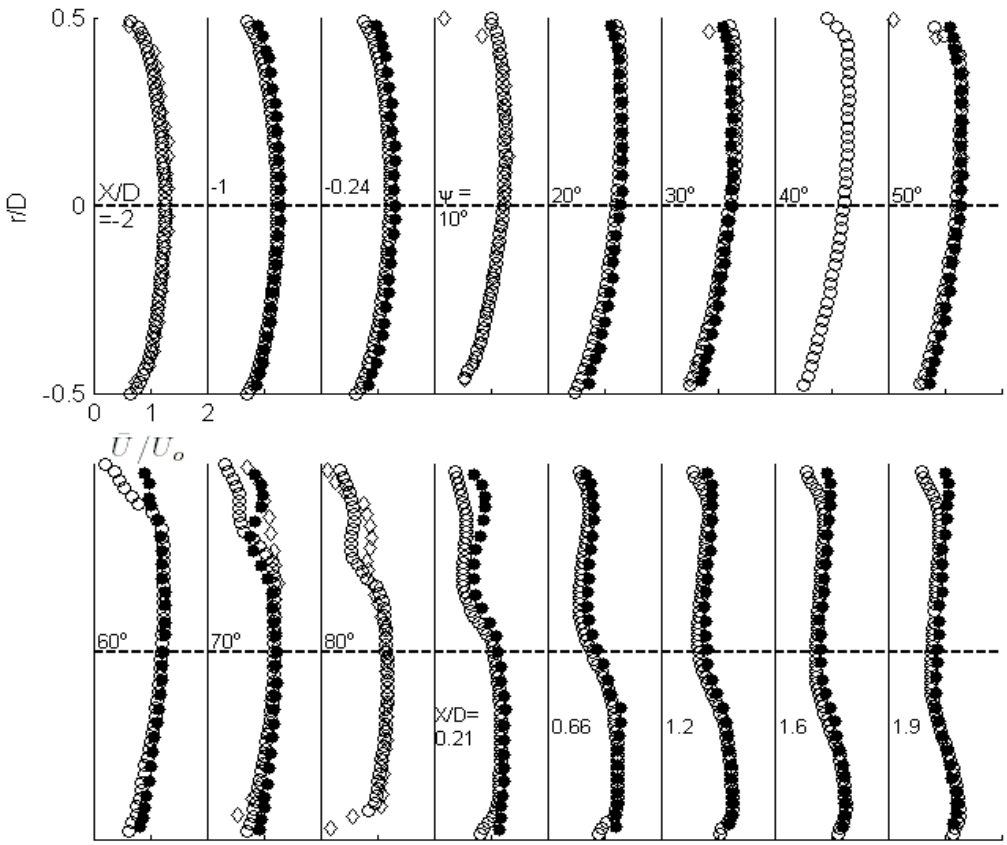

Figure 4.8 Streamwise normalized axial velocity profiles at symmetry plane.○ current experiments for Rc/D= 1.5 and Re=34800 and for • Rc/D = 2.0, Re = 60000 from Sudo et al.(1998)and ◊ Rc/D= 1.5 and Re = 40000 from Mazher et. al.(2016)

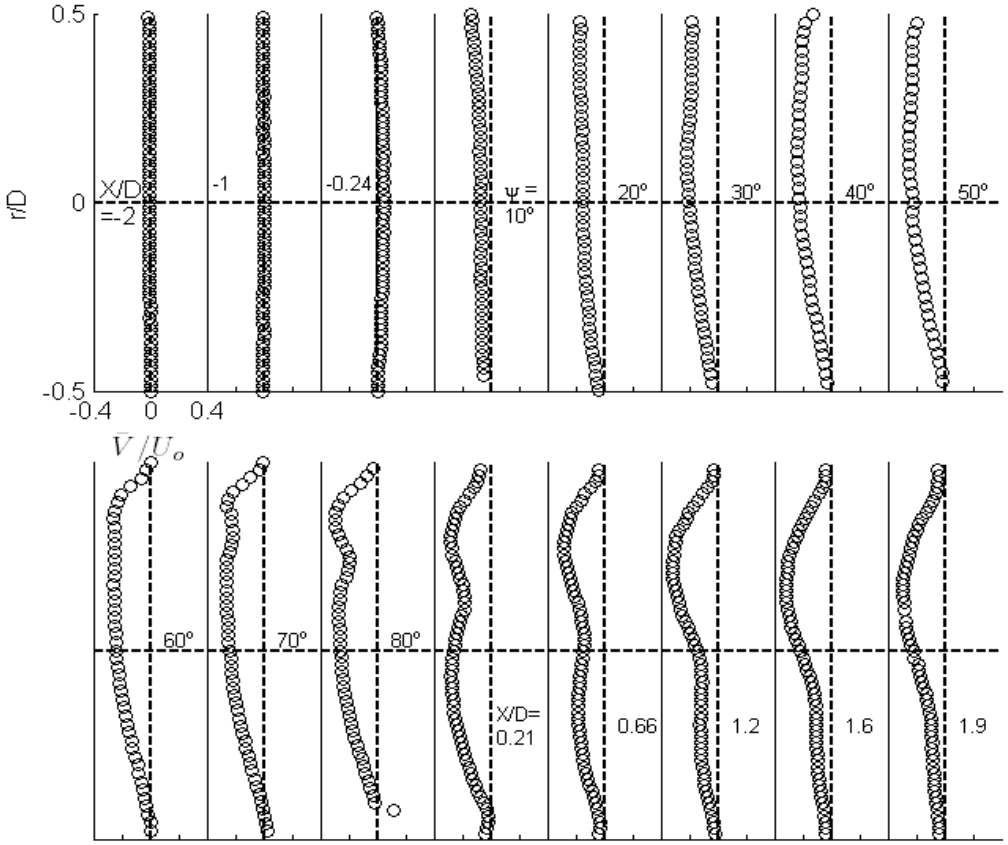

Figure 4.9 Streamwise normalized transverse velocity profile in axial symmetric plane.

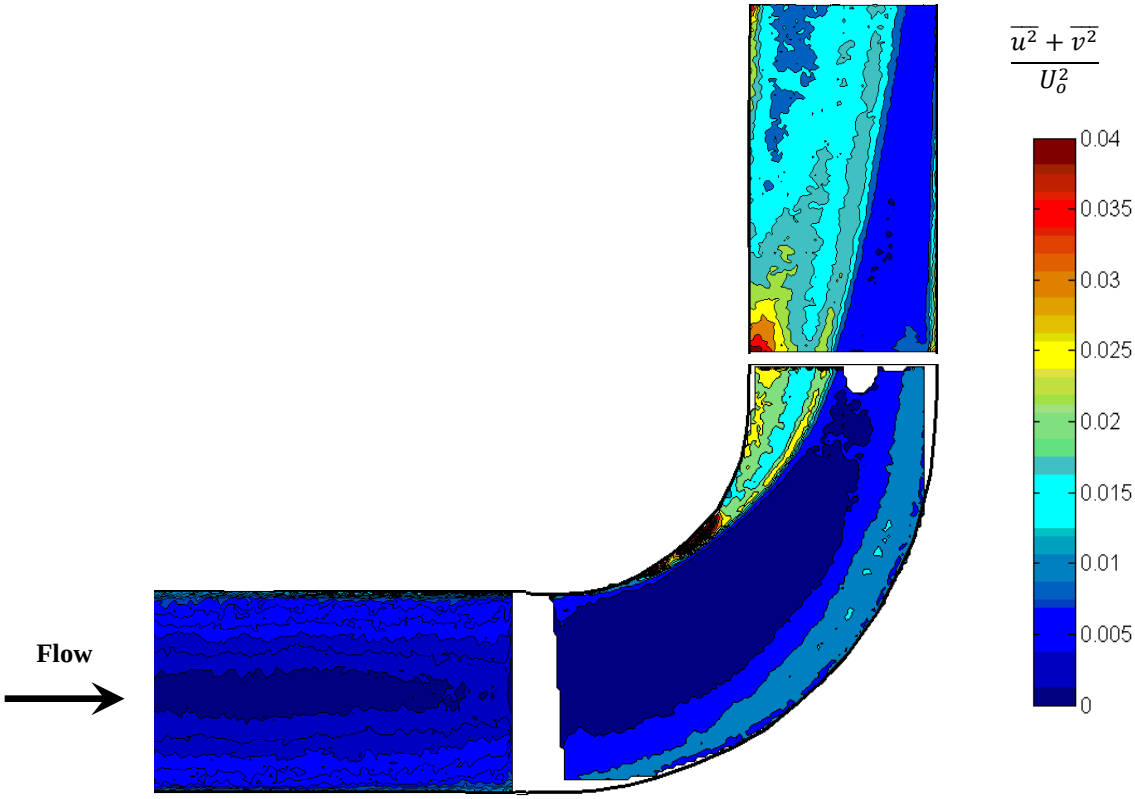

Figure 4.10 Contours of averaged turbulent kinetic energy in axial symmetric plane.

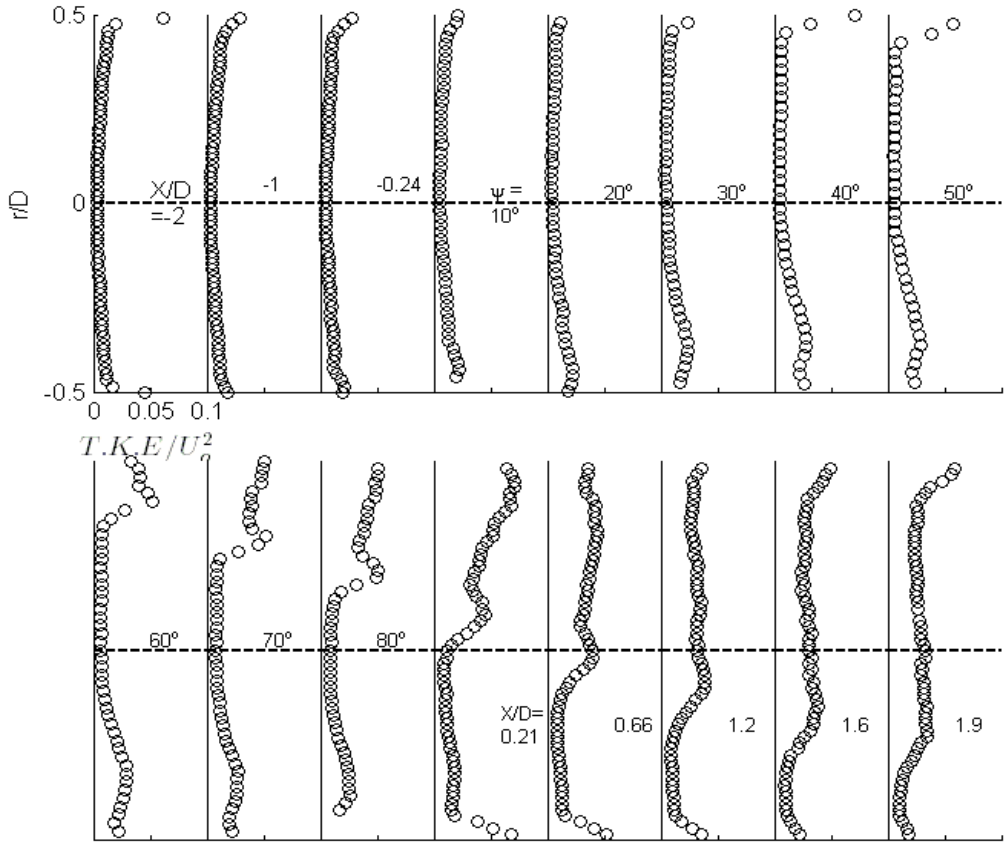

Figure 4.11 Streamwise normalized turbulent kinetic energy profile in axial symmetric plane.

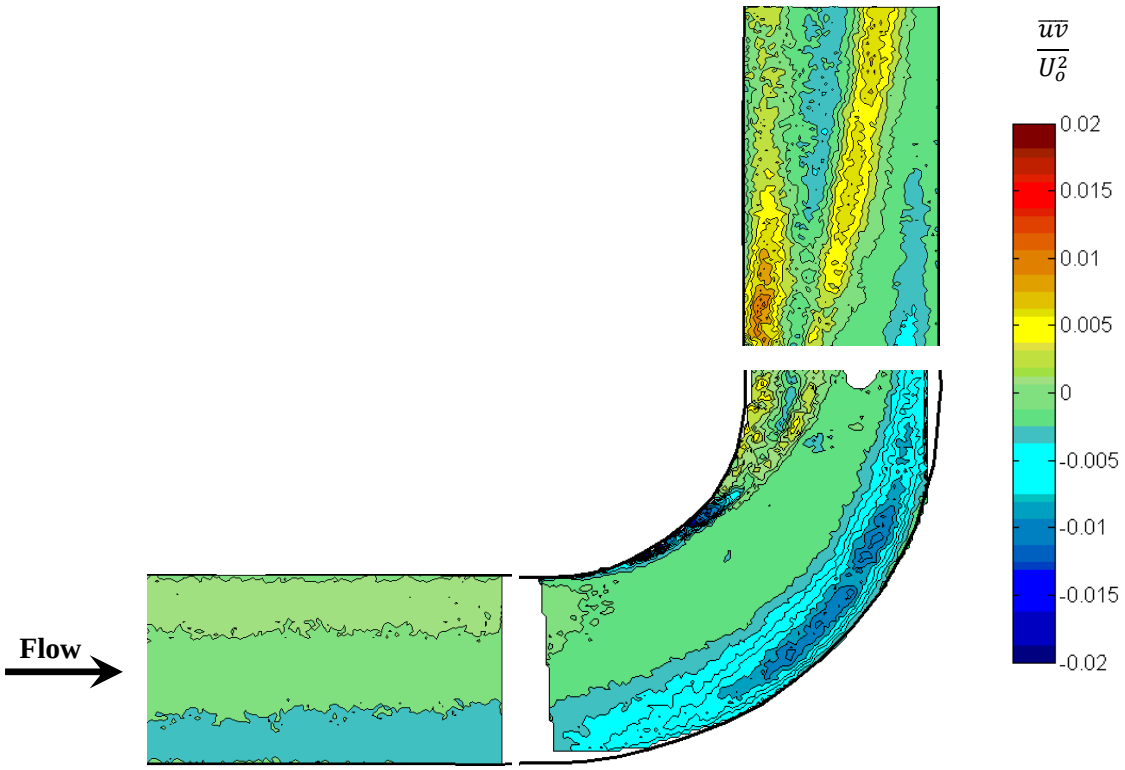

Figure 4.12 Contours of normalized Reynolds shear stress in axial symmetric plane.

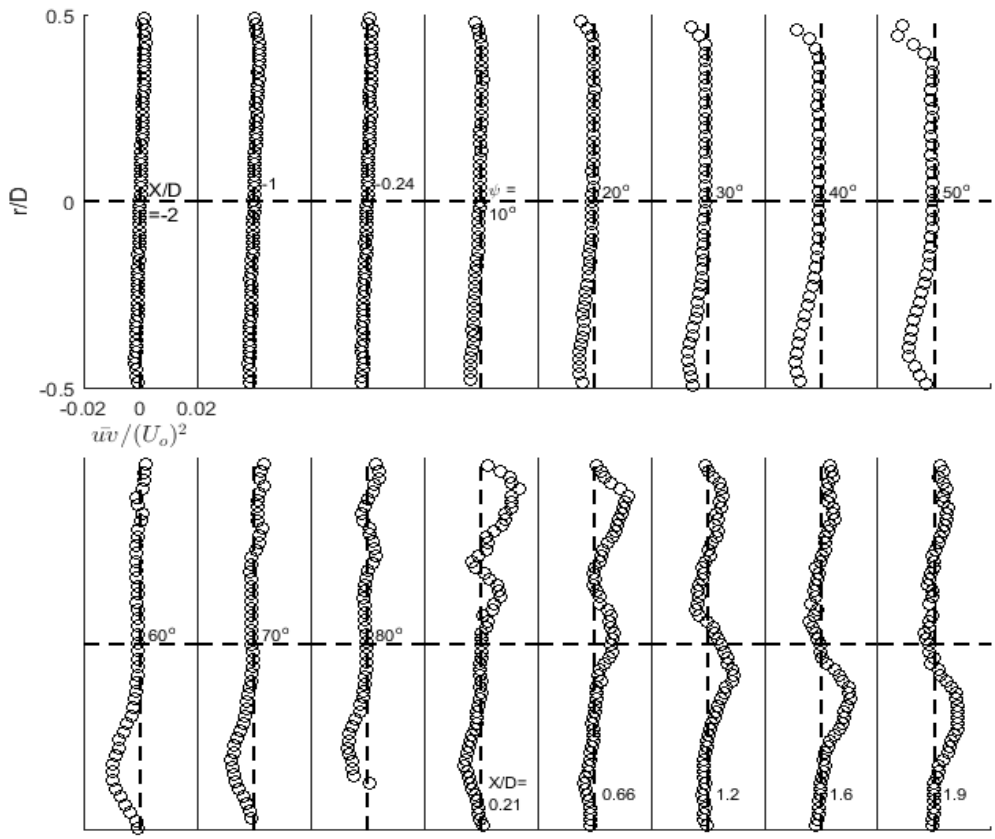

Figure 4.13 Streamwise profiles of Reynolds shear stress

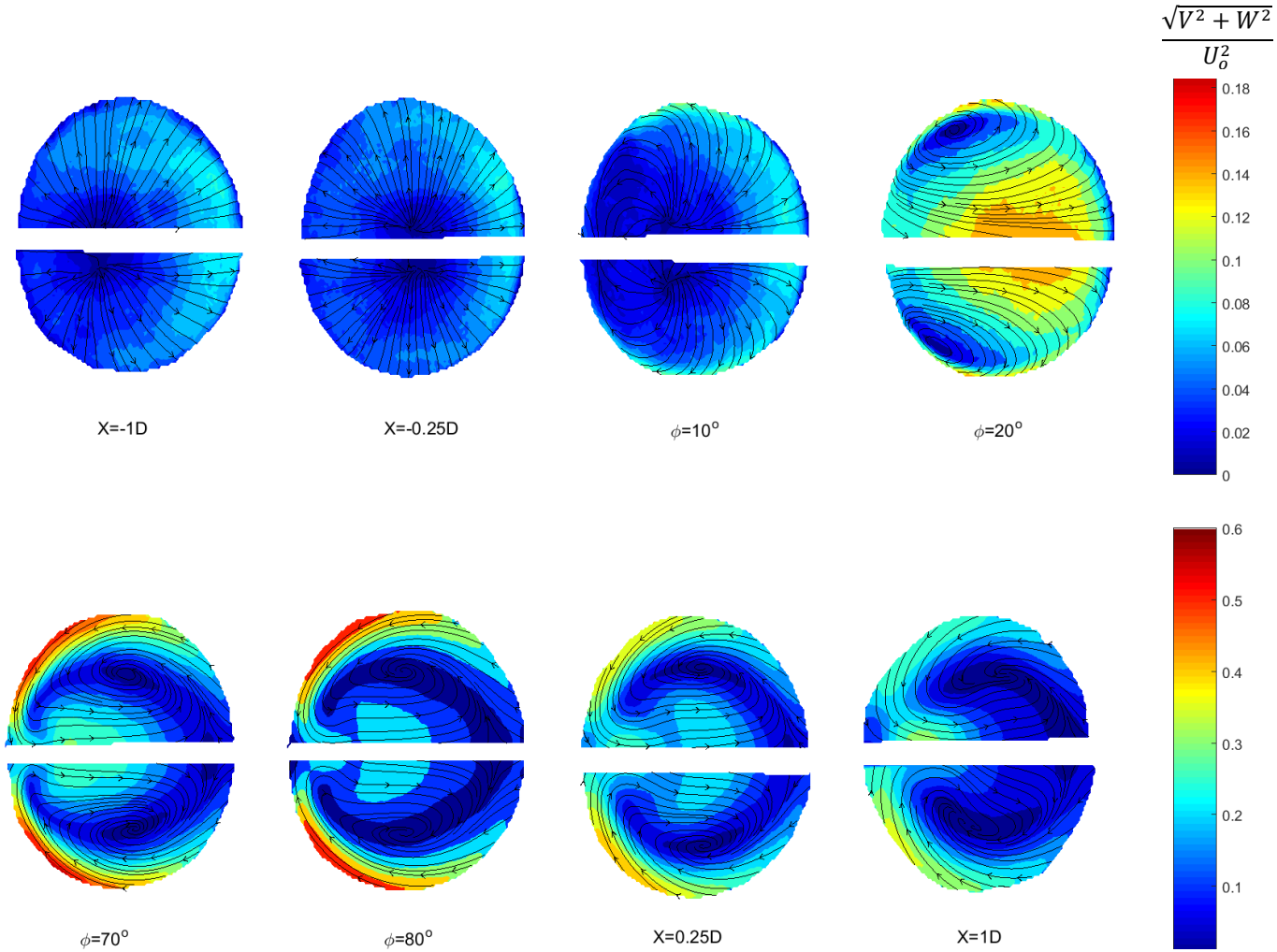

Figure 4.14 Cross sectional mean velocity contours at different planes. Streamlines showing the direction of secondary flow.

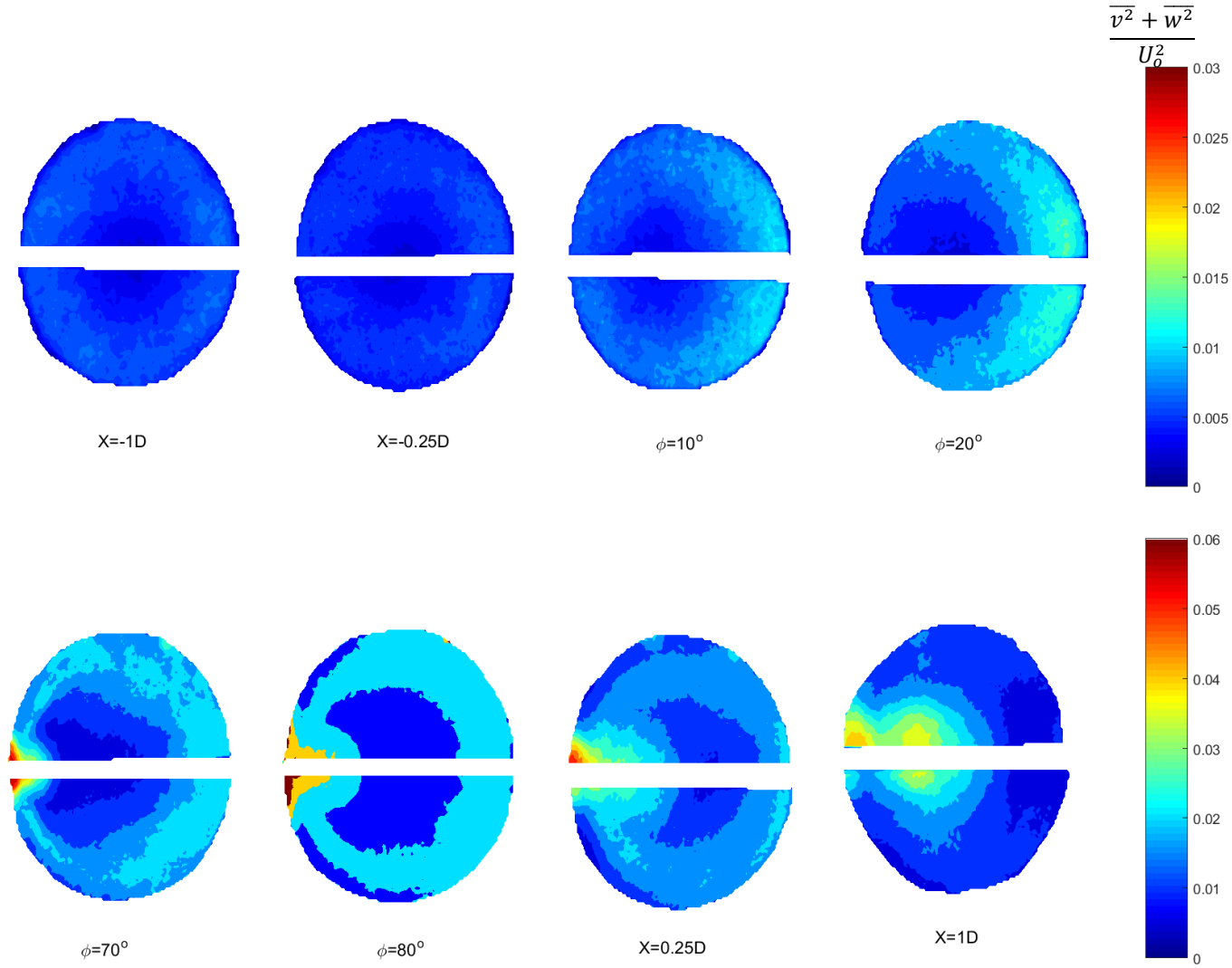

Figure 4.15 Cross sectional turbulent kinetic energy contours at different planes.

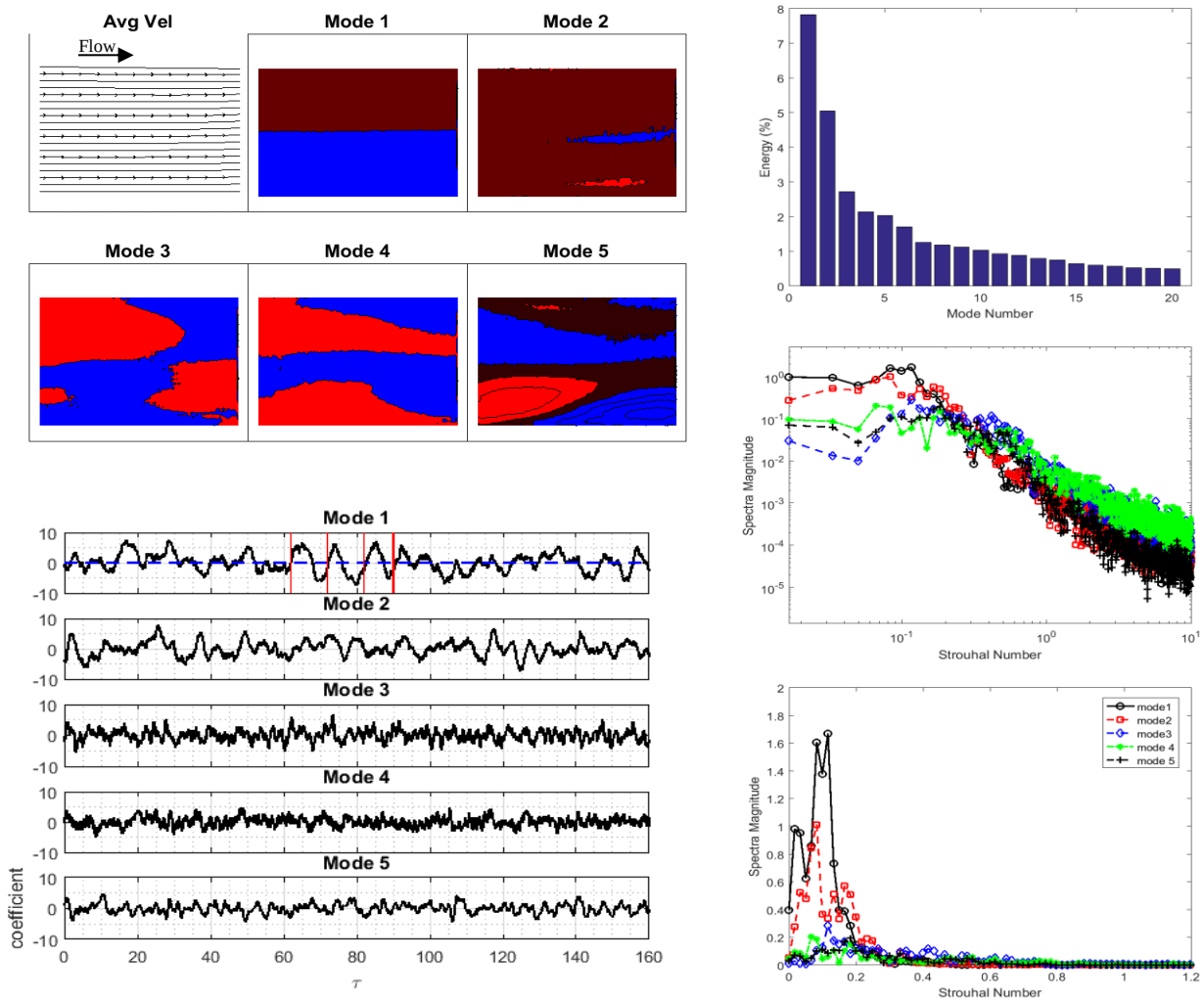

Figure 4.16 Time evolution of coefficients of modes, mode shapes, PSD of mode coefficients (linear and log log) plot at axial cross section of upstream pipe.

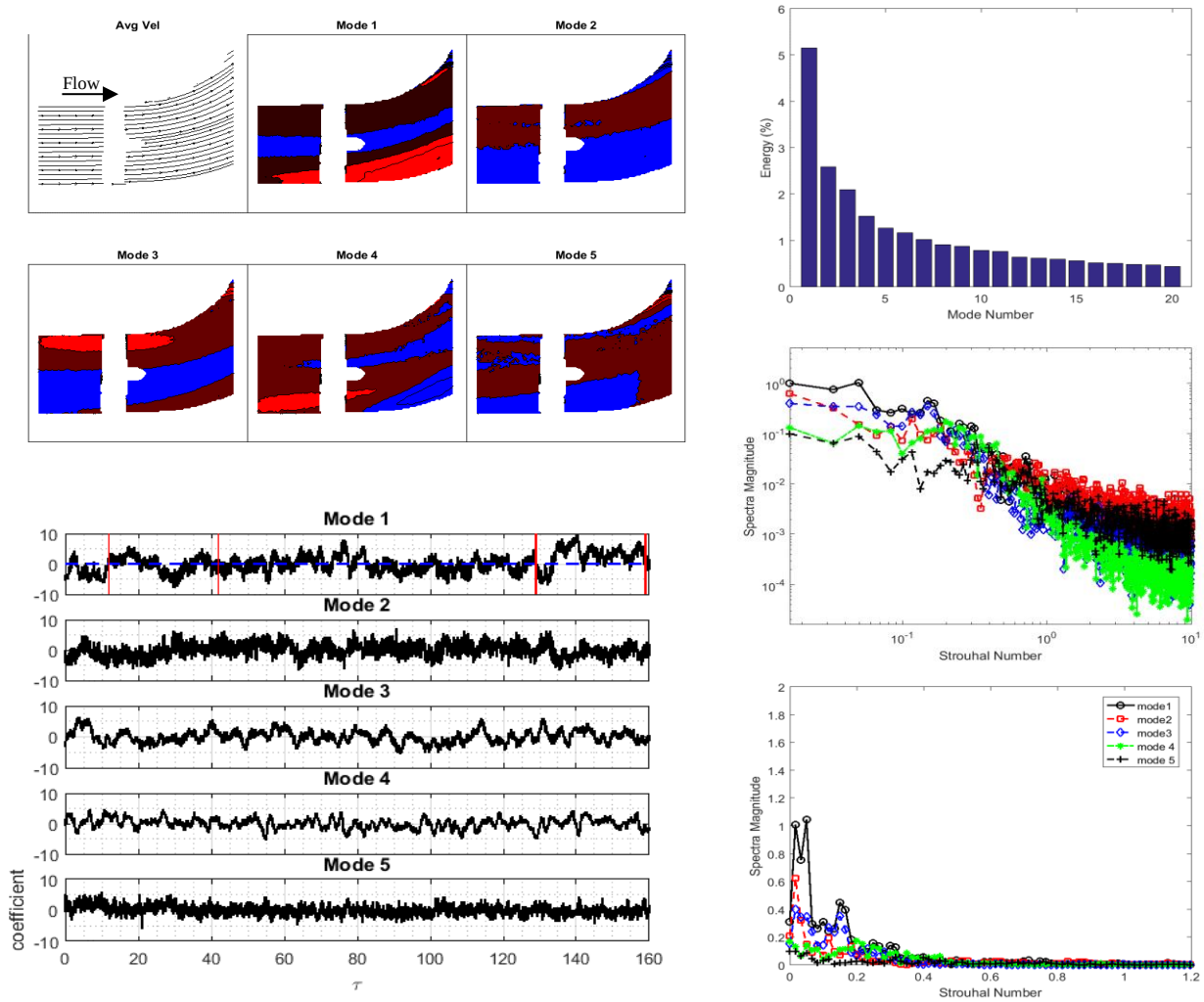

Figure 4.17 Time evolution of coefficients of modes, mode shapes, PSD of mode coefficients (linear and log log) plot at axial cross section of upstream and inlet section of bend.

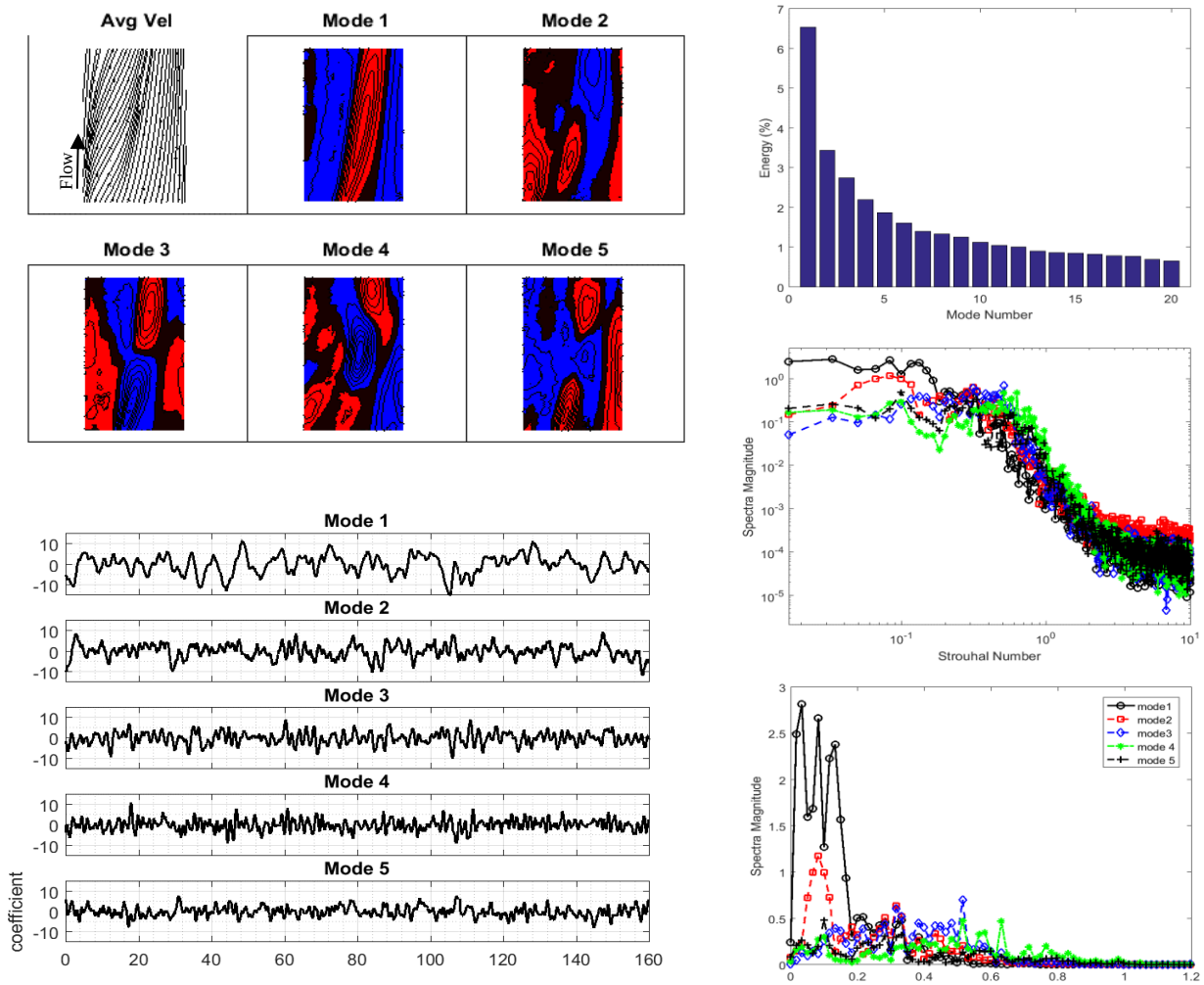

Figure 4.18 Time evolution of coefficients of modes, mode shapes, PSD of mode coefficients (linear and log log) plot at axial cross section of downstream section of bend.

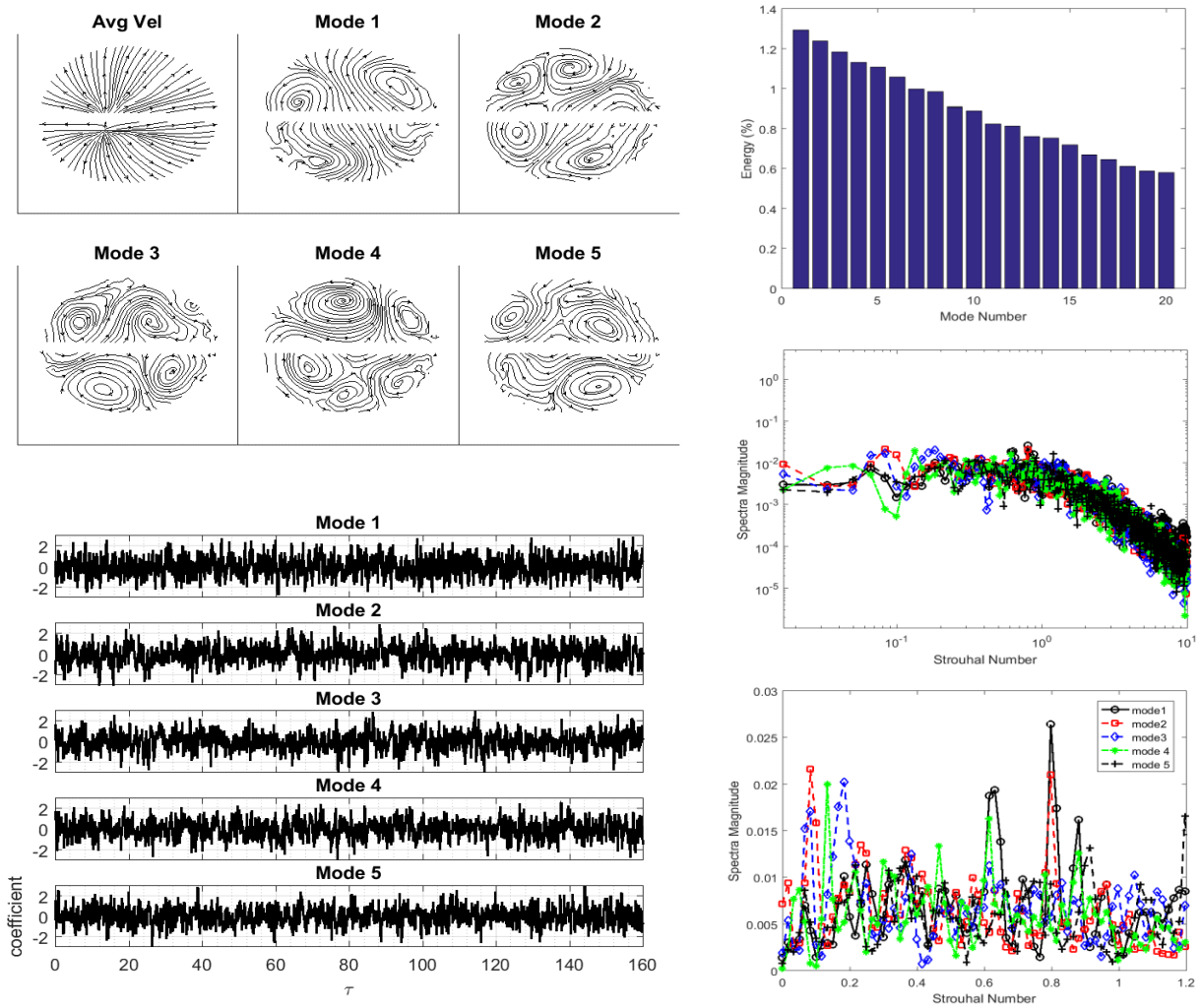

Figure 4.19 Time evolution of coefficients of modes, mode shapes, PSD of mode coefficients (linear and log log) plot at 1D upstream.

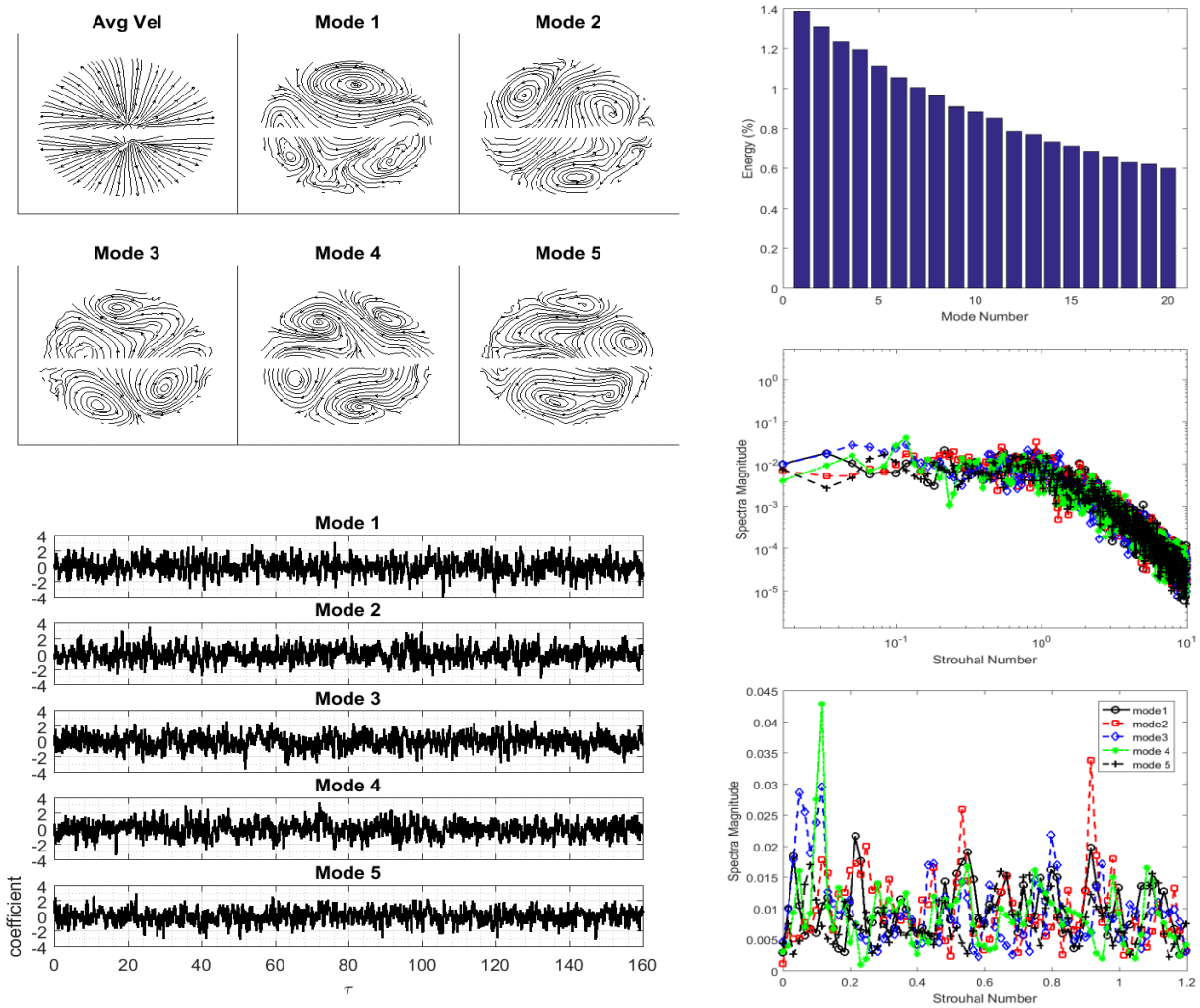

Figure 4.20 Time evolution of coefficients of modes, mode shapes, PSD of mode coefficients (linear and log log) plot at 0.25D upstream.

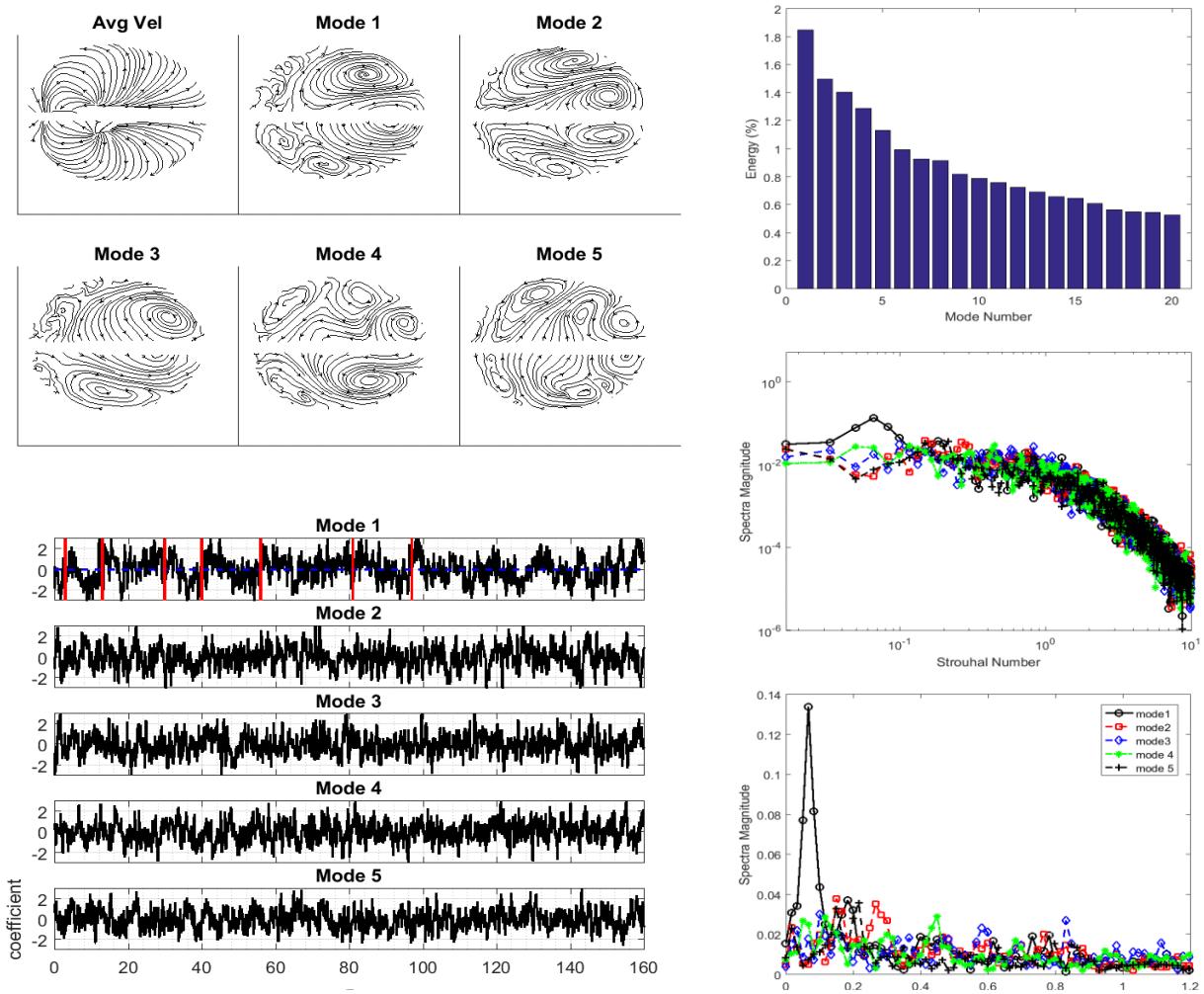

Figure 4.21 Time evolution of coefficients of modes, mode shapes, PSD of mode coefficients (linear and log log) plot at 10° plane.

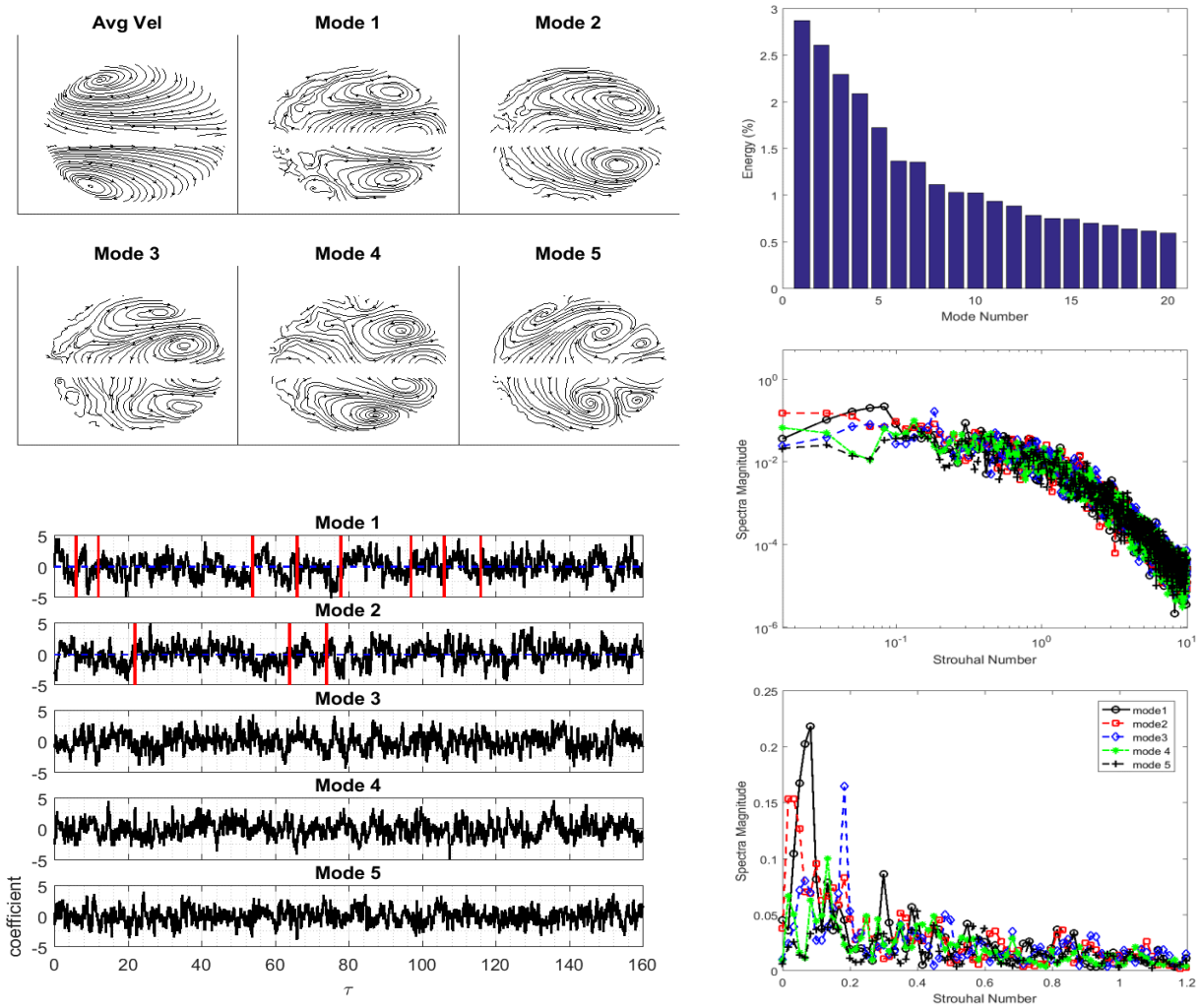

Figure 4.22 Time evolution of coefficients of modes, mode shapes, PSD of mode coefficients (linear and log log) plot at 20° plane.

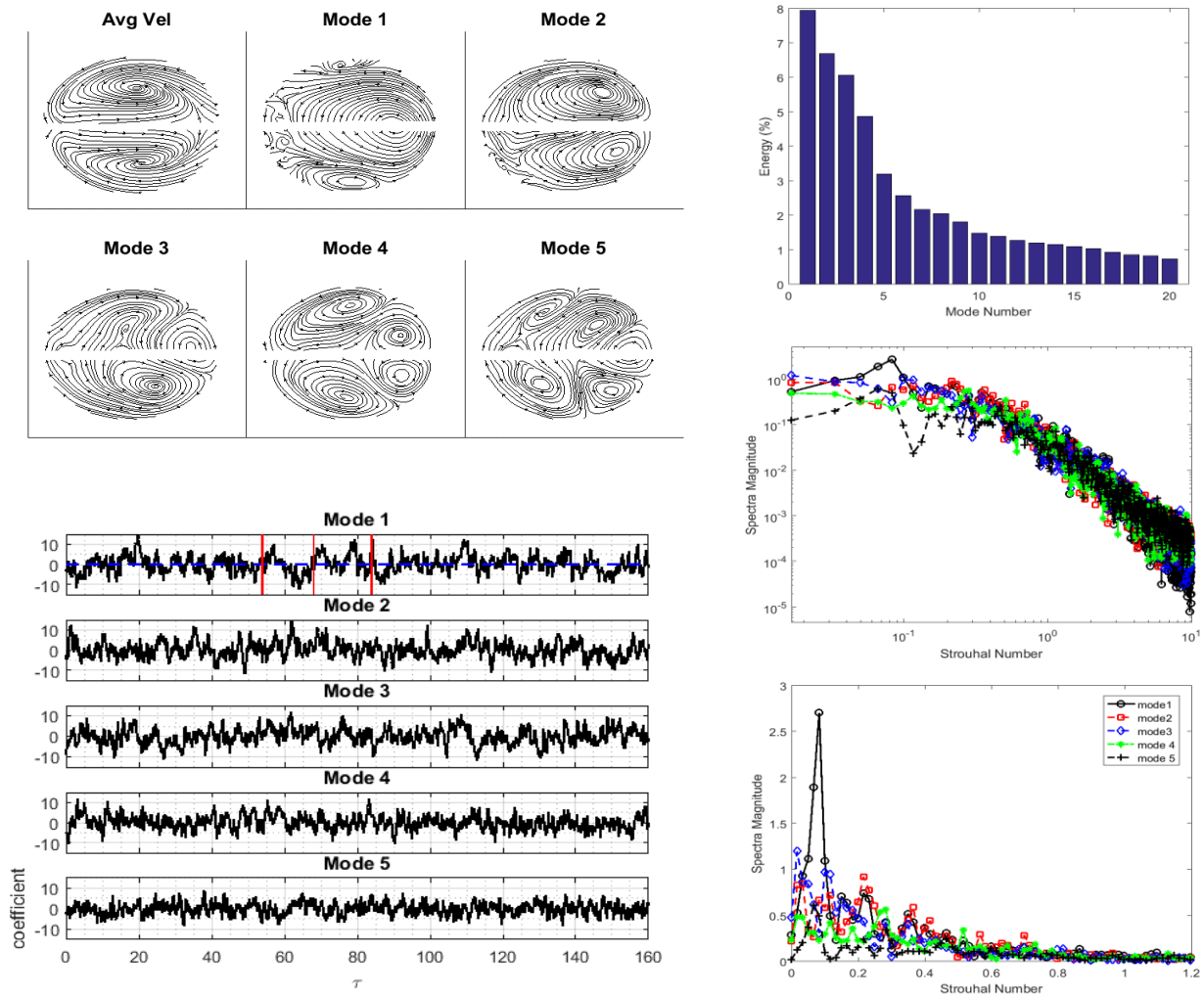

Figure 4.23 Time evolution of coefficients of modes, mode shapes, PSD of mode coefficients (linear and log log) plot at 70° plane.

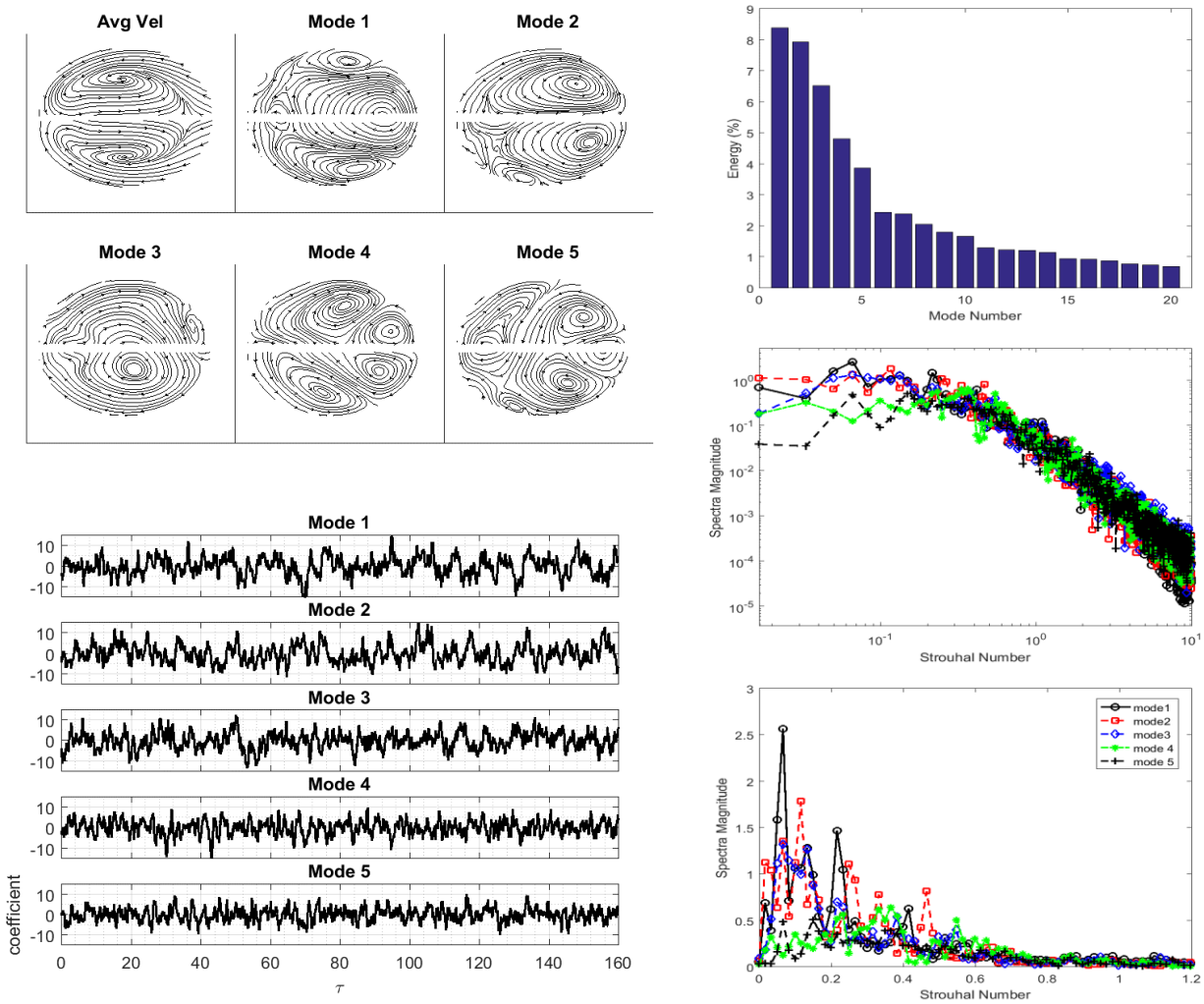

Figure 4.24 Time evolution of coefficients of modes, mode shapes, PSD of mode coefficients (linear and log log) plot at 80° plane.

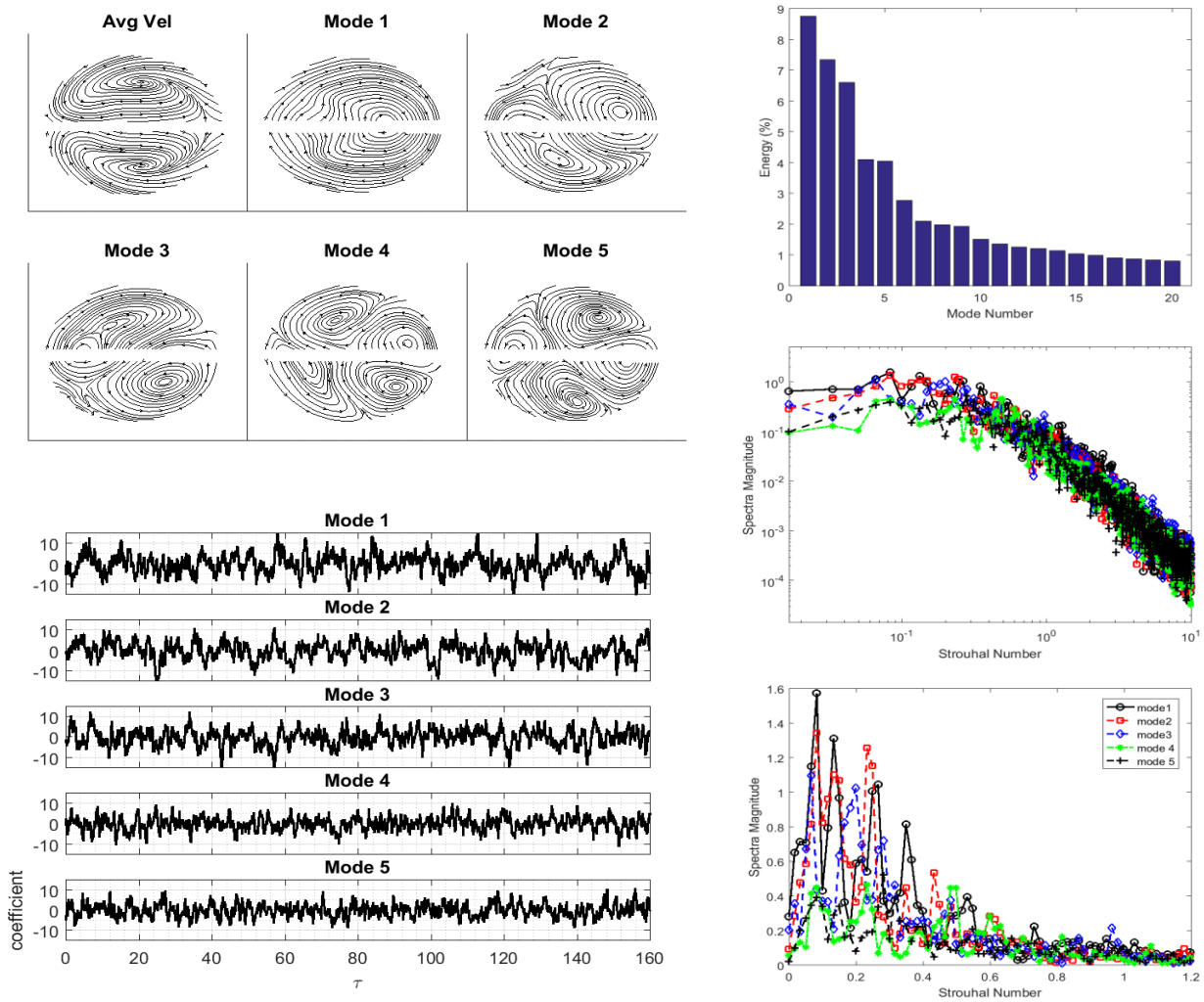

Figure 4.25 Time evolution of coefficients of modes, mode shapes, PSD of mode coefficients (linear and log log) plot at 0.25 D downstream.

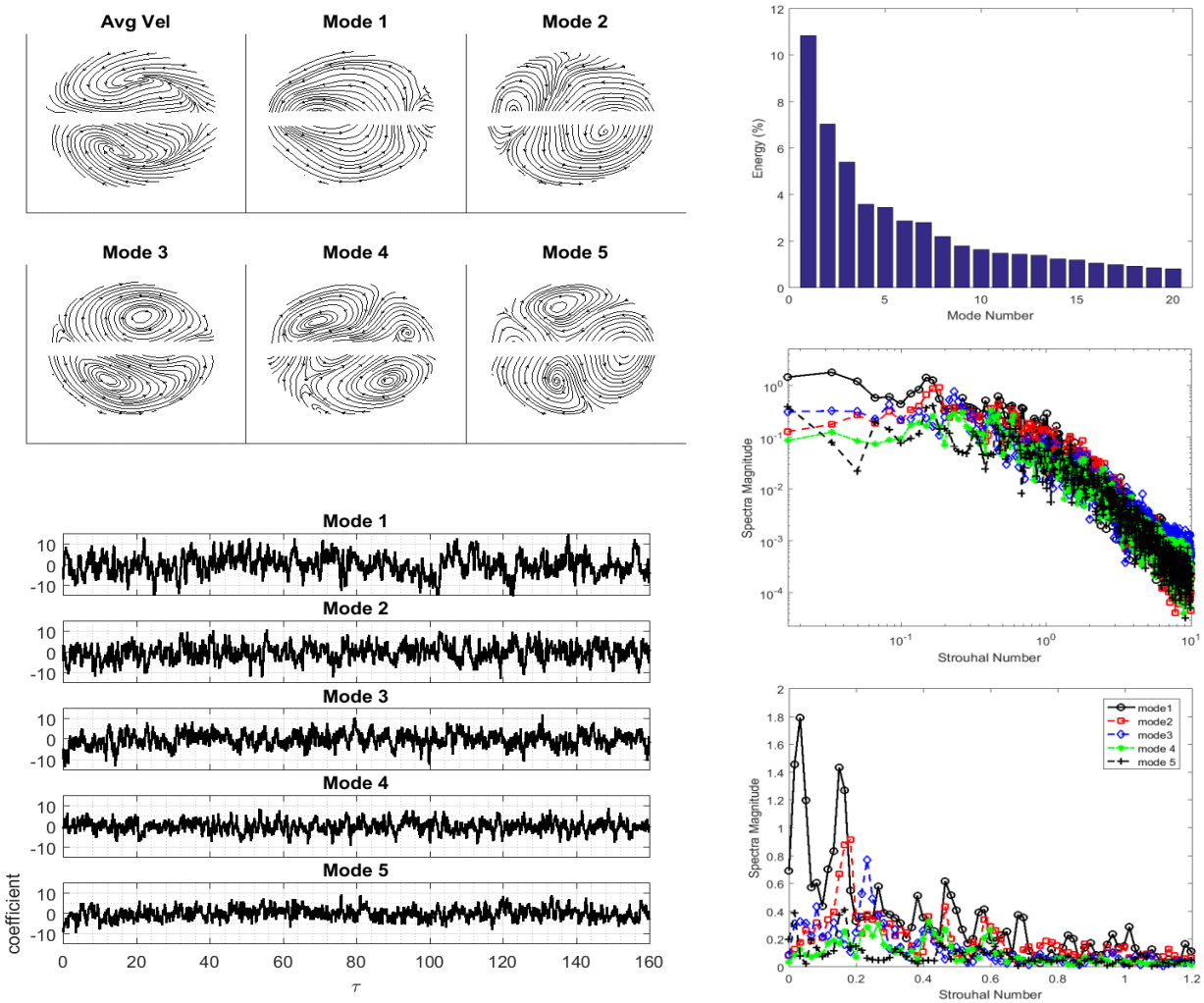

Figure 4.26 Time evolution of coefficients of modes, mode shapes, PSD of mode coefficients (linear and log log) plot at 1 D downstream.

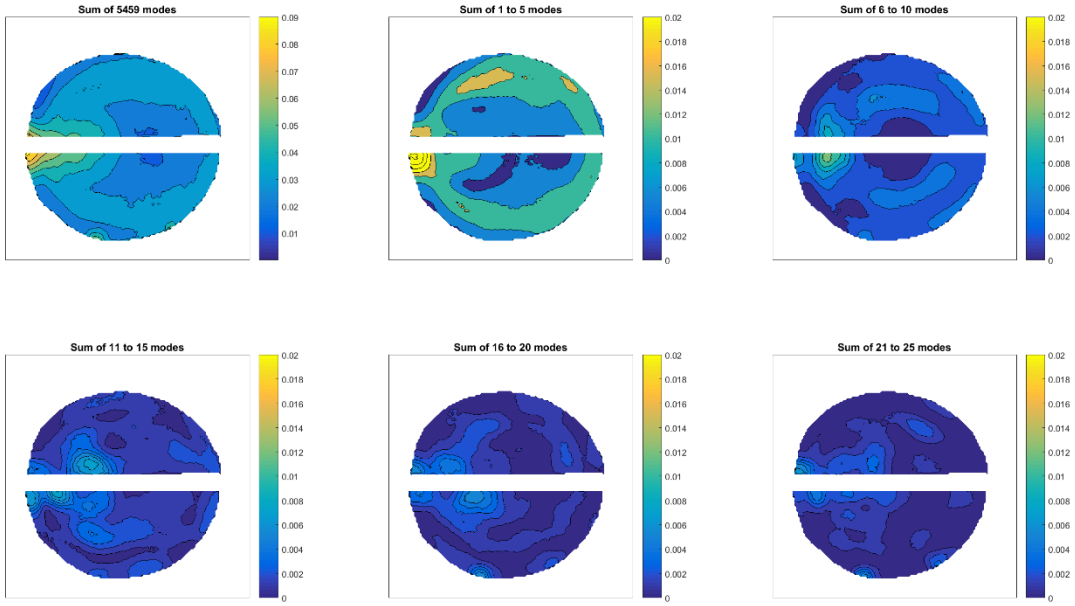

Figure 4.27 Reconstruction of Reynolds stress with successive 5 modes at 0.25 D.

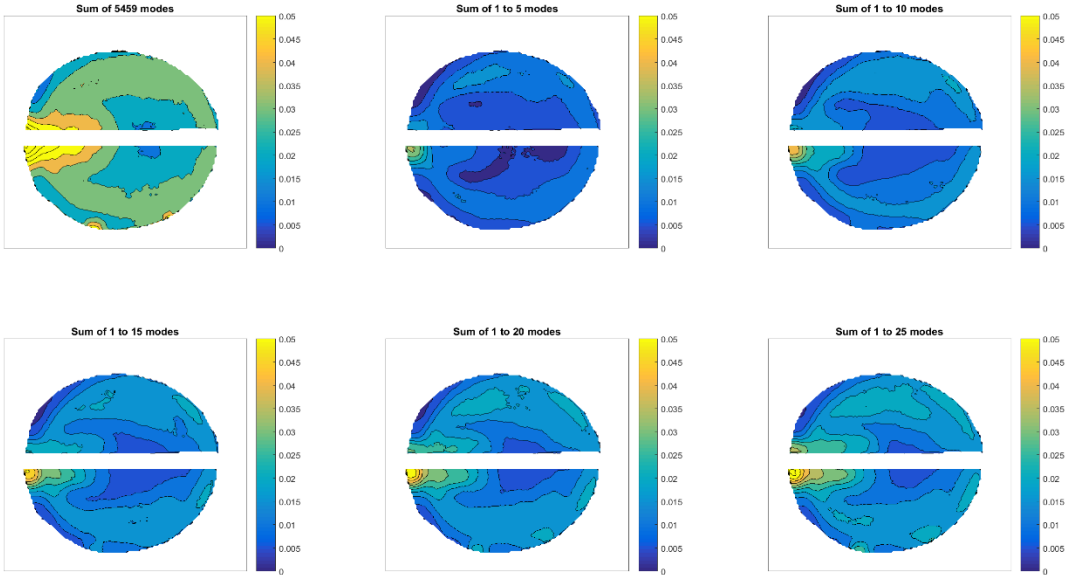

Figure 4.28 Reconstruction of Reynolds stress with different number of modes at 0.25 D.

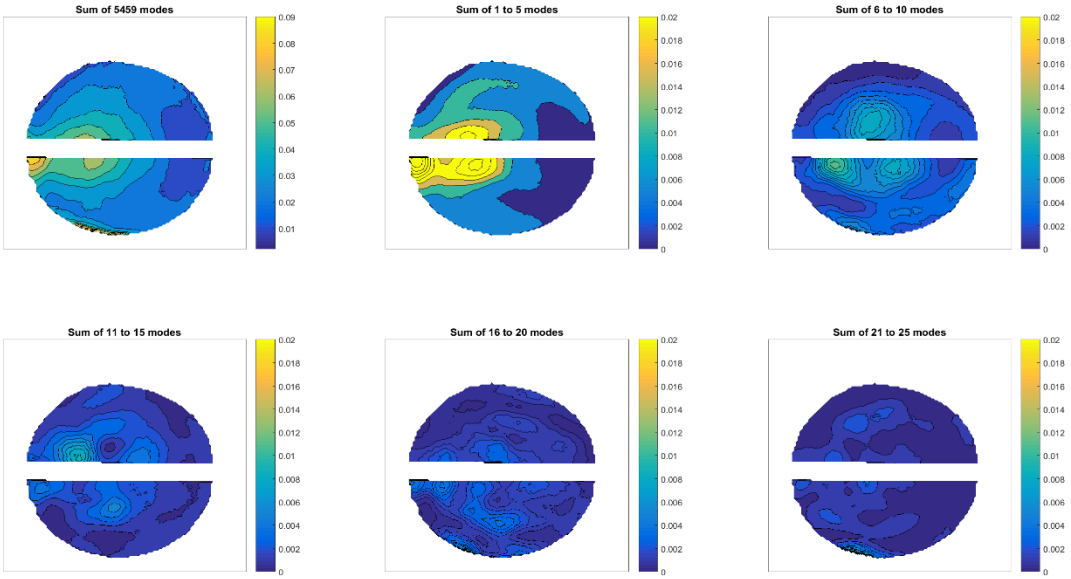

Figure 4.29 Reconstruction of Reynolds stress with successive 5 modes at 1 D

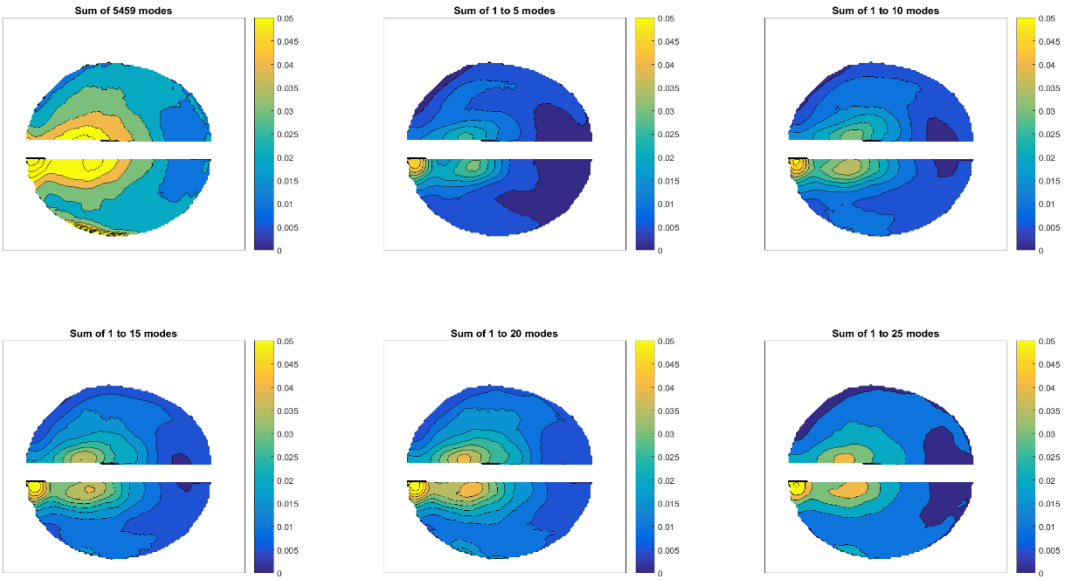

Figure 4.30 Reconstruction of Reynolds stress with different number of modes at 1D

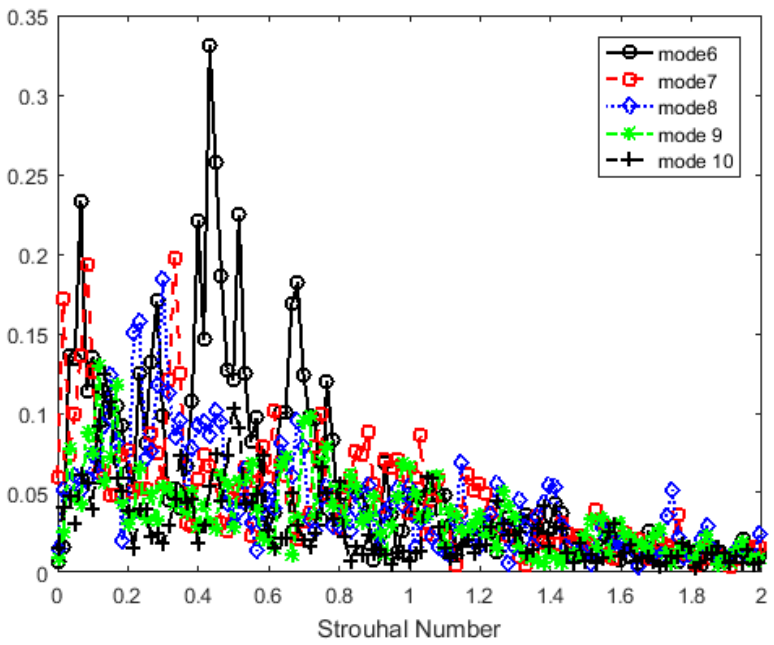

Figure 4.31 Spectra of modes 6-10 at downstream plane of 0.25 D

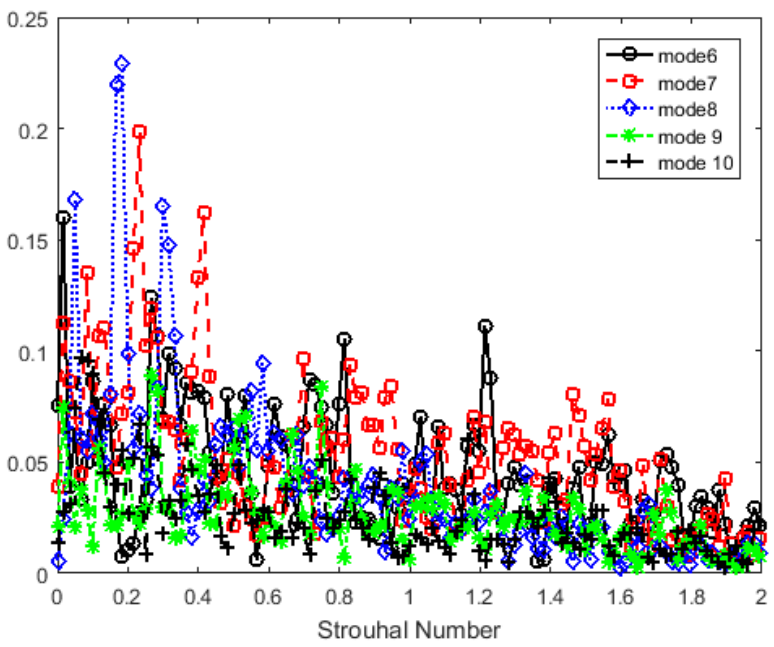

Figure 4.32 Spectra of modes 6-10 at downstream plane of 1D

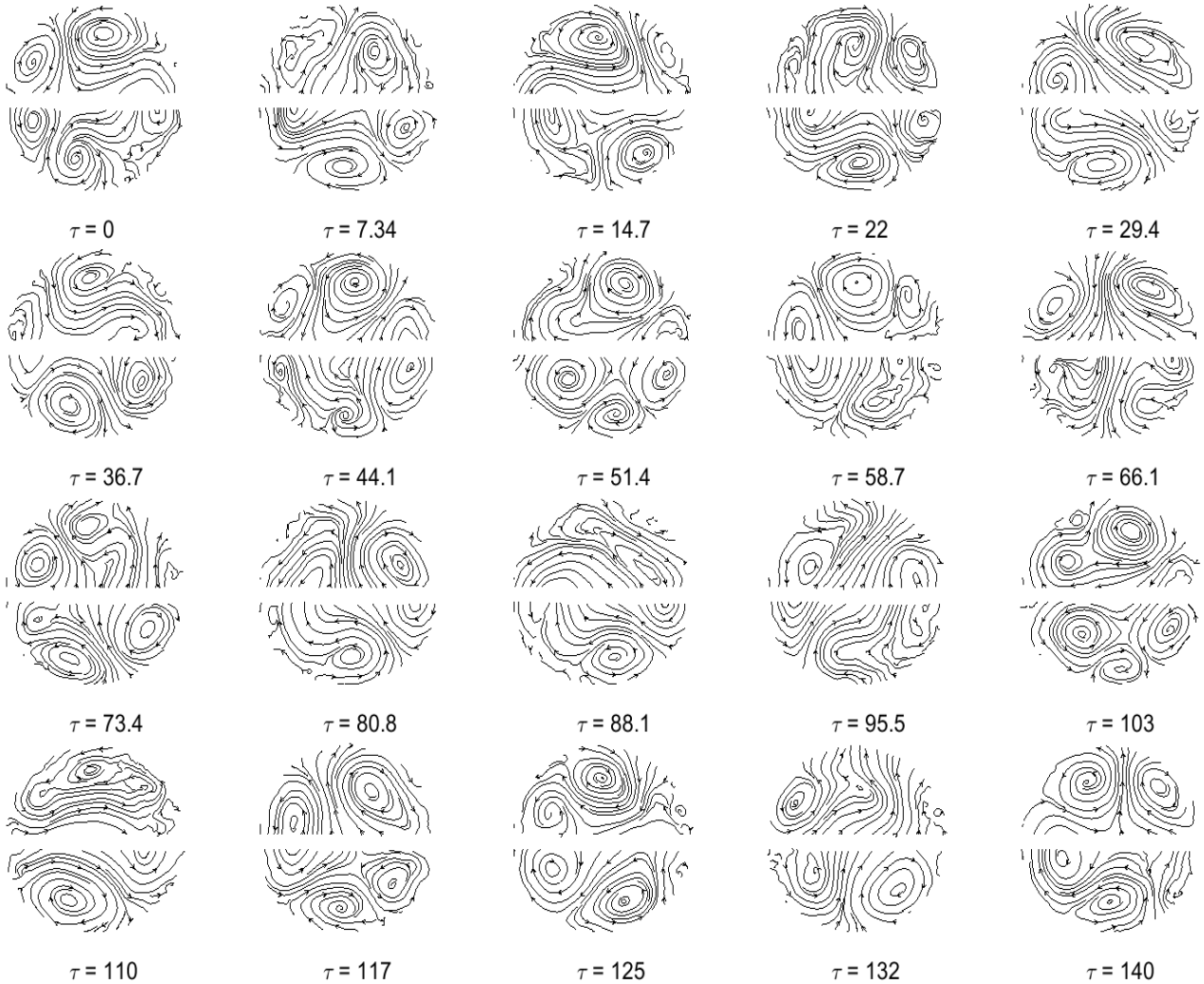

Figure 4.33 Reconstruction of fluctuations with first six modes on cross section plane 1D upstream at 7.2Hz.

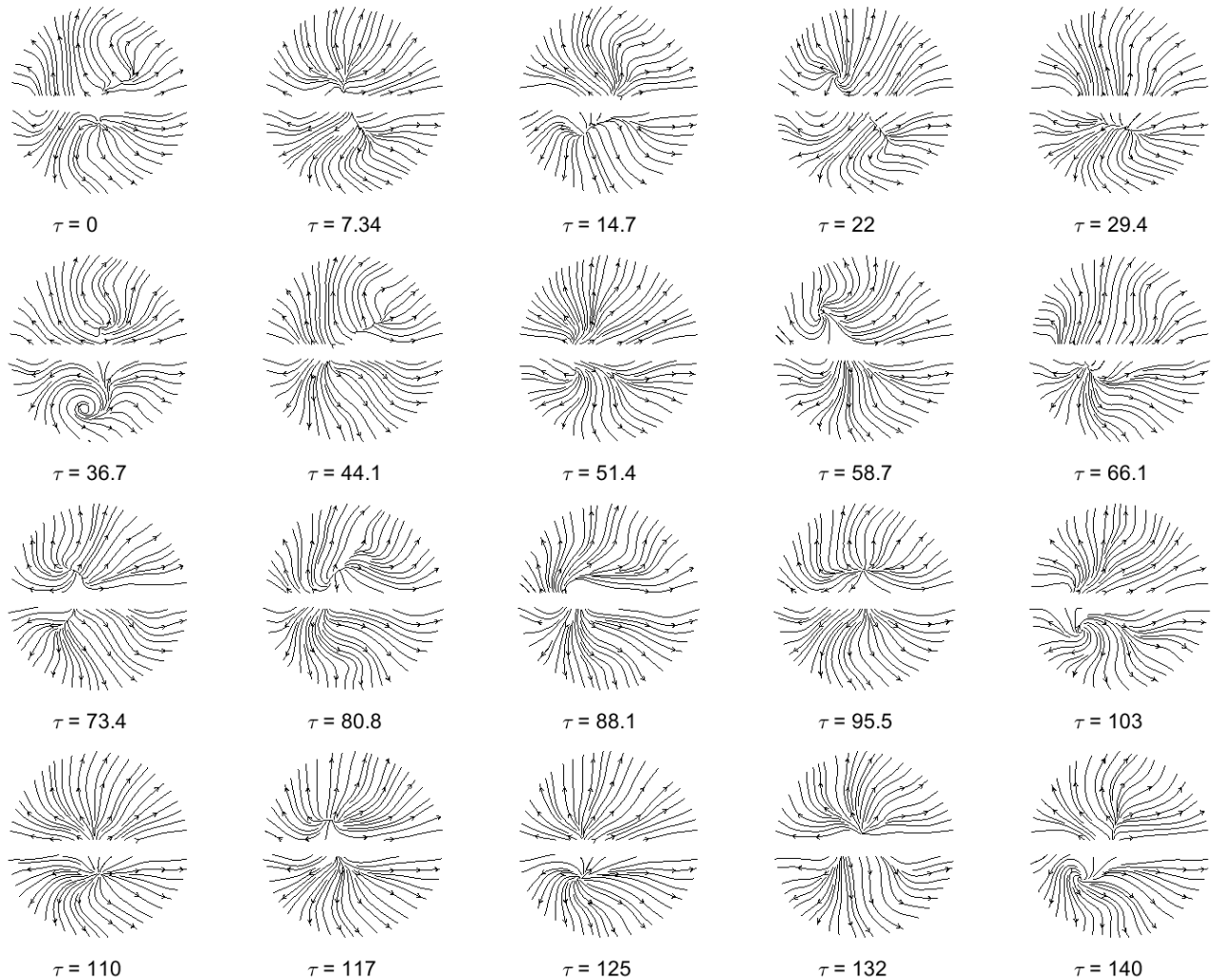

Figure 4.34 Reconstruction of total velocity with first six modes on cross section plane 1D upstream at 7.2Hz.

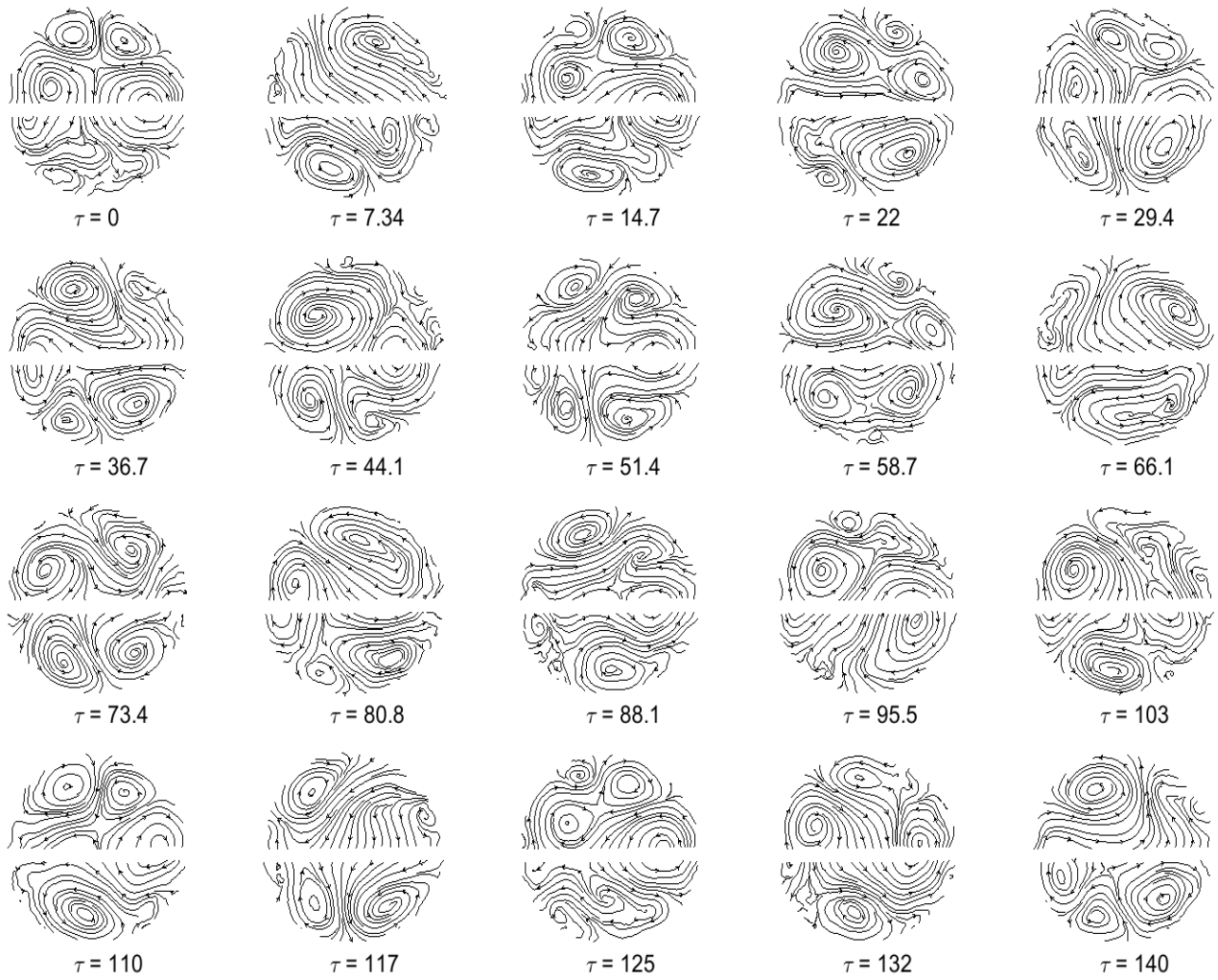

Figure 4.35 Reconstruction of fluctuations with first six modes on cross section plane 0.25D upstream at 7.2Hz.

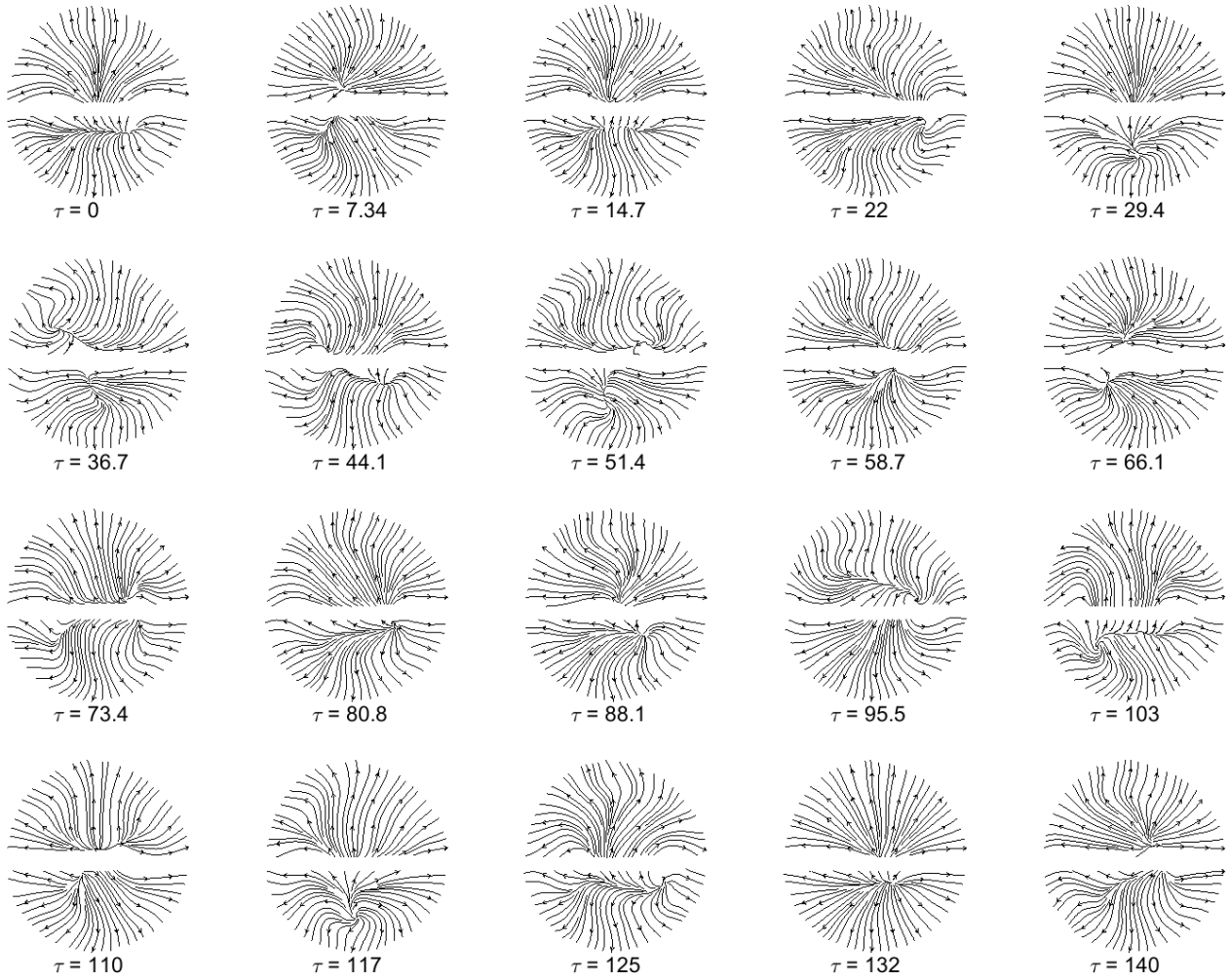

Figure 4.36 Reconstruction of total velocity with first six modes on cross section plane 1D upstream at 7.2Hz.

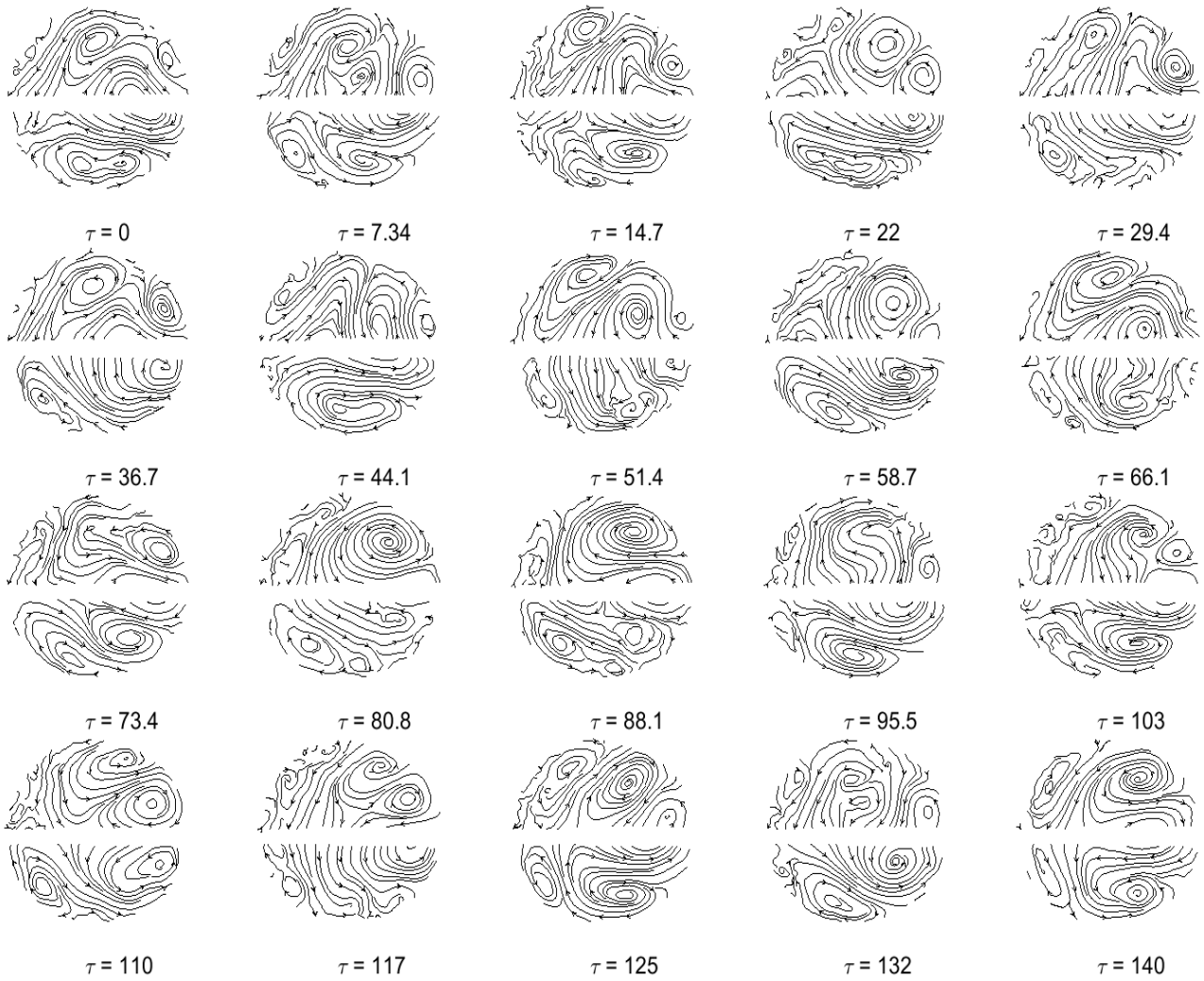

Figure 4.37 Reconstruction of fluctuations with first six modes on cross section plane 10° at 7.2Hz.

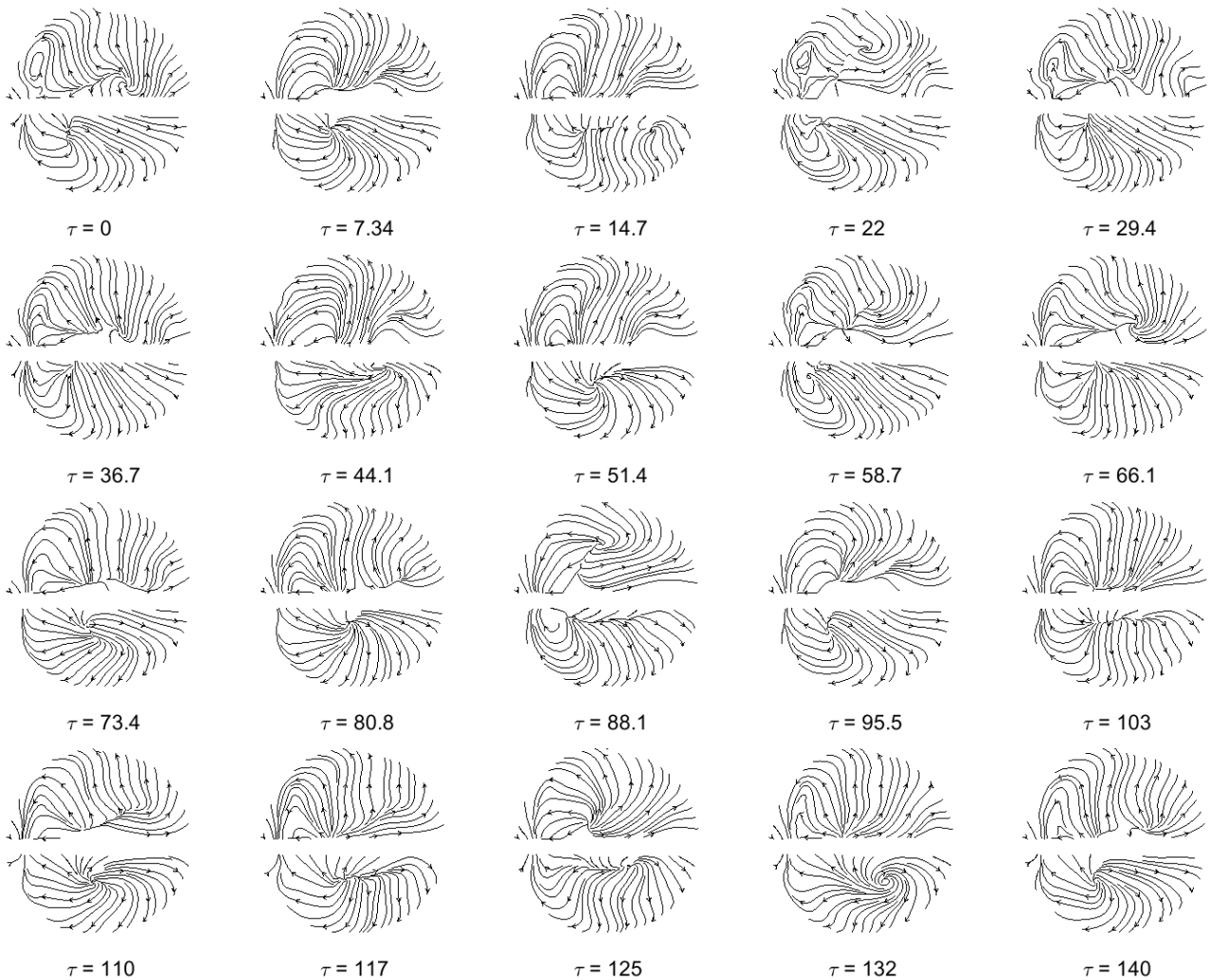

Figure 4.38 Reconstruction of total velocity with first six modes on cross section plane 10° at 7.2Hz.

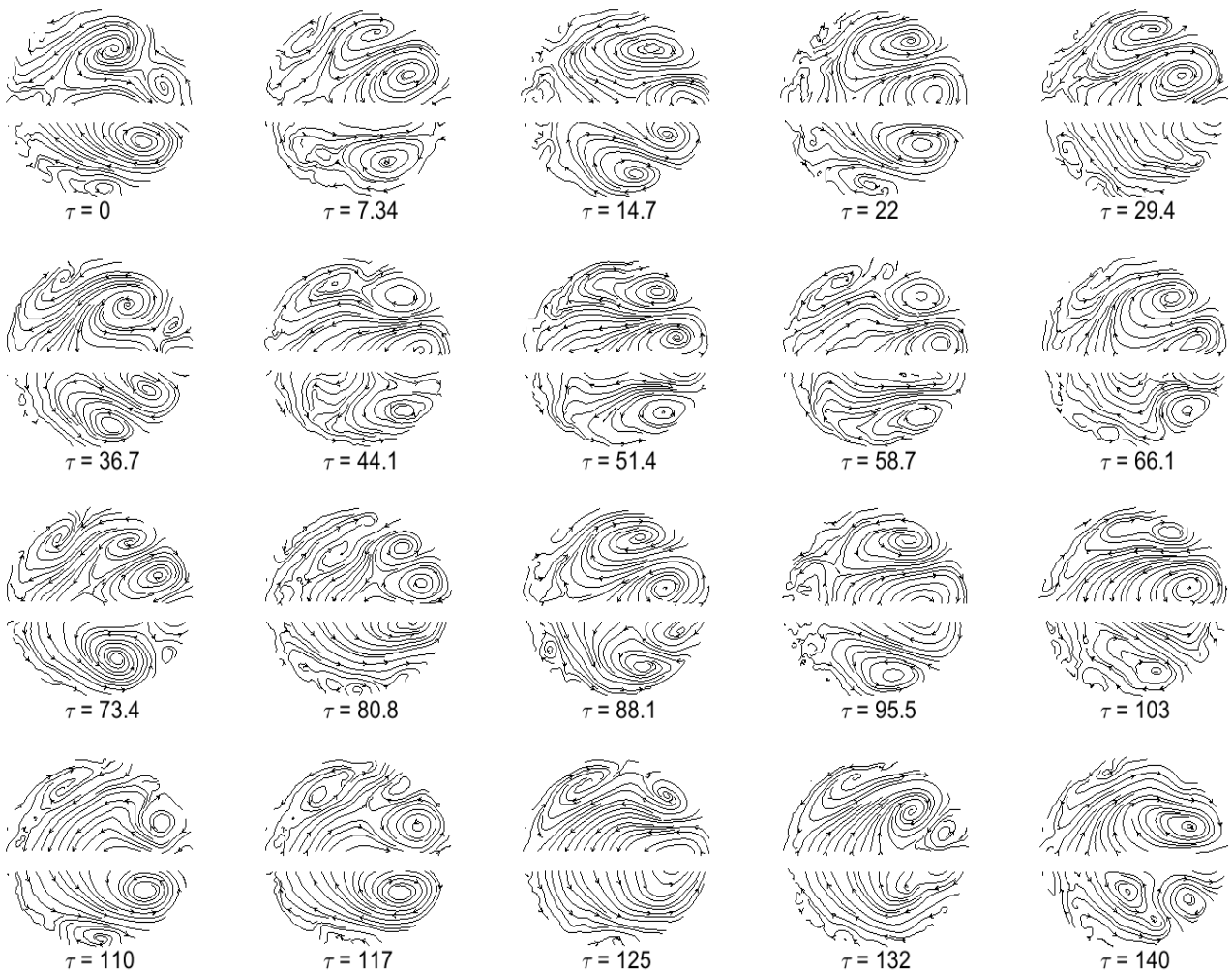

Figure 4.39 Reconstruction of fluctuations with first six modes on cross section plane 20° at 7.2Hz

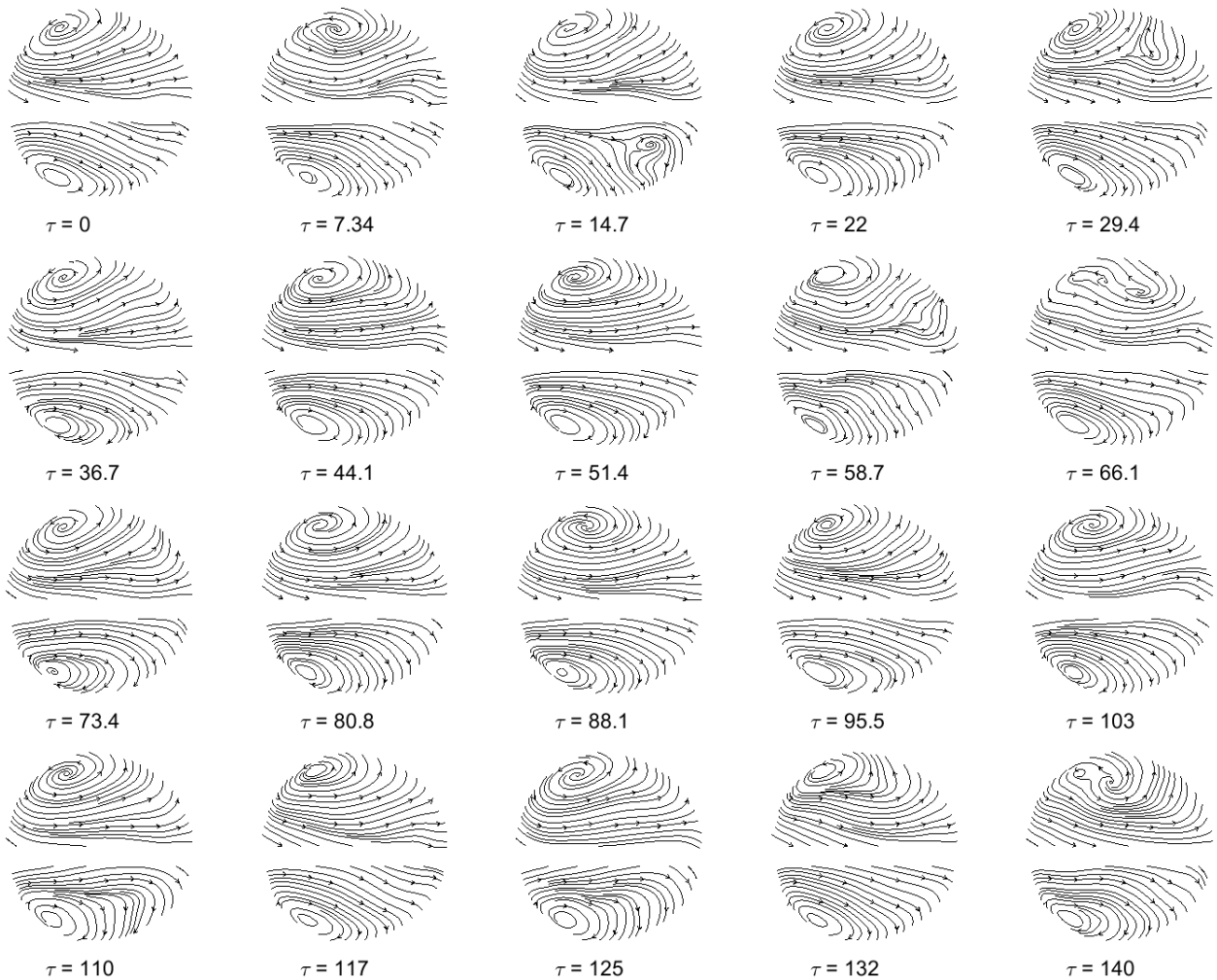

Figure 4.40 Reconstruction of total velocity with first six modes on cross section plane 20° at 7.2Hz

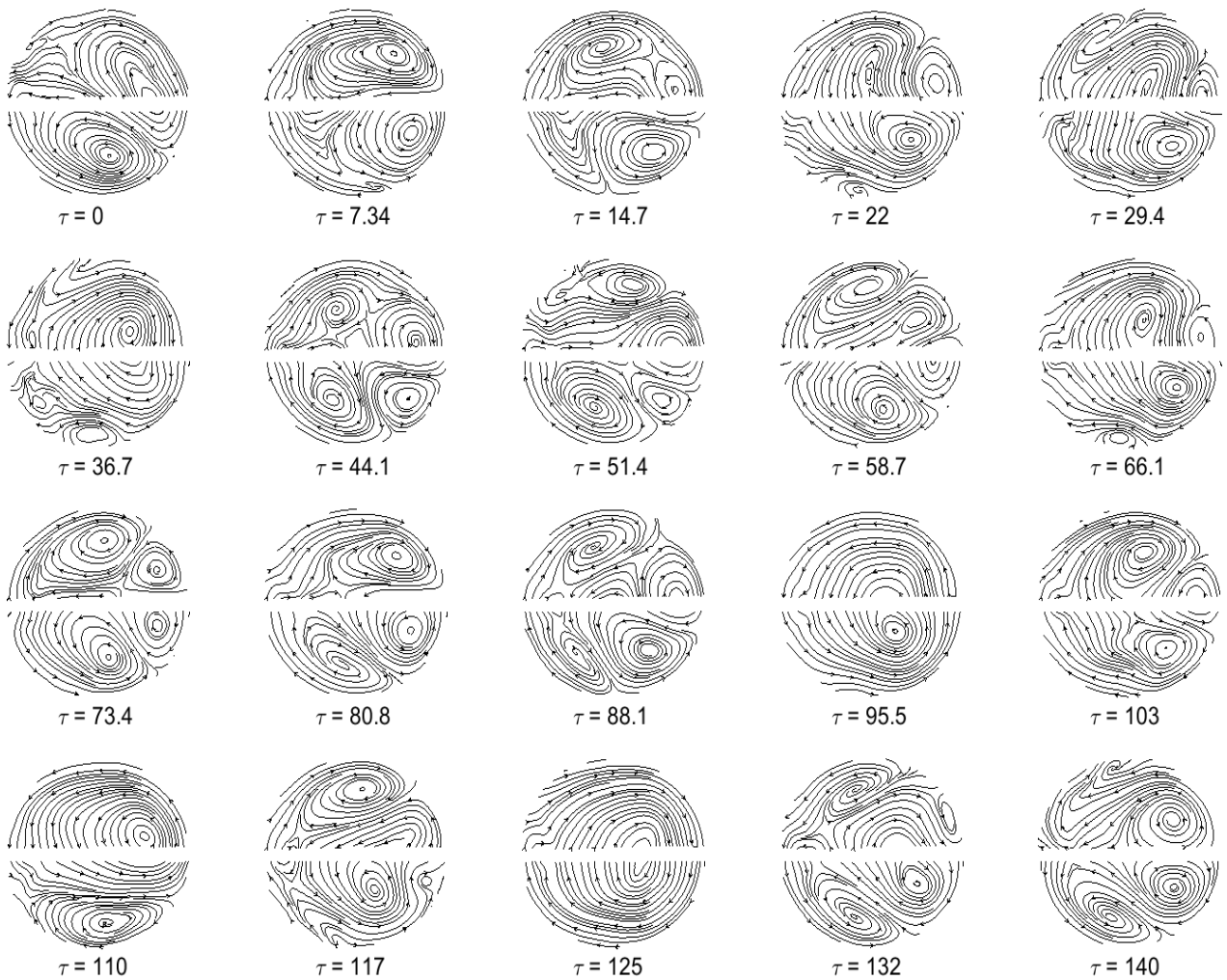

Figure 4.41 Reconstruction of fluctuations with first six modes on cross section plane 70° at 7.2Hz.

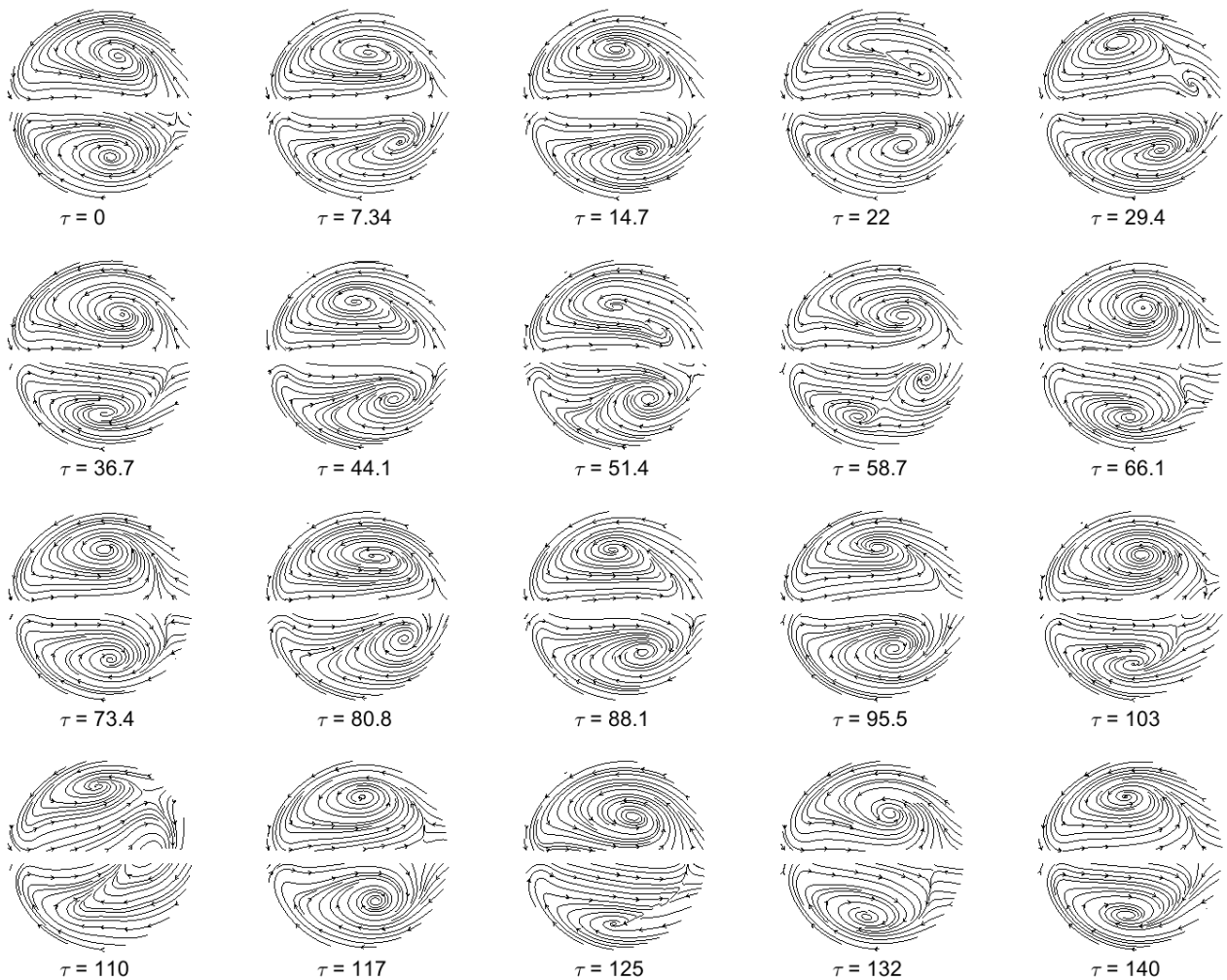

Figure 4.42 Reconstruction of total velocity with first six modes on cross section plane 70° at 7.2Hz.

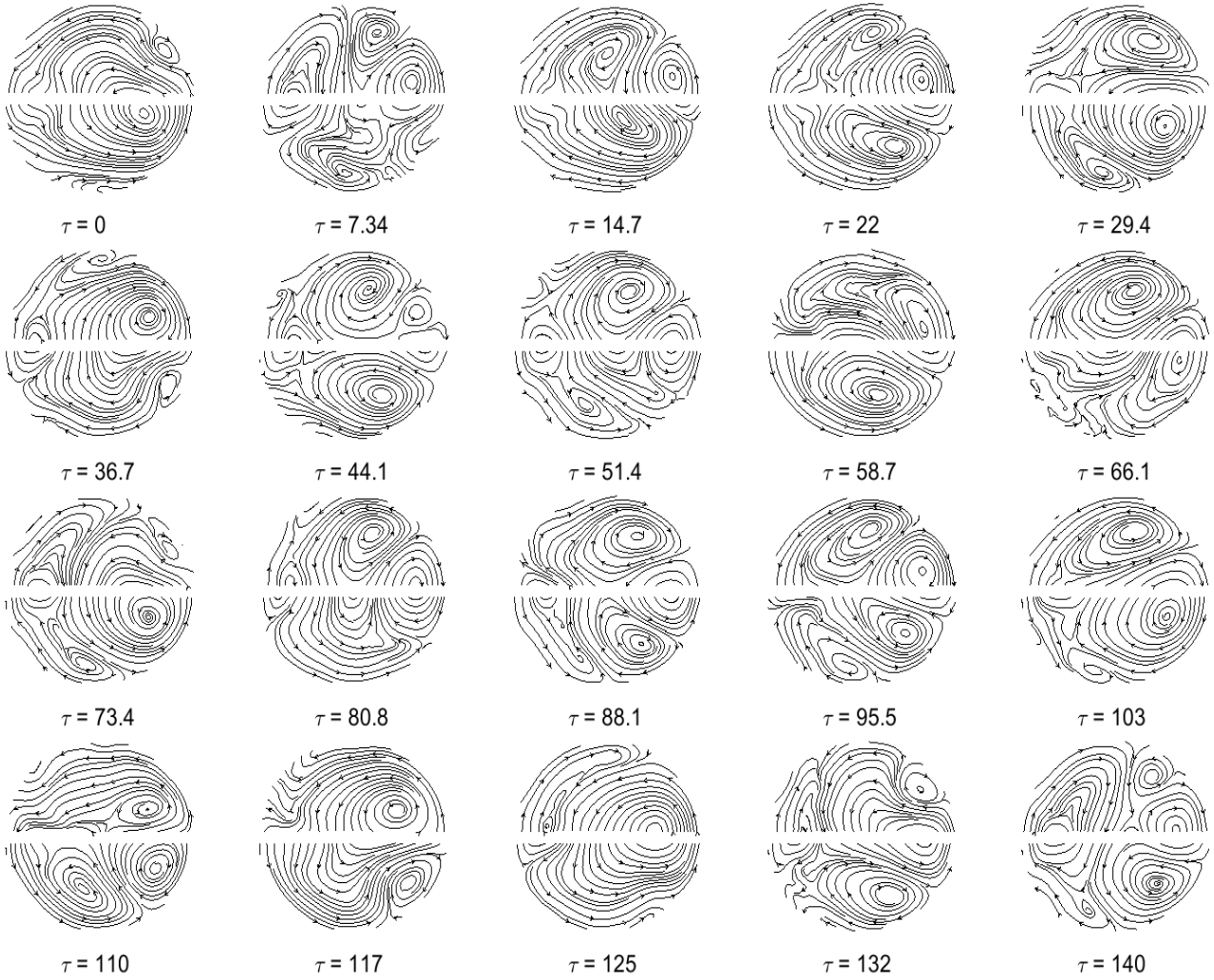

Figure 4.43 Reconstruction of fluctuations with first six modes on cross section plane 80° at 7.2Hz.

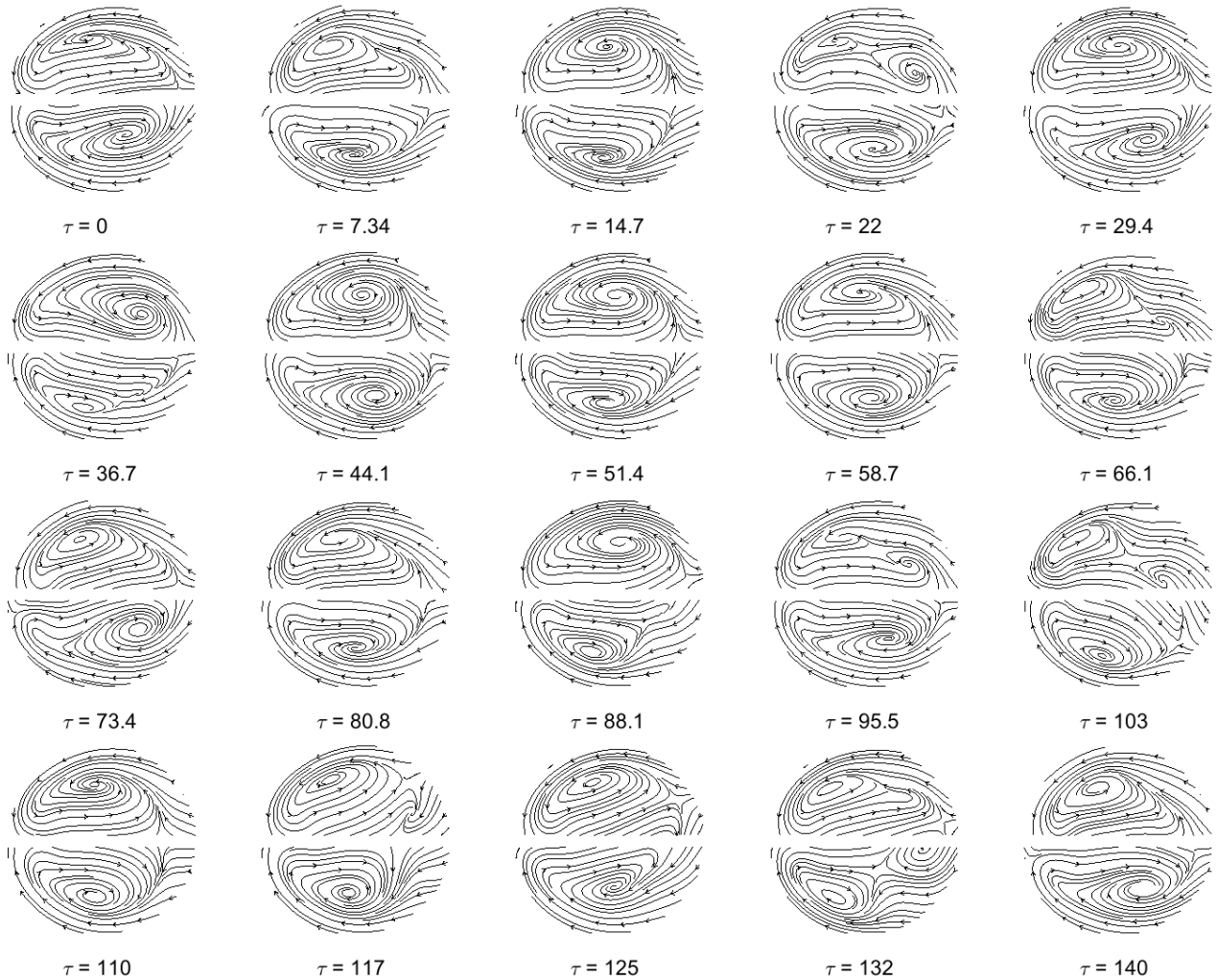

Figure 4.44 Reconstruction of total velocity with first six modes on cross section plane 80° at 7.2Hz.

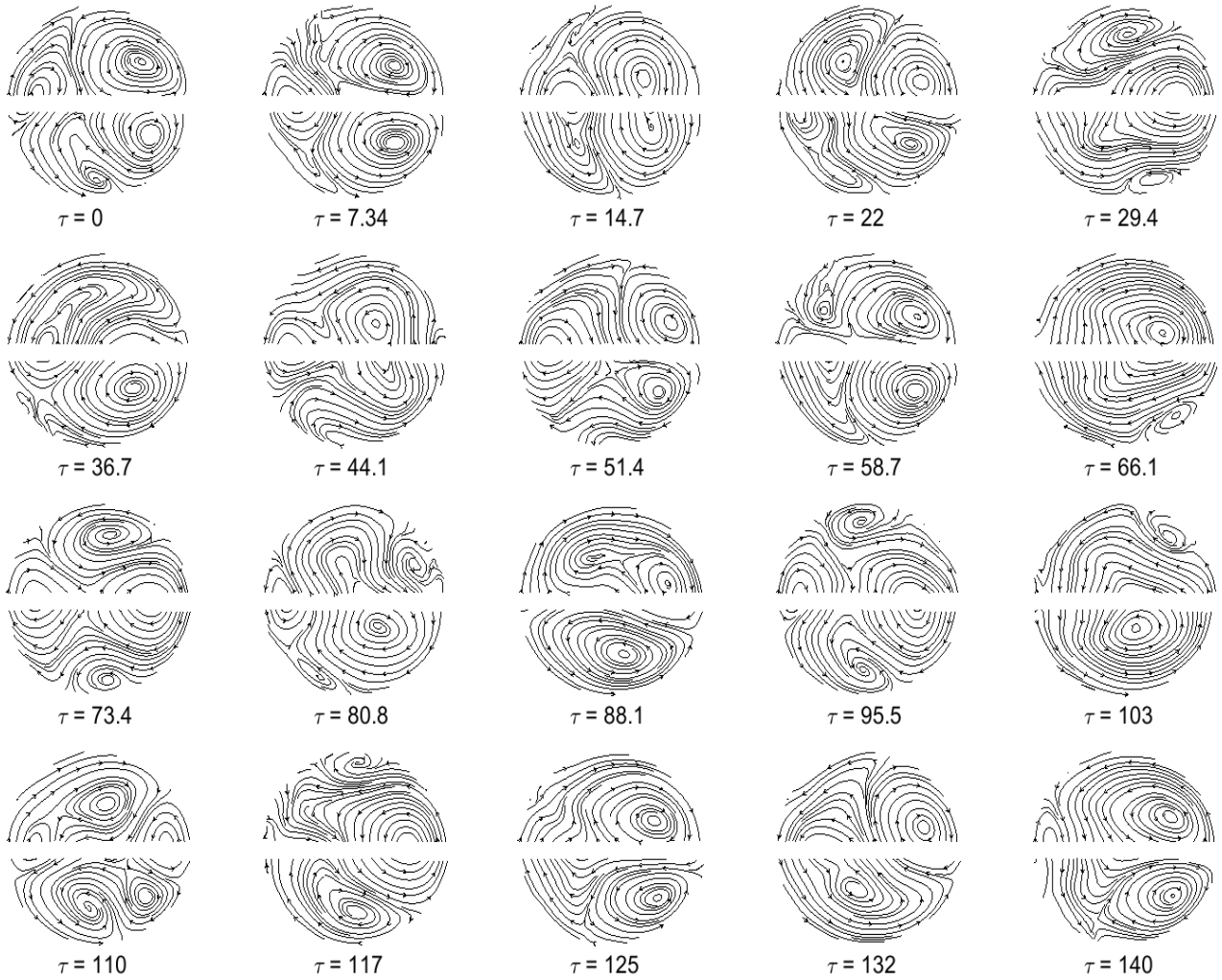

Figure 4.45 Reconstruction of fluctuations with first six modes on cross section plane 0.25D downstream at 7.2Hz

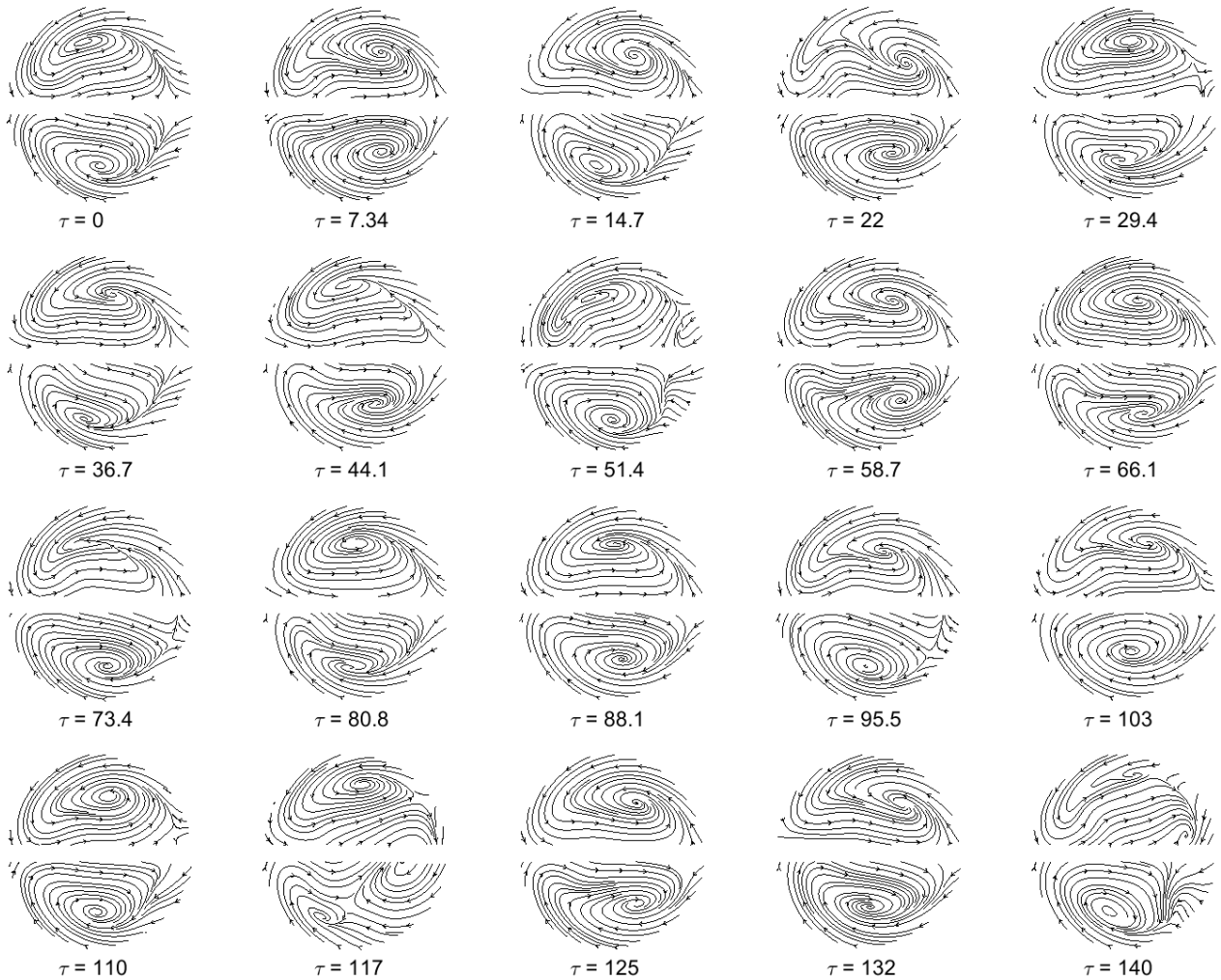

Figure 4.46 Reconstruction of total velocity with first six modes on cross section plane 0.25D downstream at 7.2Hz

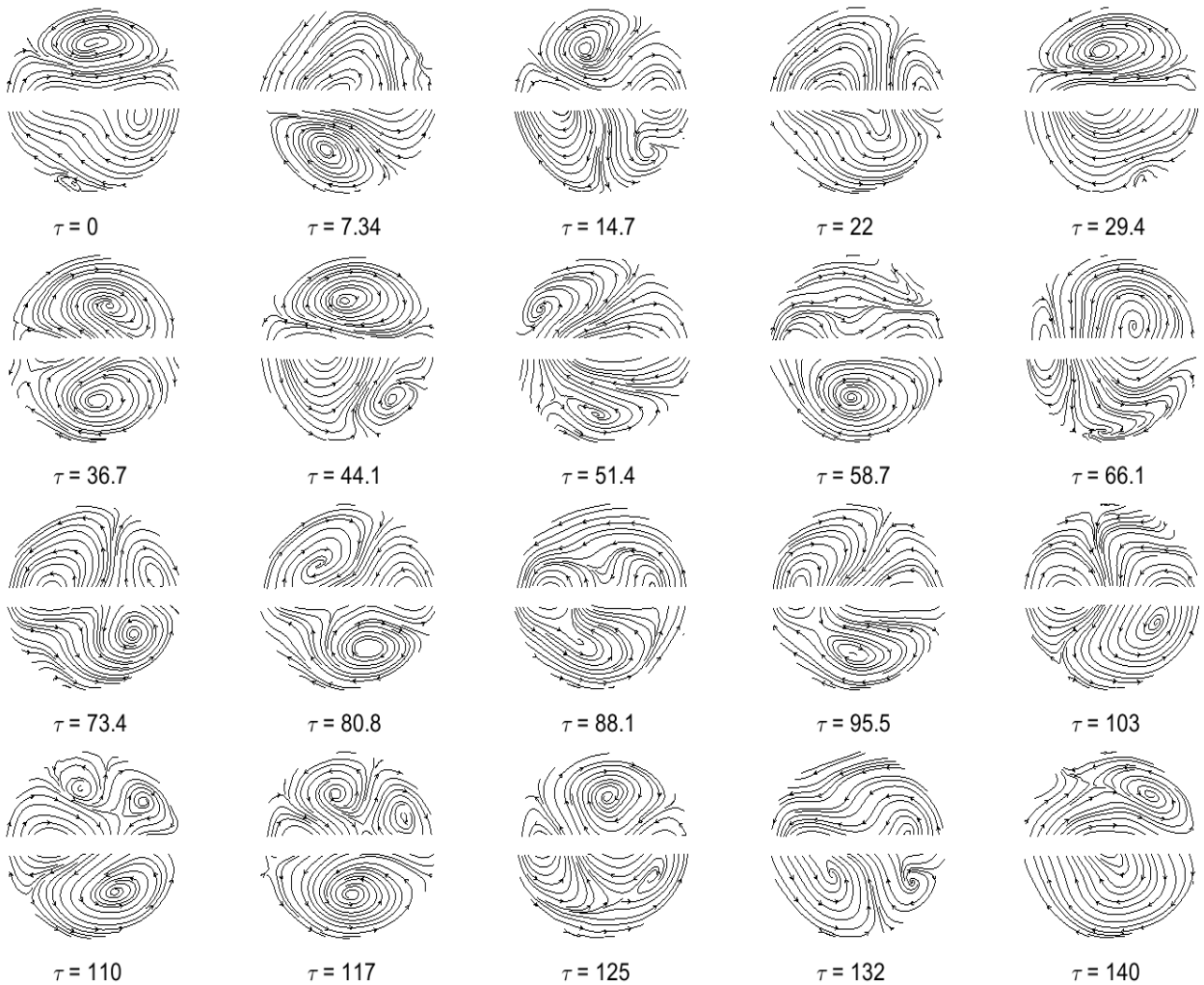

Figure 4.47 Reconstruction of fluctuations with first six modes on cross section plane 1D downstream at 7.2Hz.

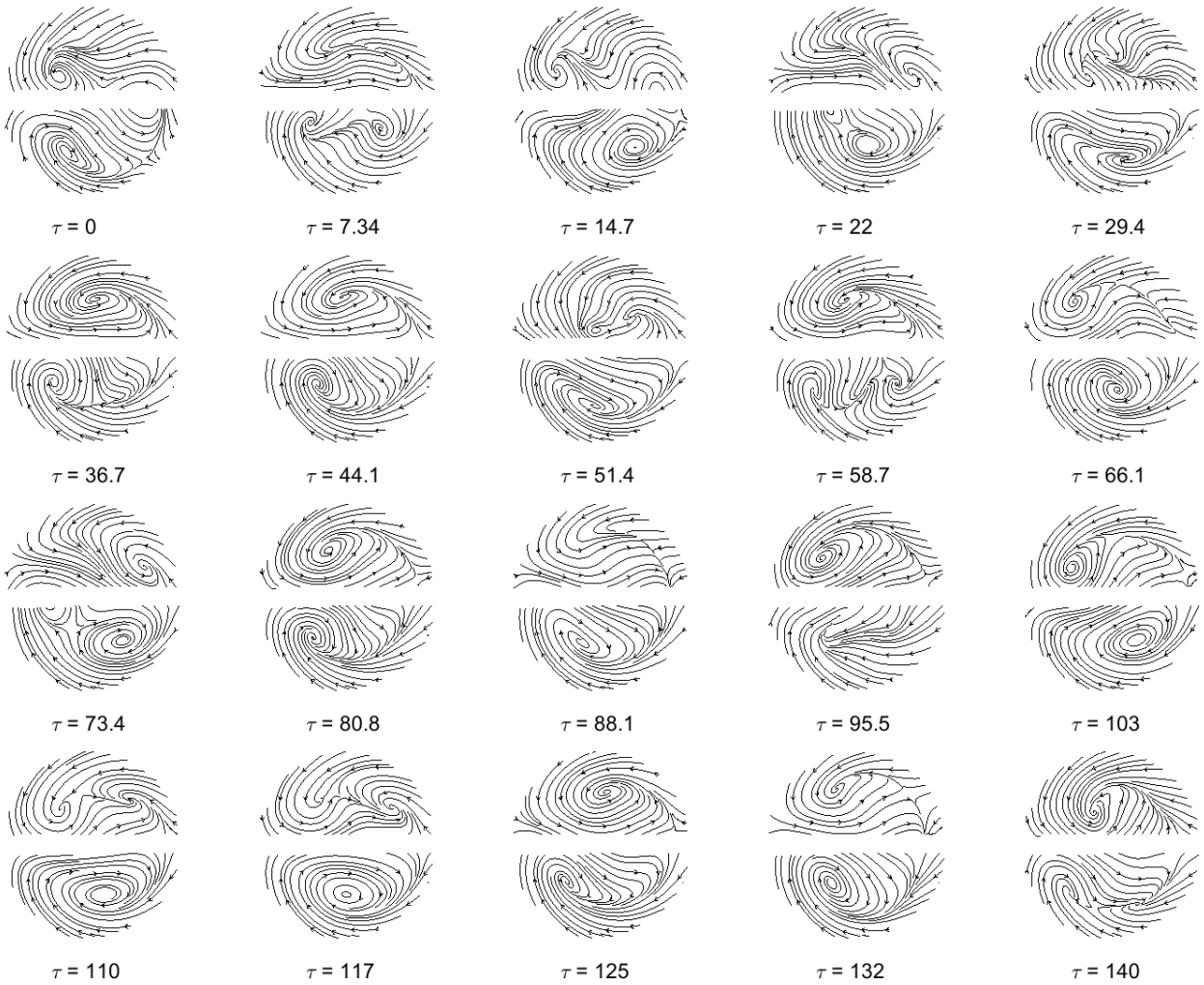

Figure 4.48 Reconstruction of total velocity with first six modes on cross section plane 1D downstream at 7.2Hz.

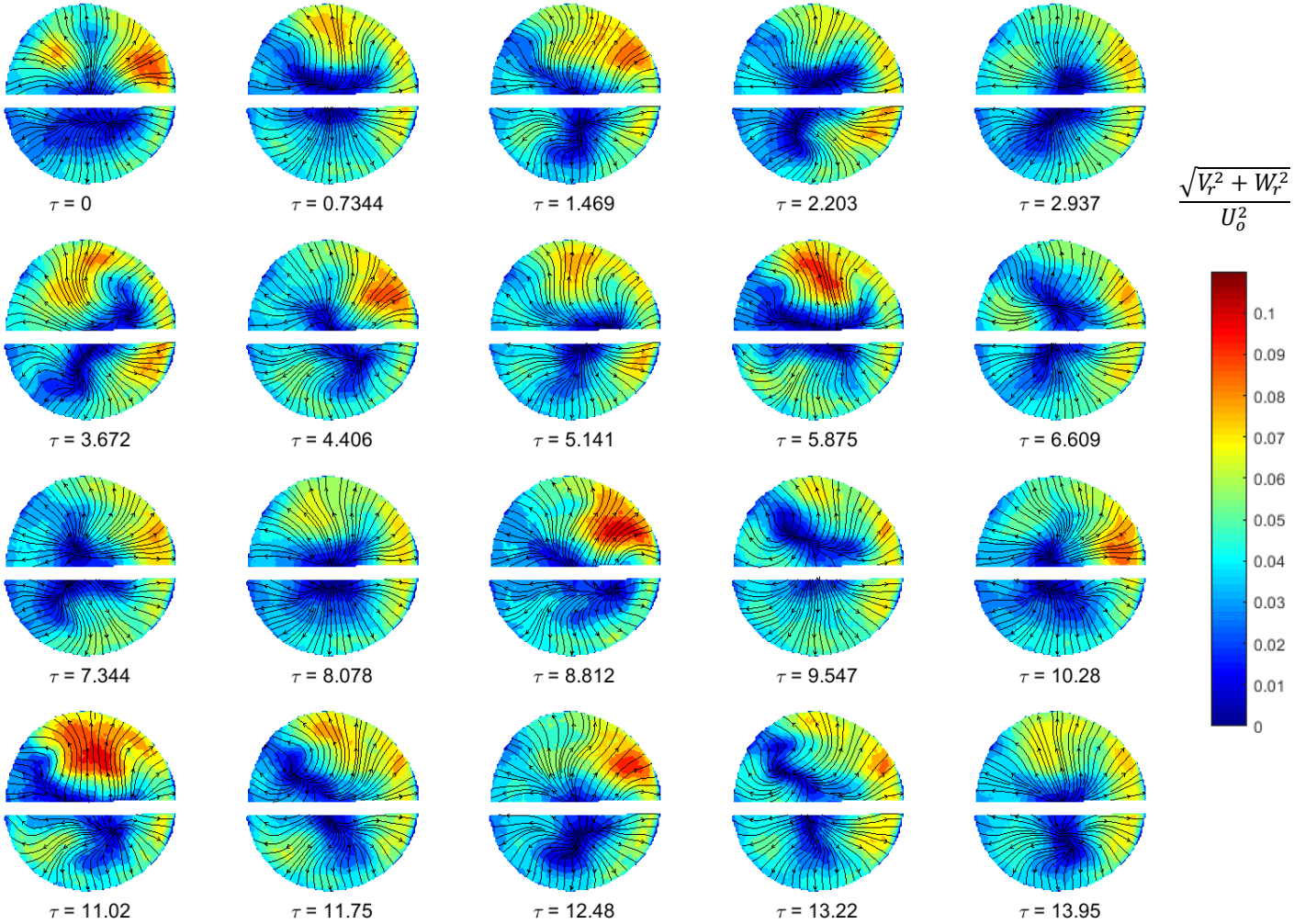

Figure 4.49 Reconstruction of total velocity with 6 modes at 0.25D upstream at 72Hz from τ= 0-13.95.

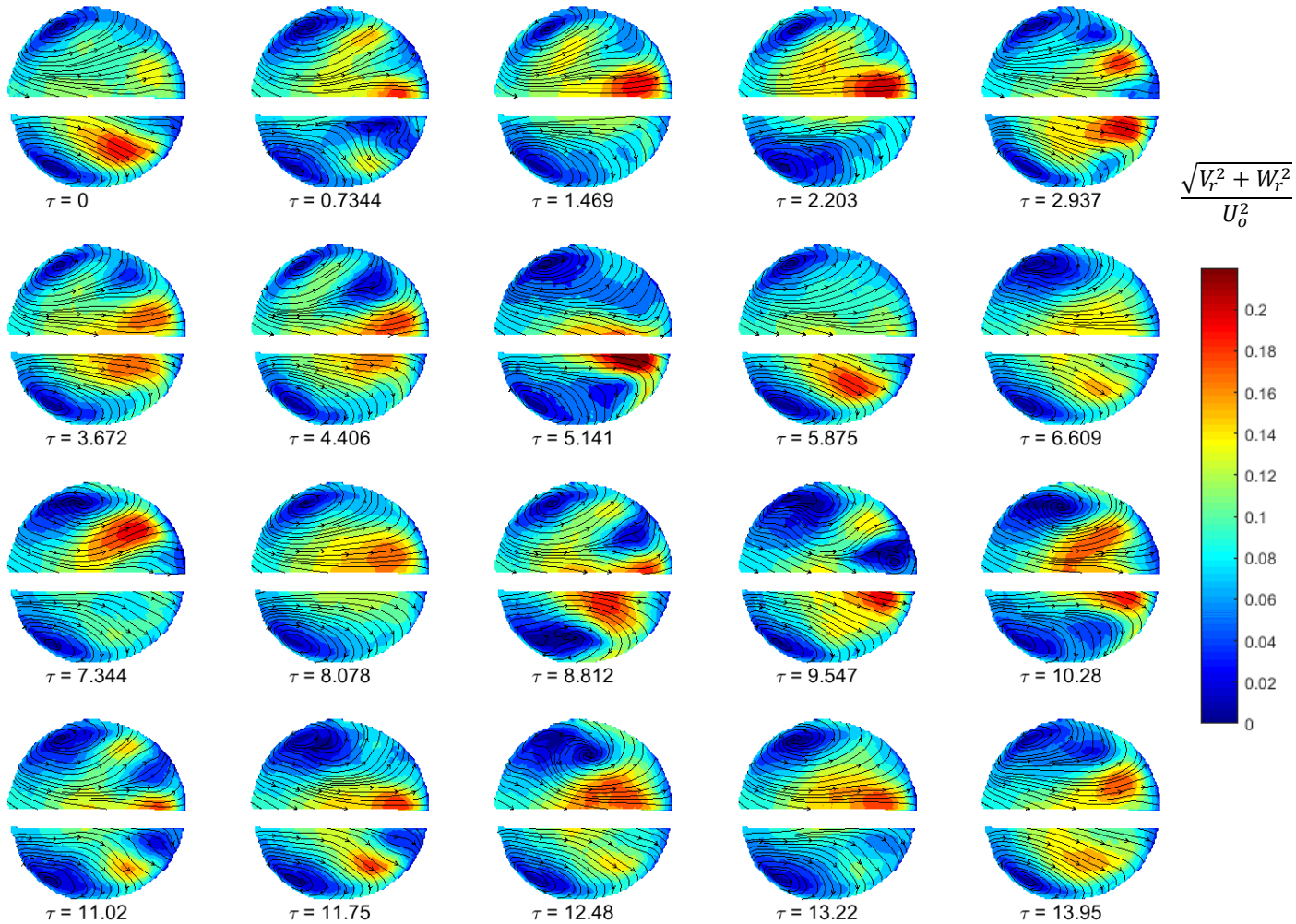

Figure 4.50 Reconstruction of total velocity with 6 modes at 20° at 72Hz from τ= 0-13.95.

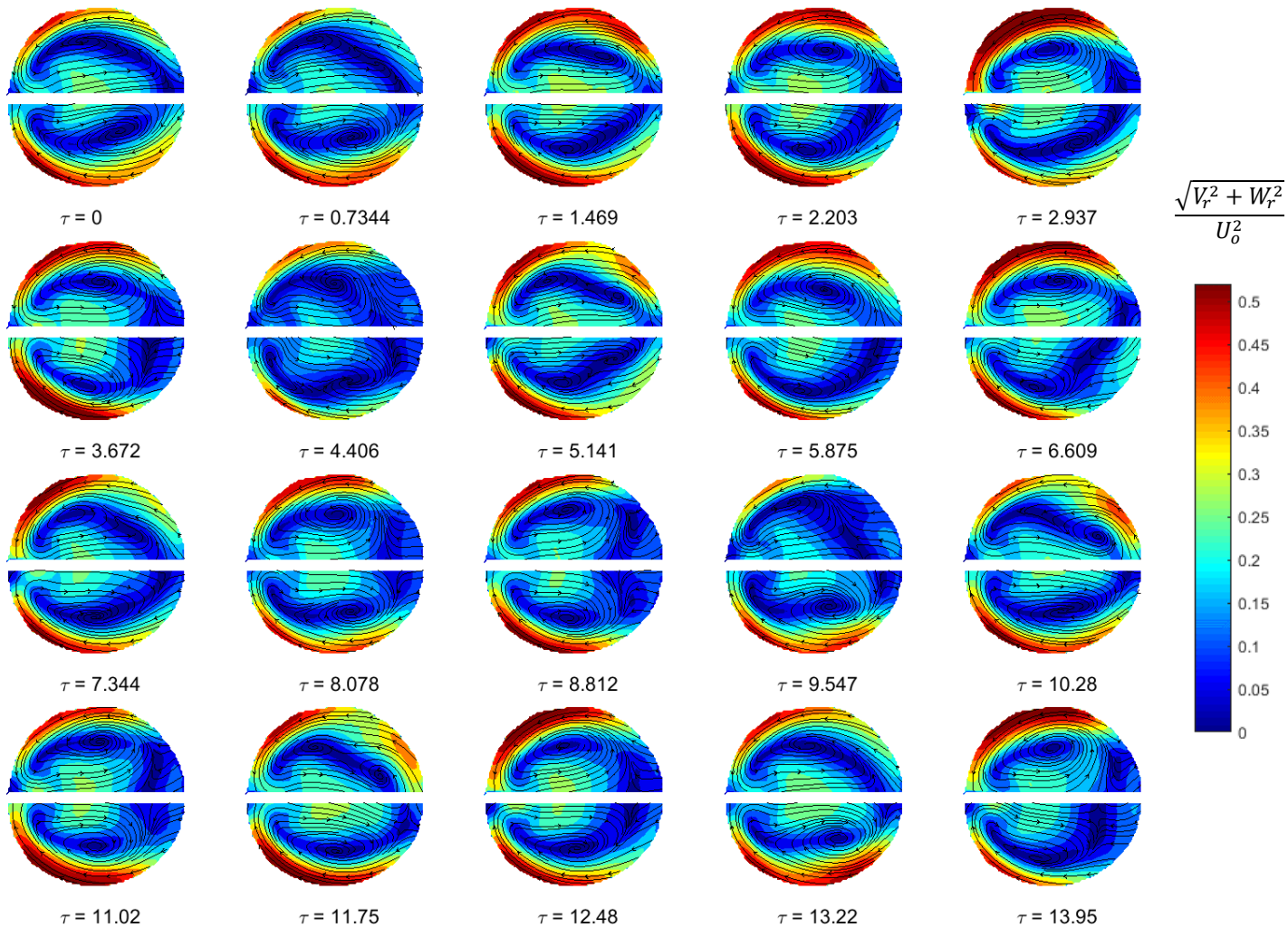

Figure 4.51 Reconstruction of total velocity with 6 modes at 80° with 72Hz from τ= 0-13.95.

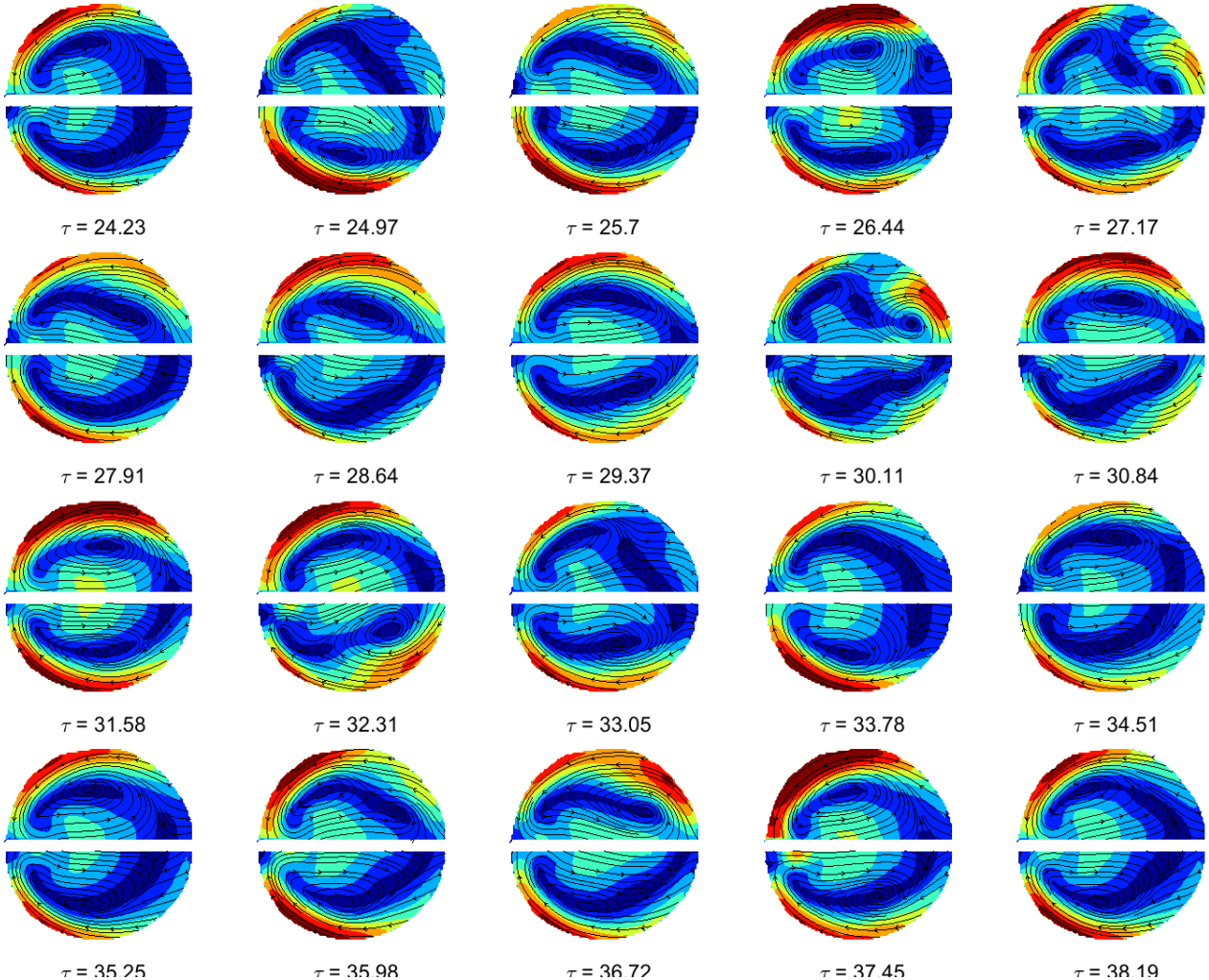

Figure 4.52 Reconstruction of total velocity with 6 modes at 80° with 72Hz from τ= 24.23-38.19.

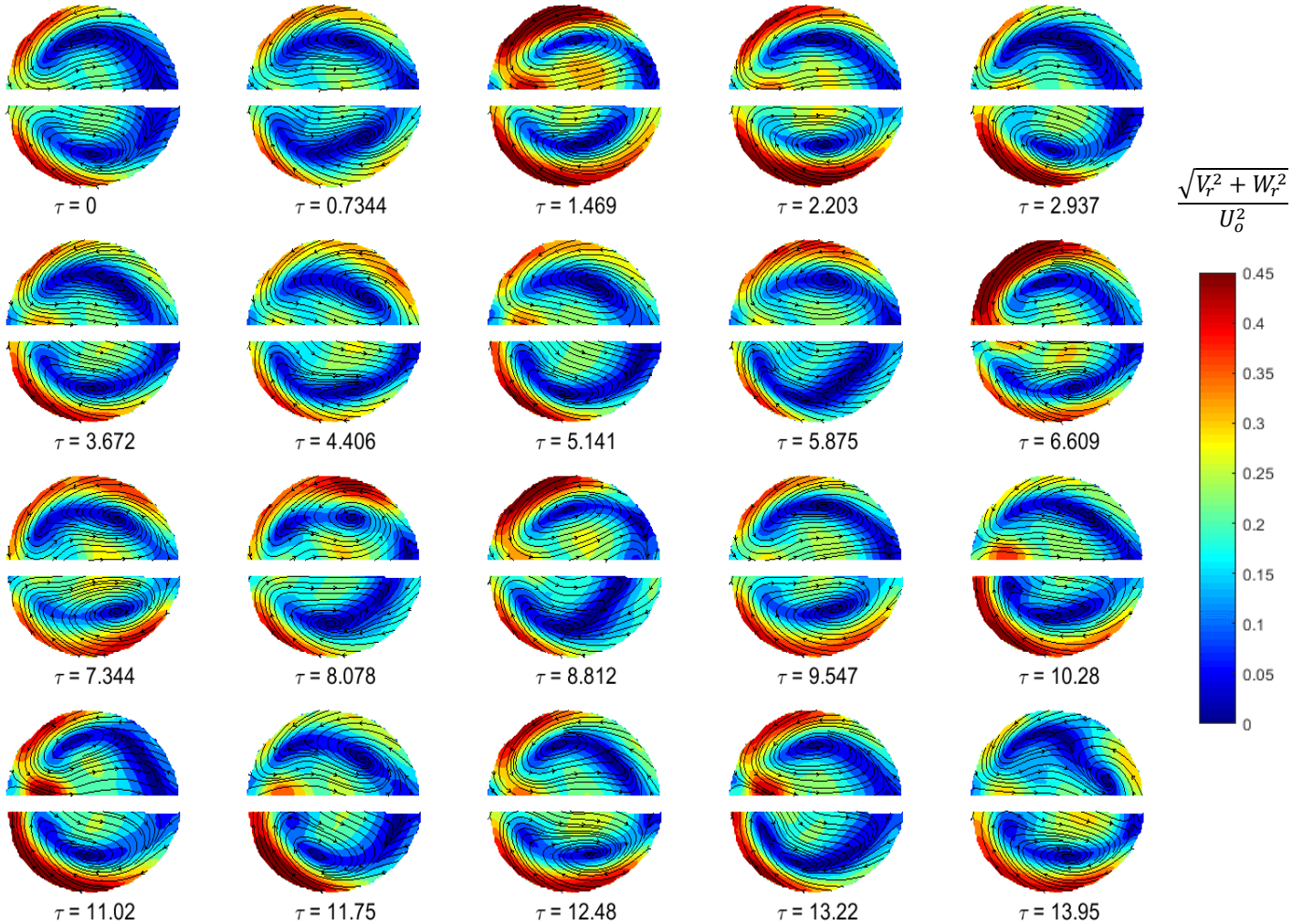

Figure 4.53 Reconstruction of total velocity with 6 modes at 0.25D downstream with 72Hz from τ= 0-13.95.

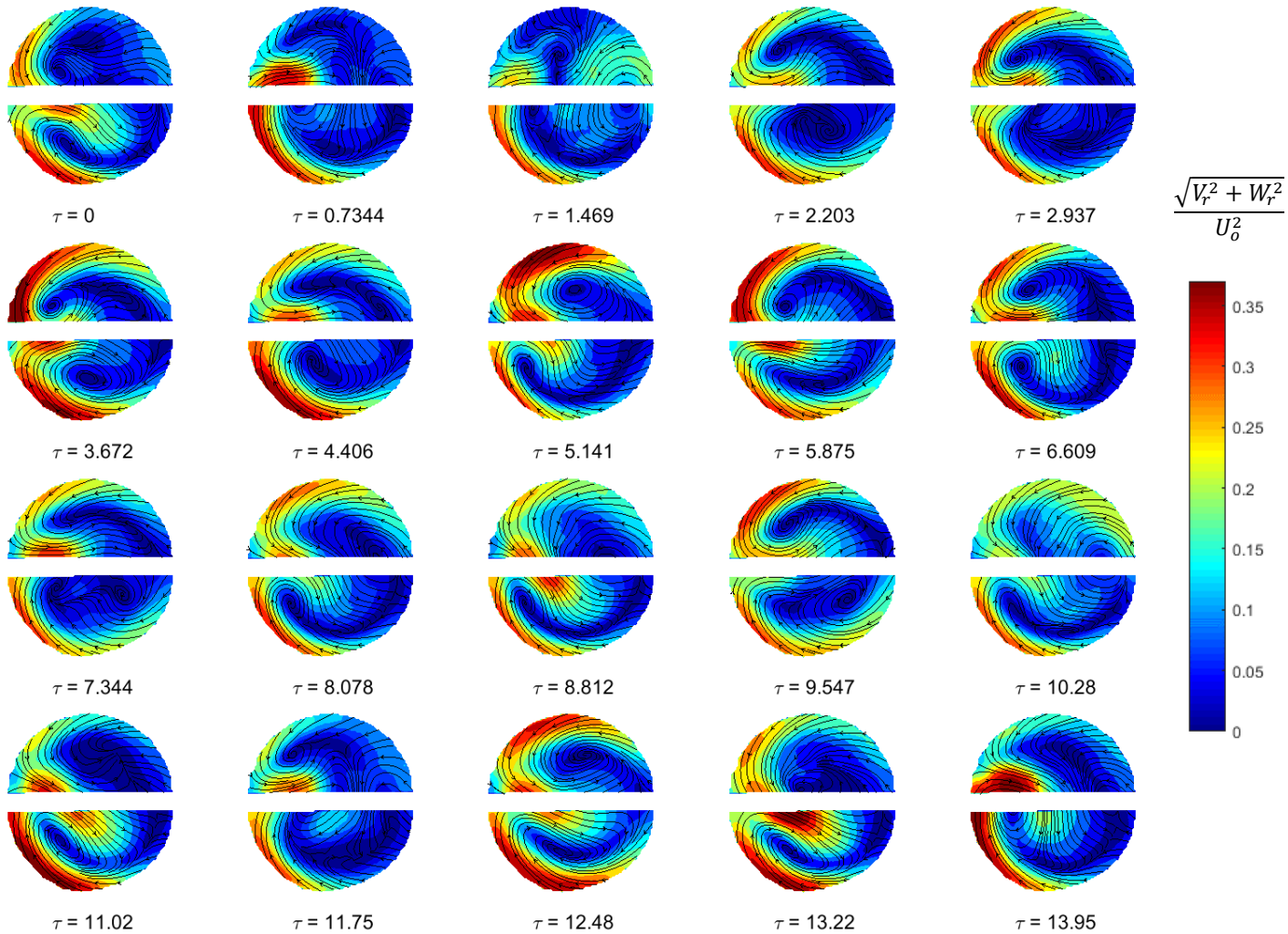

Figure 4.54 Reconstruction of total velocity with 6 modes at 1D downstream with 72Hz from τ= 0-13.95.

Chapter 5. Conclusions and Recommendations

5.1. Conclusions

The turbulent flow in a pipe bend with Rc/D = 1.5 is characterized using Particle Image Velocimetry at Re = 34800. The test section is fabricated from acrylic and the measurements were performed in a closed flow loop using a 64.2 percentage by weight solution of Sodium Iodide to refractive index match the working fluid to the test section. Measurements were performed in the axial plane of the test section that consisted of a 2D long upstream pipe, the bend and 2D long downstream pipe. Measurements were also performed on the cross sectional planes at 1D, 0.25D upstream, 10°, 20°, 70°, 80° from the bend inlet and 0.25D, 1D downstream of the bend.

A continuous laser with maximum power of 2.2W and a high speed camera with 3600 FPS at 1024 x 1024 pixel^2 is used to capture the flow. The mean flow quantities are calculated using 500 realizations while 5000 realizations are used for studying the unsteadiness in the flow. Proper Orthogonal Decomposition and spectral analysis are used to characterize the unsteady flow structures upstream, downstream and within the bend.

The mean flow 1D upstream from the bend is found to be not affected by the bend. There is a deceleration of the axial flow on the outer wall side at approximately 0.25D upstream of the bend. The axial flow has a higher velocity on the inner wall at the inlet which shifts towards the outer wall at ϕ~40-50° and remains on the outer wall side in the downstream pipe. Three regions of high turbulence in the symmetry plane are identified: (i) on the outer wall at the inlet to the bend (ii) on the inner wall at ϕ~50° extending to the downstream pipe and (iii) in the shear layer formed on the inner wall side at ϕ~50°. In the cross sectional planes, the flow is found to develop two counter rotating vortices with the highest secondary velocity reaching values of approximately 0.8 times the bulk velocity at ϕ~80° on the side walls at $\theta \sim \pm 45^o$. The cross sectional

turbulence increases on the outer wall side in the first half of the bend and then have higher values at the inner wall side in the second half of the bend.

The flow is found to be unsteady on all the cross sectional measurement planes. Large flow structures represented by the POD mode structures are found to evolve along the bend. The characteristics of the unsteady large flow structures can be summarized as:

(i) The POD mode structures in the cross sectional planes 1D and 0.25D upstream of the bend consists of multiple vortex structures that extend from the wall to the center of the pipe. The spectra of the POD mode coefficients in these cross sectional planes and in the axial cross section of the upstream pipe shows evidence of low frequency VLSM at St ~ 0.07 - 0.1 and high frequency LSM at St ~ 0.8. Additionally, in the axial cross section of the upstream pipe, a low frequency of St ~ 0.01 is present. The St ~ 0.01 is found to be related to the intermittency of VLSM while the higher frequency of St ~ 0.07-0.1 to the periodicity of VLSM. The effect of VLSM and LSM on the reconstructed total velocity from the first six modes is reflected as a movement of the flow around the pipe center.

(ii) At 10° and 20° cross sectional planes from the bend inlet, the POD mode structures of secondary flow fluctuations differ from that in the upstream pipe. The spectra shows a distinct frequency at St ~ 0.07 suggesting VLSM imparting low frequency oscillations to the secondary flow. The reconstructed total velocity are found to have small oscillations.

(iii) A single dominant vortex and two vortices tilted from the bend symmetry plane are found as the first two energetic modes of the flow fluctuations in the cross sectional planes at 70° and 80° from the bend inlet. These structures impart unsteady oscillations to the total secondary flow which are found to have a wide range of frequencies. Low frequencies of St ~ 0.07, 0.13 are related to two vortices in the total flow oscillating about the symmetry plane while a characteristic frequency of St ~ 0.3-0.6 is found to be related to the flow separation on the inner wall.

(iv) In the 0.25D downstream cross sectional plane, the 1st mode is a single swirl while the 2nd and 3rd modes are two vortices tilted from the symmetry plane of the bend. The unsteadiness in the 0.25D downstream plane shows low frequency oscillations of the two vortices about the symmetry plane with higher amplitudes. The high frequency events are identified as change in high velocity region on the side walls.

(v) At the 1D downstream plane, the mode shapes are similar to that in 0.25D downstream plane. The reconstructed total velocity shows the strength and size of the two vortices change alternatively with a frequency in the higher range of St ~ 0.3-0.5.

The presence of unsteady flow structures with St ~ 0.07 and 0.13 can be related to VLSM in the upstream pipe. The VLSM tend to impart oscillations to the two vortices in the secondary flow. These oscillations are found in all the cross sectional planes along the bend with low frequency of St ~ 0.07 and 0.13. The higher frequency (St ~ 0.5) structures are not present in first half of the bend and are present in the cross sectional planes downstream of the separation point. These are identified as change in high velocity region on the inner wall side up to 0.25D downstream. On the 1D downstream plane, the swirl switching is seen as high velocity sweeps at the inner wall that alternates resulting in the alternate domination of one vortex of the two vortices with higher frequency of St ~ 0.3-0.5.

5.2. Recommendations

1. The present measurements are in a 2-dimensional plane and results in 2 components of velocity in the plane. The flow field in the pipe bend, however, is three dimensional. Experiments capturing all three components of velocity in any plane would provide a more complete picture of the secondary flow structures within the bend.
2. The current experiments are restricted to planes that are 20° from the inlet and outlet of the bend. Test section measurement technique modification to capture flow throughout the bend would be very useful.
3. The pressure drop and heat/mass transfer is different if a second bend is present in any configuration. The effect of a second bend on the unsteady motions would be useful to study the effect of the flow on the pressure drop and mass transfer in back to back bends.

List of References

Achenbach, Elmar. 1976. "Mass Transfer from Bends of Circular Cross Section to Air." *Future Energy Production System* 1: 327–37.

Ahmed, Wael H. 2010. "Evaluation of the Proximity Effect on Flow-Accelerated Corrosion." *Annals of Nuclear Energy* 37 (4): 598–605. doi:10.1016/j.anucene.2009.12.020.

Al-Rafai, W. N., Y. D. Tridimas, and N. H. Woolley. 1990. "A Study of Turbulent Flows in Pipe Bends." *Proceedings of the Institution of Mechanical Engineers, Part C: Journal of Mechanical Engineering Science* 204 (6). SAGE PublicationsSage UK: London, England: 399–408. doi:10.1243/PIME_PROC_1990_204_120_02.

Anwer, M., R. M. C. So, and Y. G. Lai. 1989. "Perturbation by and Recovery from Bend Curvature of a Fully Developed Turbulent Pipe Flow." *Physics of Fluids A: Fluid Dynamics* 1 (1989): 1387. doi:10.1063/1.857315.

Azzola, J, J a C Humphrey, H Iacovides, and B E Launder. 1986. "Developing Turbulent Flow in a U-Bend of Circular Cross-Section: Measurement and Computation." *Transactions of the ASME. Journal of Fluids Engineering* 108: 214–21.

Bai, Kunlun, and Joseph Katz. 2014. "On the Refractive Index of Sodium Iodide Solutions for Index Matching in PIV." *Experiments in Fluids* 55 (4): 1704. doi:10.1007/s00348-014-1704-x.

Beij, K.H. 1938. "Pressure Losses for Fluid Flow in 90 Degree Pipe Bends." *Journal of Research of the National Bureau of Standards* 21 (1): 1. doi:10.6028/jres.021.001.

Benedict, L. H., and R. D. Gould. 1996. "Towards Better Uncertainty Estimates for Turbulence Statistics." *Experiments in Fluids* 22 (2). Springer-Verlag: 129–36. doi:10.1007/s003480050030.

Bergstrom, Donald J., Trevor Bender, George Adamopoulos, and John Postlethwaite. 1998. "Numerical Prediction of Wall Mass Transfer Rates in Turbulent Flow through a 90° Two-Dimensional Bend." *The Canadian Journal of Chemical Engineering* 76 (4). Wiley Subscription Services, Inc., A Wiley Company: 728–37. doi:10.1002/cjce.5450760407.

Brücker, Ch. 1998. "A Time-Recording Dpiv-Study of the Swirl Switching Effect in a 90° Bend Flow." *Proc. 8th International Symposium on Flow Visualization, Sorrento(NA), Italy*, 171.1-171.6.

Carlsson, C., E. Alenius, and L. Fuchs. 2015. "Swirl Switching in Turbulent Flow through 90° Pipe Bends." *Physics of Fluids* 27 (8): 85112. doi:10.1063/1.4928971.

Chen, Hao, David L Reuss, and Volker Sick. 2012. "On the Use and Interpretation of Proper Orthogonal Decomposition of in-Cylinder Engine Flows." *Measurement Science and Technology* 23 (8): 85302. doi:10.1088/0957-0233/23/8/085302.

Chrysler, G M, and E M Sparrow. 1986. "Turbulent Flow and Heat Transfer in Bends of Circular Cross Section: I-Heat Transfer Experiments." *Journal of Heat Transfer* 108 (February 1986): 212–16.

Coffield, RD, RB Hammond, and JP Koczko. 1998. "Irrecoverable Pressure Loss Coefficients for a Short Radius of Curvature Piping Elbow at High Reynolds Numbers." http://www.osti.gov/bridge/product.biblio.jsp?osti_id=650318.

Coney, M W E. 1981. *Erosion-Corrosion: The Calculation of Mass-Transfer Coefficients*. CEGB.

Crawford, N. M., G. Cunningham, and S. W. T. Spence. 2007. "An Experimental Investigation into the Pressure Drop for Turbulent Flow in 90° Elbow Bends." *Proceedings of the Institution of Mechanical Engineers, Part E: Journal of Process Mechanical Engineering* 221 (May): 77–88. doi:10.1243/0954408JPME84.

Crawford, N M, G Cunningham, and P L Spedding. 2003. "Prediction of Pressure Drop for Turbulent Fluid Flow in 90° Bends." *Proceedings of the Institution of Mechanical Engineers, Part E: Journal of Process Mechanical Engineering* 217 (3): 153–55. doi:10.1243/095440803322328827.

Dennis, David J C, and Francesca M Sogaro. 2014. "Distinct Organizational States of Fully Developed Turbulent Pipe Flow." *Physical Review Letters* 113 (23). APS: 234501.

Dutta, Prasun, and Nityananda Nandi. 2015. "Study on Pressure Drop Characteristics of Single Phase Turbulent Flow in Pipe Bend for High Reynolds Number" 10 (5):

2221–26.

Dutta, Prasun, Sumit Kumar Saha, Nityananda Nandi, and Nairit Pal. 2016. "Numerical Study on Flow Separation in 90° Pipe Bend under High Reynolds Number by K-ε Modelling." *Engineering Science and Technology, an International Journal* 19 (2): 904–10. doi:10.1016/j.jestch.2015.12.005.

Ebara, Shinji, Yuta Aoya, Tsukasa Sato, Hidetoshi Hashizume, Yuki Kazuhisa, Kosuke Aizawa, and Hidemasa Yamano. 2010. "Pressure Fluctuation Characteristics of Complex Turbulent Flow in a Single Elbow With Small Curvature Radius for a Sodium-Cooled Fast Reactor." *Journal of Fluids Engineering* 132 (11). ASME: 111102–7. http://dx.doi.org/10.1115/1.4002813.

Eguchi, Yuzuru, Takahiro Murakami, Masaaki Tanaka, and Hidemasa Yamano. 2011. "A Finite Element Les for High-Re Flow in a Short-Elbow Pipe with Undisturbed Inlet Velocity." In *Nuclear Engineering and Design*, 241:4368–78. doi:10.1016/j.nucengdes.2010.09.038.

El-Gammal, M., H. Mazhar, J.S. Cotton, C. Shefski, J. Pietralik, and C.Y. Ching. 2010. "The Hydrodynamic Effects of Single-Phase Flow on Flow Accelerated Corrosion in a 90-Degree Elbow." *Nuclear Engineering and Design* 240 (6): 1589–98. doi:10.1016/j.nucengdes.2009.12.005.

Enayet, M.M., M.M. Gibson, A.M.K.P. Taylor, and M. Yianneskis. 1982. "Laser-Doppler Measurements of Laminar and Turbulent Flow in a Pipe Bend." *International Journal of Heat and Fluid Flow* 3 (4): 213–19. doi:10.1016/0142-727X(82)90024-8.

Fiedler, H E. 1997. "A Note on Secondary Flow in Bends and Bend Combinations." *Experiments in Fluids* 23. Springer-Verlag.

Hellström, Leo H. O., Aman Sinha, and Alexander J. Smits. 2011. "Visualizing the Very-Large-Scale Motions in Turbulent Pipe Flow." *Physics of Fluids* 23 (1). American Institute of Physics: 11703. doi:10.1063/1.3533016.

Hellström, Leo H. O., Metodi B. Zlatinov, Guangjun Cao, and Alexander J. Smits. 2013. "Turbulent Pipe Flow Downstream of a 90° Bend." *Journal of Fluid Mechanics* 735:

R7-1–12. doi:10.1017/jfm.2013.534.

Hellstrom, Leo H O, Metodi B Zlatinov, Alexander J Smits, and Guongjun Cao. 2011. "Turbulent Pipe Flow through a 90 Bend." In *TSFP DIGITAL LIBRARY ONLINE*. Begel House Inc.

Ikarashi, Yuya, Shoichi Taguchi, Takayuki Yamagata, and Nobuyuki Fujisawa. 2017. "Mass and Momentum Transfer Characteristics in and Downstream of 90° Elbow." *International Journal of Heat and Mass Transfer* 107: 1085–93. doi:10.1016/j.ijheatmasstransfer.2016.11.014.

Itō, H. 1960. "Pressure Losses in Smooth Pipe Bends." *Journal of Basic Engineering* 82 (1): 131–40. doi:10.1115/1.3662501.

Kalpakli, A. 2012. "Experimental Study of Turbulent Flows through Pipe Bends Athanasia Kalpakli," no. April. Engineering Sciences, Royal Institute of Technology (KTH): 1–78.

Kalpakli, A., and R. Örlü. 2013. ""Turbulent Pipe Flow Downstream a 90° Pipe Bend with and without Superimposed Swirl." *International Journal of Heat and Fluid Flow* 41 (2013). Elsevier Inc.: 103–11. doi:10.1016/j.ijheatfluidflow.2013.01.003.

Kalpakli Vester, Athanasia, Ramis Örlü, and P Henrik Alfredsson. 2016. "Turbulent Flows in Curved Pipes: Recent Advances in Experiments and Simulations." *Applied Mechanics Reviews* 68 (5). ASME: 50802–25. http://dx.doi.org/10.1115/1.4034135.

Kalpakli Vester, Athanasia, Ramis, and P. Henrik Alfredsson. 2015. "POD Analysis of the Turbulent Flow Downstream a Mild and Sharp Bend." *Experiments in Fluids* 56 (3). doi:10.1007/s00348-015-1926-6.

Keane, Richard D, and Ronald J Adrian. 1992. "Theory of Cross-Correlation Analysis of PIV Images." *Applied Scientific Research* 49 (3): 191–215. doi:10.1007/BF00384623.

Kim, Jongtae, Mohan Yadav, and Seungjin Kim. 2014. "Characteristics of Secondary Flow Induced by 90-Degree Elbow in Turbulent Pipe Flow." *Engineering Applications of Computational Fluid Mechanics* 8 (2): 229–39. doi:10.1080/19942060.2014.11015509.

Kim, K. C., and R. J. Adrian. 1999. "Very Large-Scale Motion in the Outer Layer." *Physics of Fluids* 11 (2). American Institute of Physics: 417–22. doi:10.1063/1.869889.

Lazar, Eli, Bradley Deblauw, Nick Glumac, Craig Dutton, Gregory Elliott, and Associate Head. 2010. "A Practical Approach to PIV Uncertainty Analysis." *27th AIAA Aerodynamic Measurement Technology and Ground Testing Conference*, no. July: 1–22. doi:10.2514/6.2010-4355.

Lee, Gun Hyee, Young Don Choi, and Seong Ho Han. 2007. "Measurement of Developing Turbulent Flow in a U-Bend of Circular Cross-Section." *Journal of Mechanical Science and Technology* 21 (2). Korean Society of Mechanical Engineers: 348–59. doi:10.1007/BF02916295.

Lin, Chih Hung, and Yuh Ming Ferng. 2014. "Predictions of Hydrodynamic Characteristics and Corrosion Rates Using CFD in the Piping Systems of Pressurized-Water Reactor Power Plant." *Annals of Nuclear Energy* 65: 214–22. doi:10.1016/j.anucene.2013.11.007.

Mazhar, H. 2013. "Flow Accelerated Corrosion in Single and Dual S-Shape Bends under Single and Two Phase Annular Flow Conditions." McMaster University.

Mazhar, H., D. Ewing, J. S. Cotton, and C. Y. Ching. 2016. "Measurement of the Flow Field Characteristics in Single and Dual S-Shape 90?? Bends Using Matched Refractive Index PIV." *Experimental Thermal and Fluid Science* 79: 65–73. doi:10.1016/j.expthermflusci.2016.06.025.

Mazhar, H., D. Ewing, J.S. Cotton, and C.Y. Ching. 2013. "Experimental Investigation of Mass Transfer in 90° Pipe Bends Using a Dissolvable Wall Technique." *International Journal of Heat and Mass Transfer* 65 (October): 280–88. doi:10.1016/j.ijheatmasstransfer.2013.06.001.

Miller, D S. 1971. *Internal Flow*. Cranfield-Bradford: BHRA.

Ohadi, M. M., and E M Sparrow. 1989. "Heat Transfer in a Straight Tube Situated Downstream of a Bend." *International Journal of Heat and Mass Transfer* 32 (2): 201–12. doi:10.1016/0017-9310(89)90168-3.

Ono, A., N. Kimura, H. Kamide, and A. Tobita. 2011. "Influence of Elbow Curvature on Flow Structure at Elbow Outlet under High Reynolds Number Condition." *Nuclear Engineering and Design* 241 (11): 4409–19. doi:10.1016/j.nucengdes.2010.09.026.

Poulson, Bryan. 1993. "Advances in Understanding Hydrodynamic Effects on Corrosion." *Corrosion Science* 35 (1–4): 655–65. doi:10.1016/0010-938X(93)90201-Q.

Poulson, Bryan. 1999. "Complexities in Predicting Erosion Corrosion." *Wear* 233–235 (December): 497–504. doi:10.1016/S0043-1648(99)00235-5.

Poulson, Bryan, and Russell Robinson. 1988. "The Local Enhancement of Mass Transfer at 180° Bends." *International Journal of Heat and Mass Transfer* 31 (6): 1289–97. doi:10.1016/0017-9310(88)90071-3.

Raffel, Markus, Christian E Willert, Steve T Wereley, and Jürgen Kompenhans. 2007. *Particle Image Velocimetry - A Practical Guide*. New York: Springer Berlin Heidelberg.

Röhrig, R., S. Jakirlić, and C. Tropea. 2015. "Comparative Computational Study of Turbulent Flow in a 90° Pipe Elbow." *International Journal of Heat and Fluid Flow* 55: 120–31. doi:10.1016/j.ijheatfluidflow.2015.07.011.

Rowe, M. 1970. "Measurements and Computations of Flow in Pipe Bends." *Jounal of Fluid Mechanic* 43 (4). McMaster University Library: 771–83. doi:10.1017/S0022112070002732.

Rütten, Frank, Matthias Meinke, and Wolfgang Schröder. 2001. "Large-Eddy Simulations of 90° Pipe Bend Flows." *Journal of Turbulence* 2 (July 2015): N3. doi:10.1088/1468-5248/2/1/003.

Rütten, Frank, Wolfgang Schröder, and Matthias Meinke. 2005. "Large-Eddy Simulation of Low Frequency Oscillations of the Dean Vortices in Turbulent Pipe Bend Flows." *Physics of Fluids* 17 (3). doi:10.1063/1.1852573.

Sakakibara, Jun, and Akira Hashimoto. 2010. "Stereo-PIV Study of Turbulent Flow Downstream of a Bend in a Round Pipe." In *APS Division of Fluid Dynamics Meeting Abstracts*. Vol. 1.

Sakakibara, Jun, and Nobuteru Machida. 2012. "Measurement of Turbulent Flow Upstream and Downstream of a Bend in a Round Pipe." *16th International Symposium on Applications of Laser Techniques to Fluid Mechanics* 41702: 1–8.

Sciacchitano, Andrea, and Bernhard Wieneke. 2016. "PIV Uncertainty Propagation." *Measurement Science and Technology* 27 (8). IOP Publishing: 84006. doi:10.1088/0957-0233/27/8/084006.

Smits, Alexander J., Beverley J. McKeon, and Ivan Marusic. 2011. "High–Reynolds Number Wall Turbulence." *Annual Review of Fluid Mechanics* 43 (1). Annual Reviews: 353–75. doi:10.1146/annurev-fluid-122109-160753.

Spedding, P L, E Benard, and G M Mcnally. 2004. "Fluid Flow through 90 Degree Bends." *Dev. Chem. Eng. Mineral Process* 2 (12): 107–28. doi:10.1002/apj.5500120109.

Sudo, K., M. Sumida, and H. Hibara. 1998. "Experimental Investigation on Turbulent Flow in a Circular-Sectioned 90-Degree Bend." *Experiments in Fluids* 25 (1): 42–49. doi:10.1007/s003480050206.

Sudo, K., M.Sumida, and H. Hibara. 2000. "Experimental Investigation on Turbulent Flow in a Circular-Sectioned 180-Degree Bend." *Experiments in Fluids* 28 (1). Springer-Verlag: 51–57. doi:10.1007/s003480050206.

Takamura, Hiroyuki, Shinji Ebara, Hidetoshi Hashizume, Kosuke Aizawa, and Hidemasa Yamano. 2012. "Flow Visualization and Frequency Characteristics of Velocity Fluctuations of Complex Turbulent Flow in a Short Elbow Piping Under High Reynolds Number Condition." *Journal of Fluids Engineering* 134 (10). ASME: 101201–8. http://dx.doi.org/10.1115/1.4007436.

Takeuchi, J, S Satake, N B Morley, T Yokomine, T Kunugi, and M A Abdou. 2005. "PIV Measurements of Turbulence Statistics and near-Wall Structure of Fully Developed Pipe Flow at High Reynolds Number." In *Proc. 6th International Symposium on Particle Image Velocimetry*, 21–23.

Tan, Lei, Baoshan Zhu, Yuchuan Wang, Shuliang Cao, and Kaihong Liang. 2014. "Turbulent Flow Simulation Using Large Eddy Simulation Combined with

Characteristic-Based Split Scheme." *Computers & Fluids* 94. Elsevier Ltd: 161–72. doi:10.1016/j.compfluid.2014.01.037.

Tanaka, Masa-aki. 2009. "Pvp2009-77598 Numerical Investigation of Flow Structure in Pipe Elbow With Large Eddy," 1–10.

Tennekes, Hendrik, and John Leask Lumley. 1972. *A First Course in Turbulence*. MIT press.

Toonder, J. M. J. den, and F. T. M. Nieuwstadt. 1997. "Reynolds Number Effects in a Turbulent Pipe Flow for Low to Moderate Re." *Physics of Fluids* 9 (11). American Institute of Physics: 3398–3409. doi:10.1063/1.869451.

Tropea, C., A.L. Yarin, and J.F. Foss. 2007. "Springer Handbook of Experimental Fluid Mechanics." *AIAA Journal* 46 (10): 2653–55. doi:10.2514/1.38773.

TSI Incorporated. 2012. "Seed Particles for Ldv and Piv Maxi."

Tunstall, M. J., and J. K. Harvey. 1968. "On the Effect of a Sharp Bend in a Fully Developed Turbulent Pipe-Flow." *Journal of Fluid Mechanics* 34 (3): 595. doi:10.1017/S0022112068002107.

van Doorne, C W H, and J Westerweel. 2007. "Measurement of Laminar, Transitional and Turbulent Pipe Flow Using Stereoscopic-PIV." *Experiments in Fluids* 42 (2): 259–79. doi:10.1007/s00348-006-0235-5.

Wang, Jianrong, and Siamack A Shirazi. 2001. "A CFD Based Correlation for Mass Transfer Coefficient in Elbows." *International Journal of Heat and Mass Transfer* 44 (9): 1817–22. doi:10.1016/S0017-9310(00)00222-2.

Wang, Shiming, Cheng Ren, Yangfei Sun, Xingtuan Yang, and Jiyuan Tu. 2016. "A Study on the Instantaneous Turbulent Flow Field in a 90-Degree Elbow Pipe with Circular Section." *Science and Technology of Nuclear Installations* 2016. doi:10.1155/2016/5265748.

Wang, Yan, Quanlin Dong, and Pengfei Wang. 2015. "Numerical Investigation on Fluid Flow in a 90-Degree Curved Pipe with Large Curvature Ratio." *Mathematical Problems in Engineering* 2015. doi:10.1155/2015/548262.

Warner, Scott O, and Barton L Smith. 2014. "Autocorrelation-Based Estimate of Particle

Image Density for Diffraction Limited Particle Images." *Measurement Science and Technology* 25 (6): 65201. doi:10.1088/0957-0233/25/6/065201.

Weske, JR. 1943. "Pressure Loss in Ducts with Compound Elbows." *WASHINGTON*. http://www.stormingmedia.us/32/3201/A320108.pdf.

Wilkin, S J, H S Oates, and M W E Coney. 1983. "Mass Transfer in Straight Pipes and 90o Bends Measured by the Dissolution of Plaster."

Wilson, Brandon M, and Barton L Smith. 2013. "Uncertainty on PIV Mean and Fluctuating Velocity due to Bias and Random Errors." *Meas. Sci. Technol. Meas. Sci. Technol* 24 (24): 35302–35302. doi:10.1088/0957-0233/24/3/035302.

Yarnell, David L. 1937. "Flow of Water through 6-Inch Pipe Bends."

Appendix A

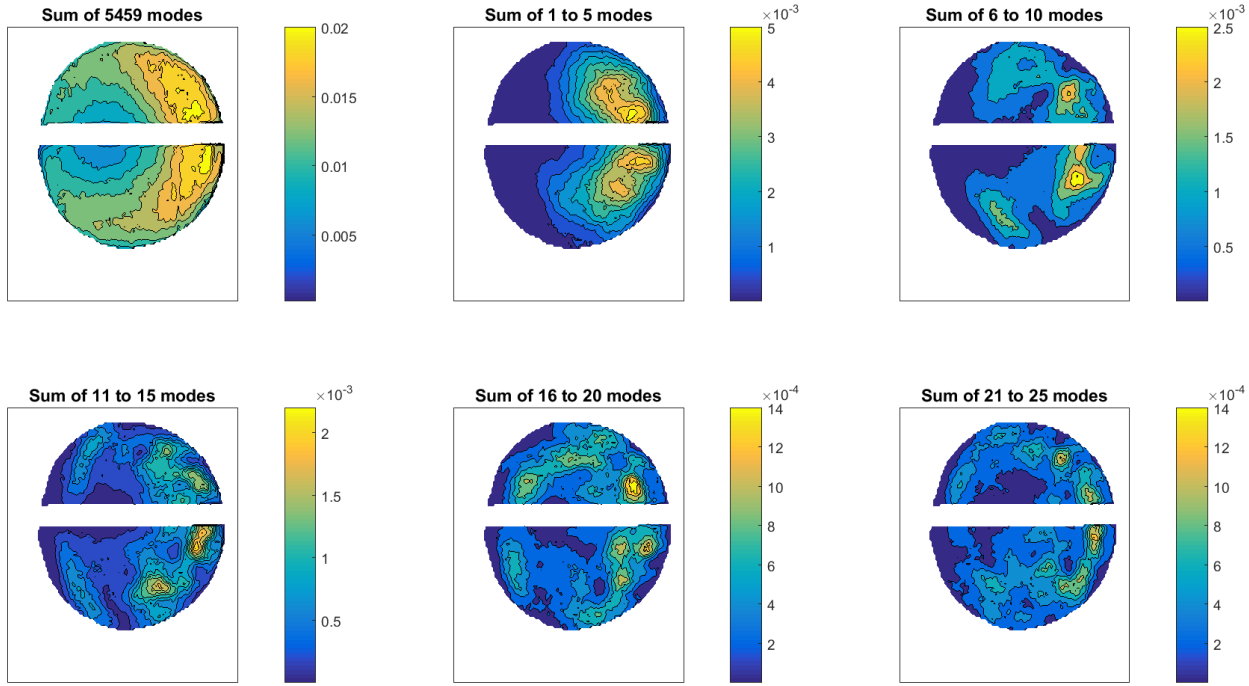

Figure A.1 Reconstruction of Reynolds stress with successive 5 modes at 20° plane

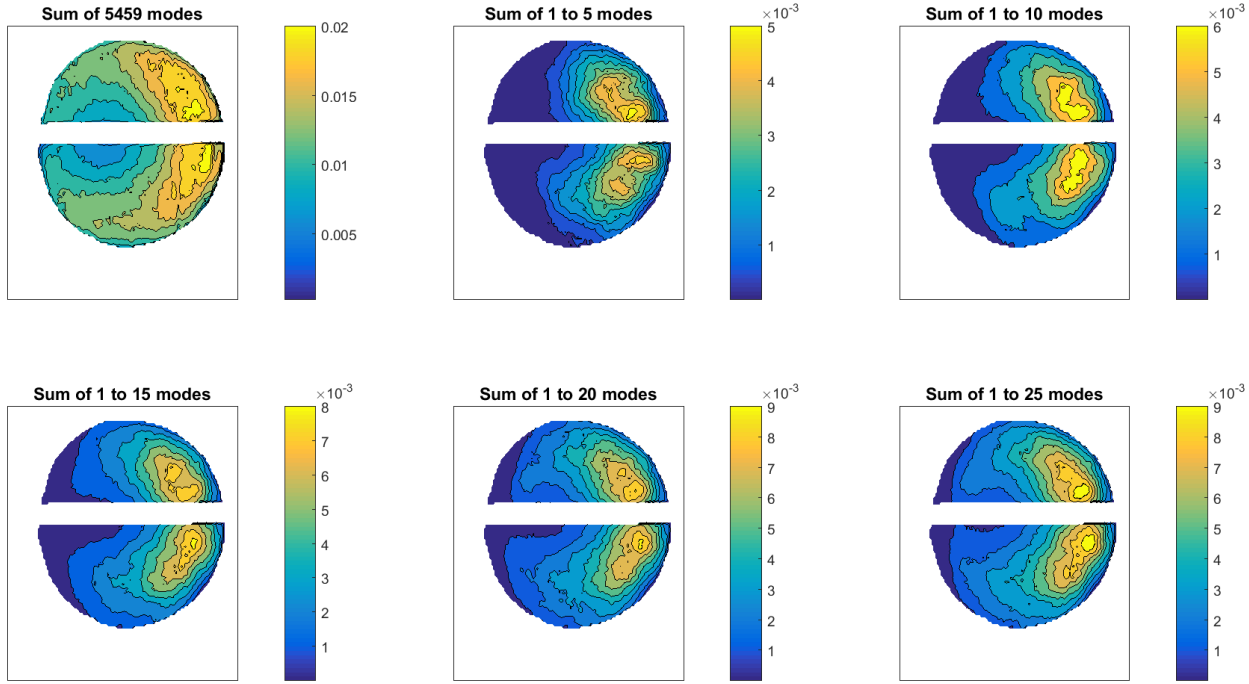

Figure A.2 Reconstruction of Reynolds stress with different number of modes at 20° plane.

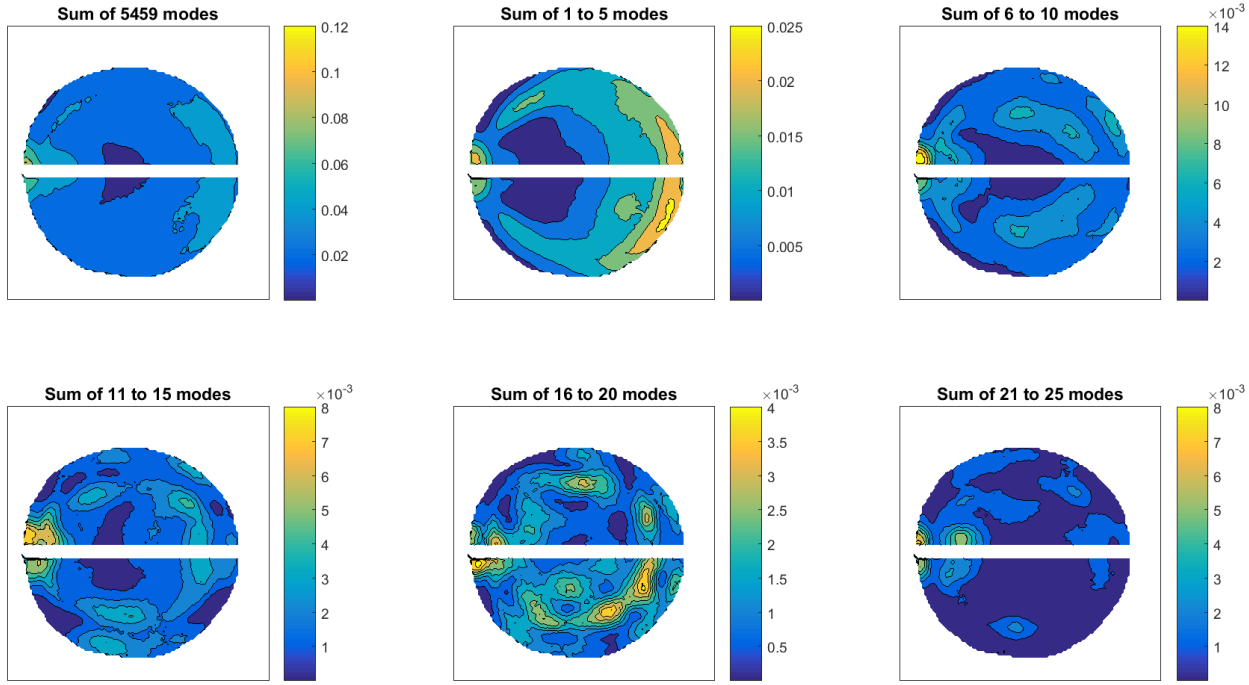

Figure A.3 Reconstruction of Reynolds stress with successive 5 modes at 80° plane

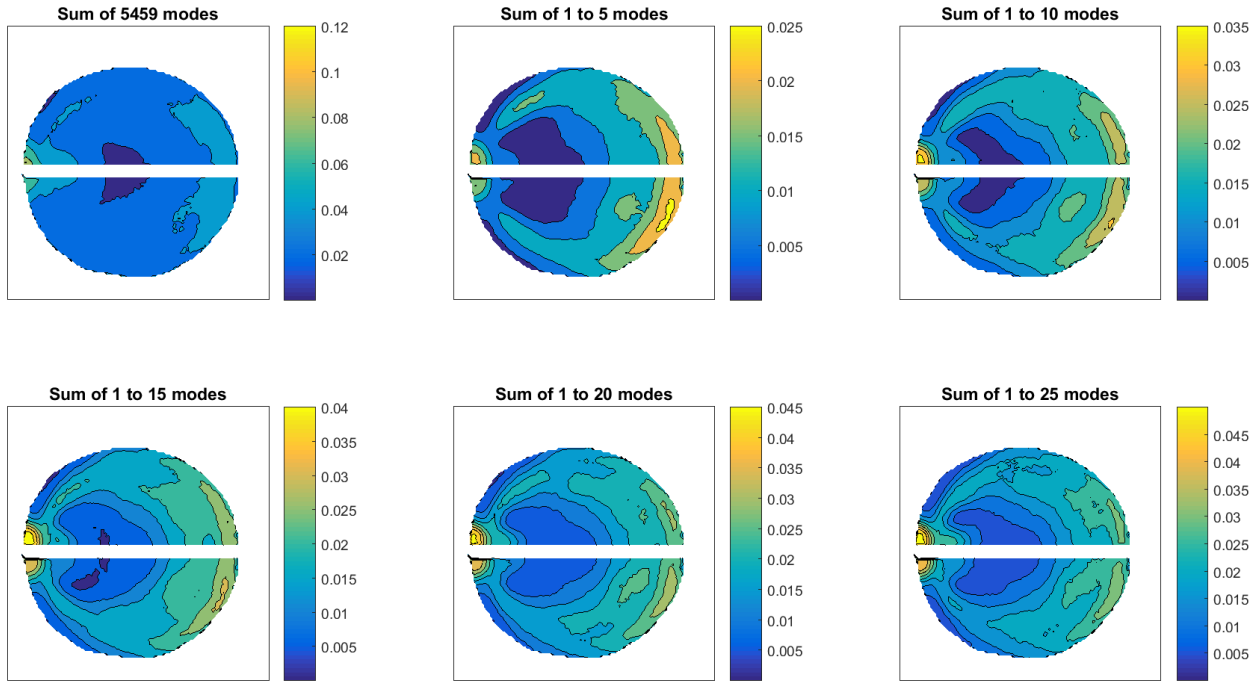

Figure A.4 Reconstruction of Reynolds stress with different number of modes at 80° plane.

Appendix B

The total velocity results for a frequency of 360Hz, corresponding to a St of 6.8, along with contours of magnitude of transverse velocity at the cross-section planes of 0.25D upstream, 20°, 80°, 0.25 D and 1D downstream are shown in Figure B.1 through Figure B.2. The reconstructed flow at the cross sectional plane 0.25D upstream of the bend shows high velocity region moving along the outer wall side. However, a single periodic event is not identified which can be attributed to fluctuation energy contained by wide spectra of frequencies. At the 20° plane, the results show small oscillations of the high velocity region about the symmetry plane. The results show the flow evolution in between two states of low frequency oscillations and no other distinct high frequency (St~0.5) event is found. On the 80° plane, the oscillations are small and the vortices are found tilted in different directions at τ = 0 and 1.76 resulting in full cycle nominal frequency of St ~ 0.25. Also the appearance and disappearance of high velocity in the upper wall can be seen at τ = 0, 1.322, 4.4 which corresponds to St~0.3. The higher frequency reconstruction results at cross sectional plane 0.25D downstream of the bend are shown in Figure B.6 to Figure B.8. The results cover a low frequency oscillation from τ= 0.73 to 6.75. The high velocity regions are present on the side walls and extend up to the inner wall. The change in high velocity region on the upper wall can be seen from τ = 0.3 to 3.1. Similarly, high velocity region on the lower wall changes from τ = 0.59 to 4.4. These change in strength of velocity on side walls corresponds to high frequency events and may be affected by flow separation. At the cross section plane 1D downstream, the total flow is plotted from τ = 0-5.728 (Figure B.9 and Figure B.10). The high velocity sweeping on inner wall side results in domination of two vortices alternatively at higher frequency of around St~ 0.3-0.5.

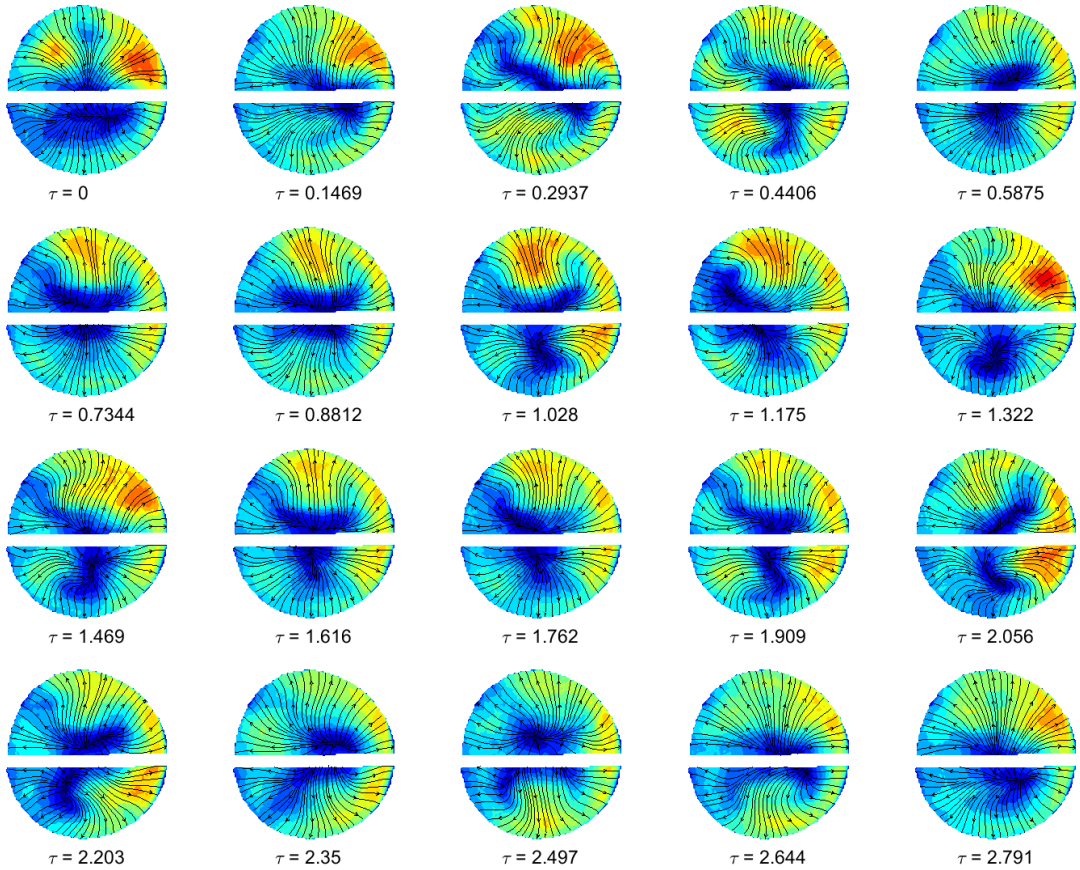

Figure B.1 Reconstruction of total velocity with 6 modes at 0.25D upstream with 360Hz from τ= 0-2.791.

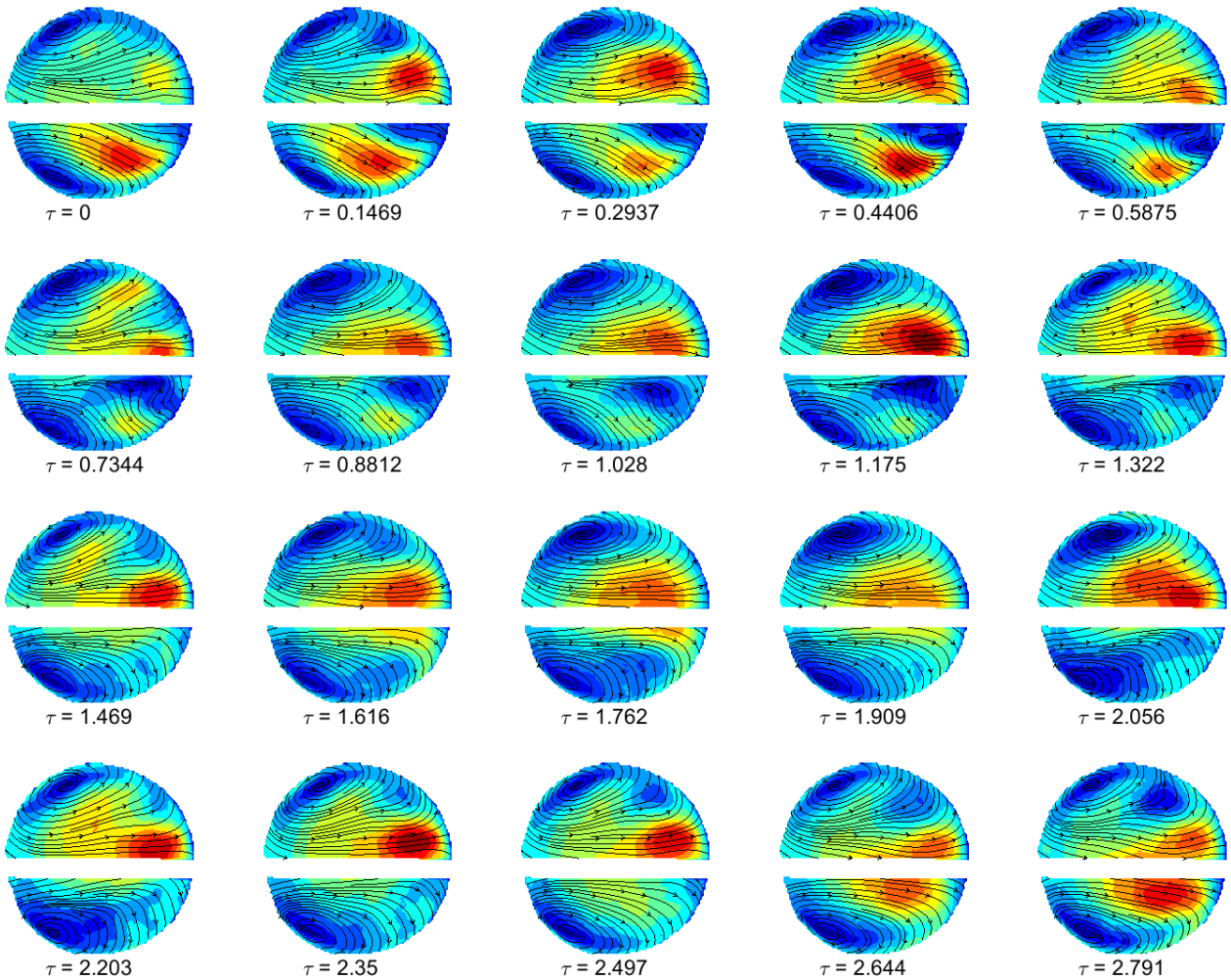

Figure B.2 Reconstruction of total velocity with 6 modes at 20° with 360Hz from τ= 0-2.791.

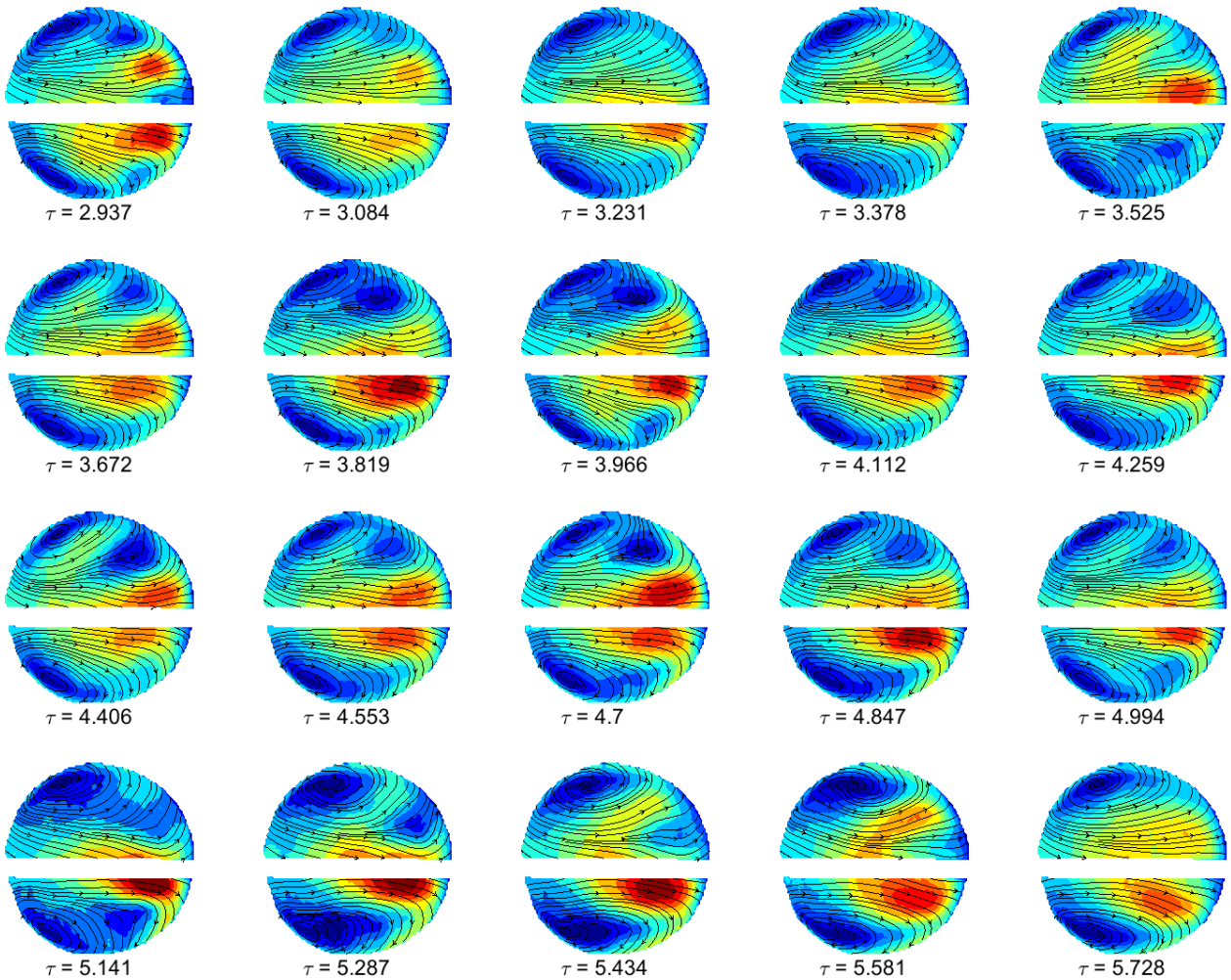

Figure B.3 Reconstruction of total velocity with 6 modes at 20° with 360Hz from τ= 2.937-5.728.

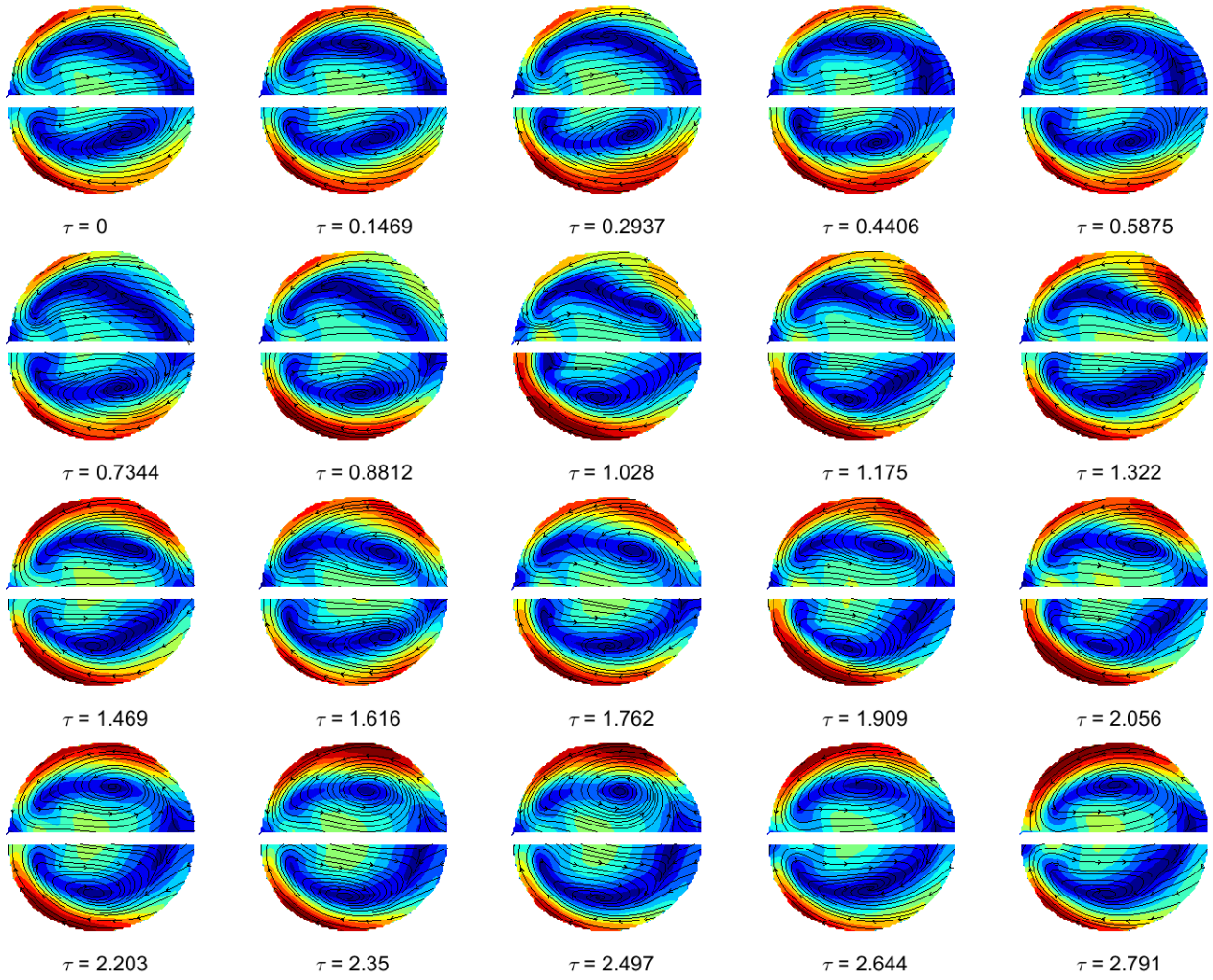

Figure B.4 Reconstruction of total velocity at 80° plane with 6 modes with 360Hz from τ= 0-2.791

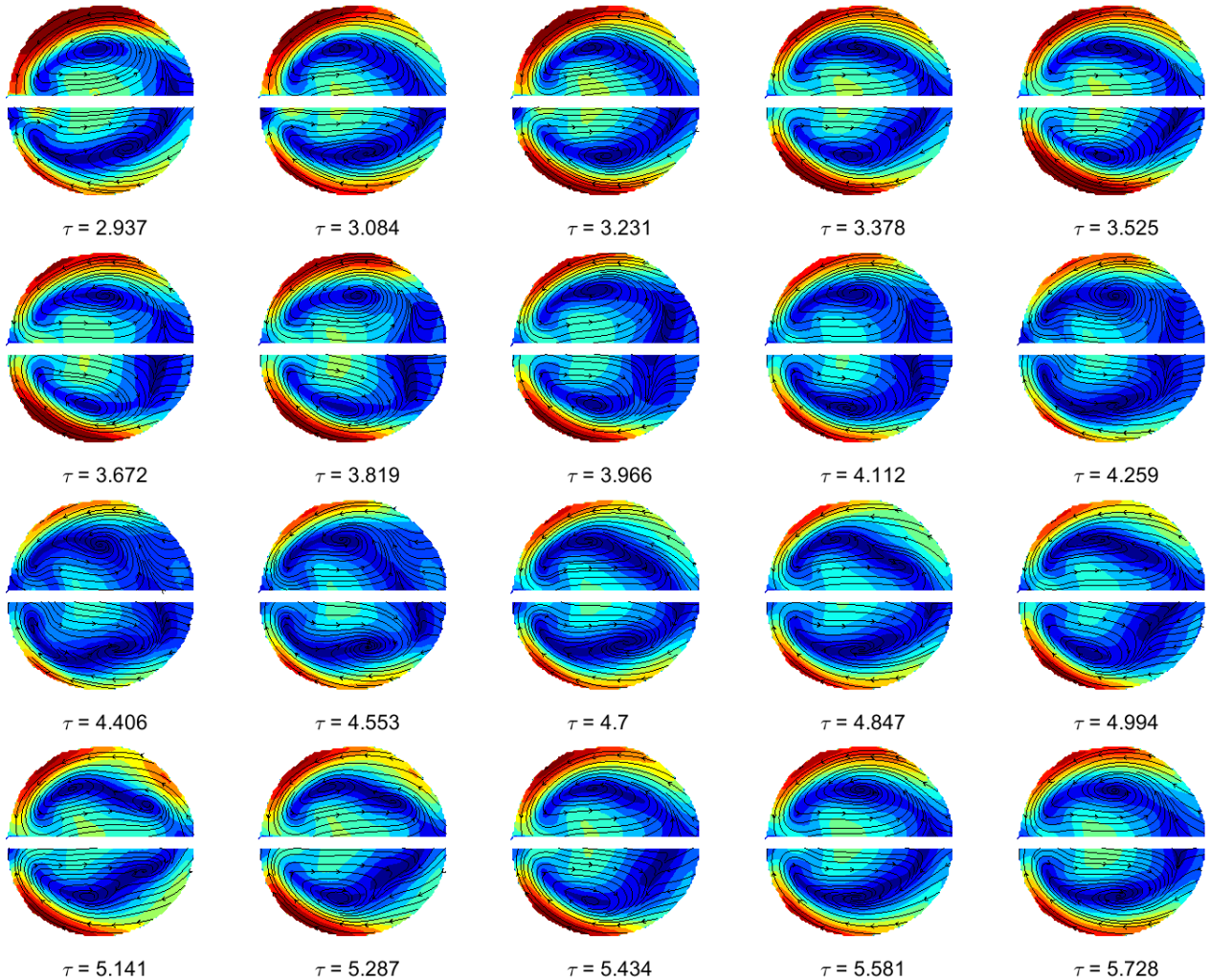

Figure B.5 Reconstruction of total velocity at 80° plane with 6 modes with 360Hz from τ= 2.937-5.728.

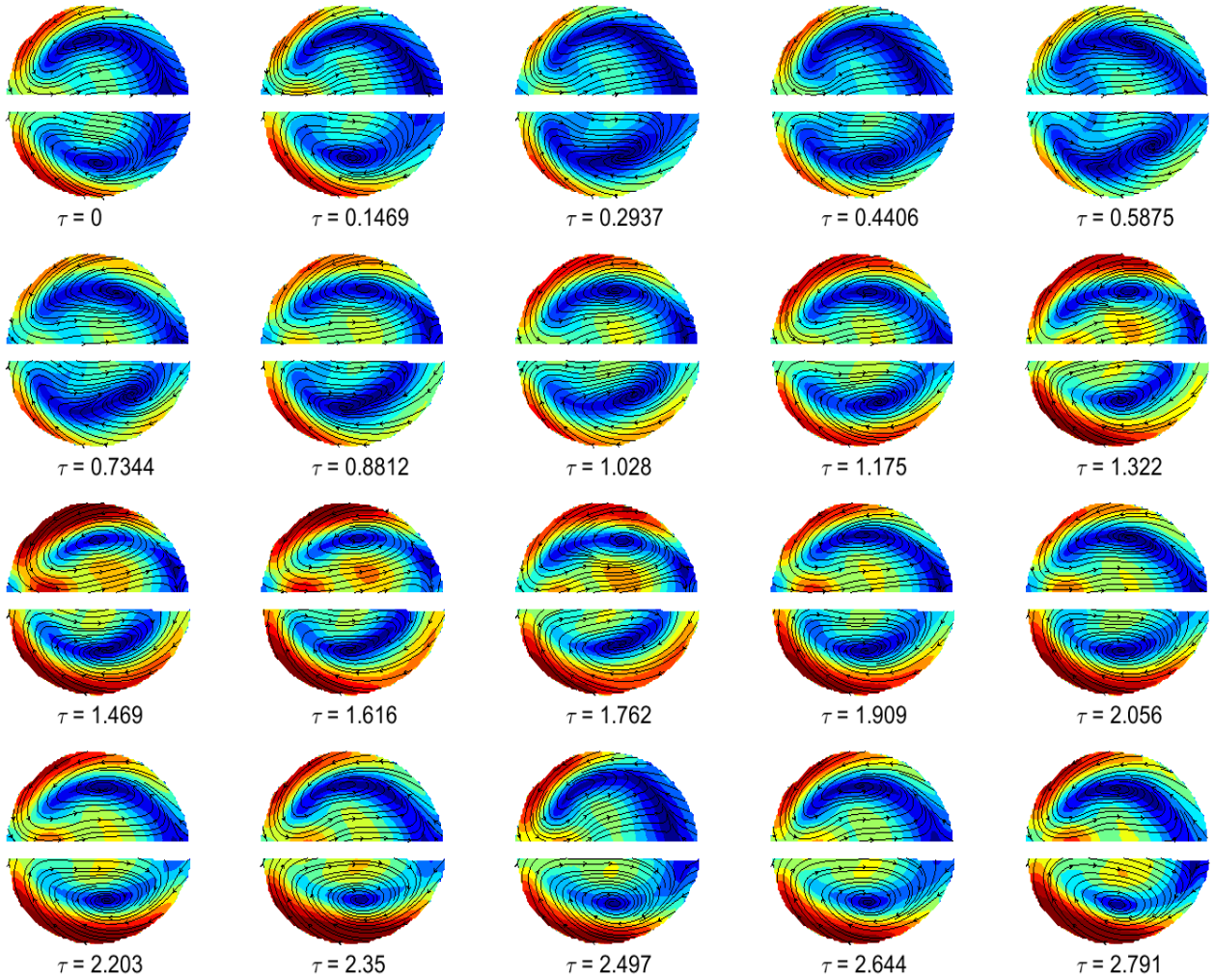

Figure B.6 Reconstruction of total velocity with 6 modes at 0.25D downstream with 360Hz from τ= 0 -2.791.

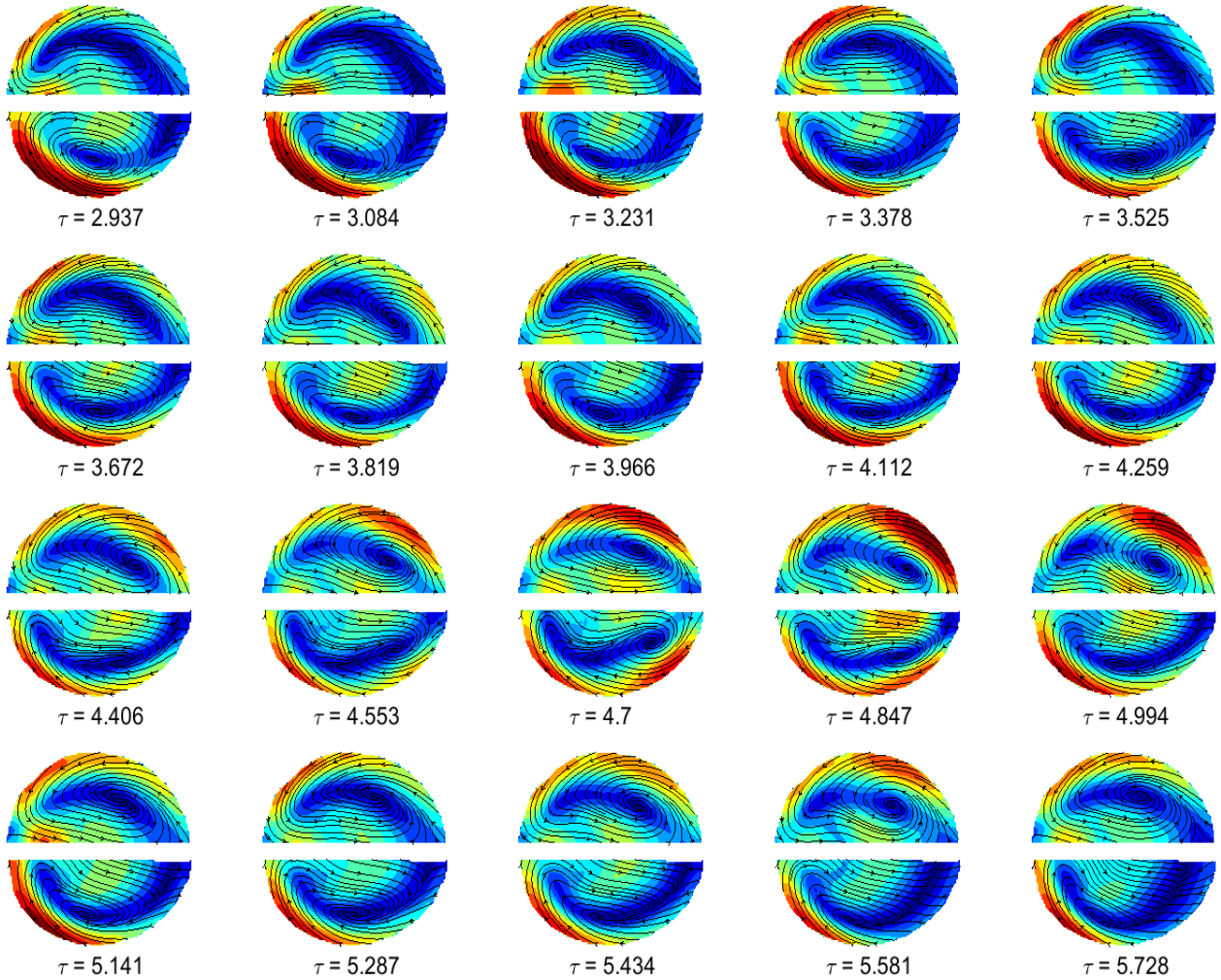

Figure B.7 Reconstruction of total velocity with 6 modes at 0.25D downstream with 360Hz from τ= 2.937-5.728.

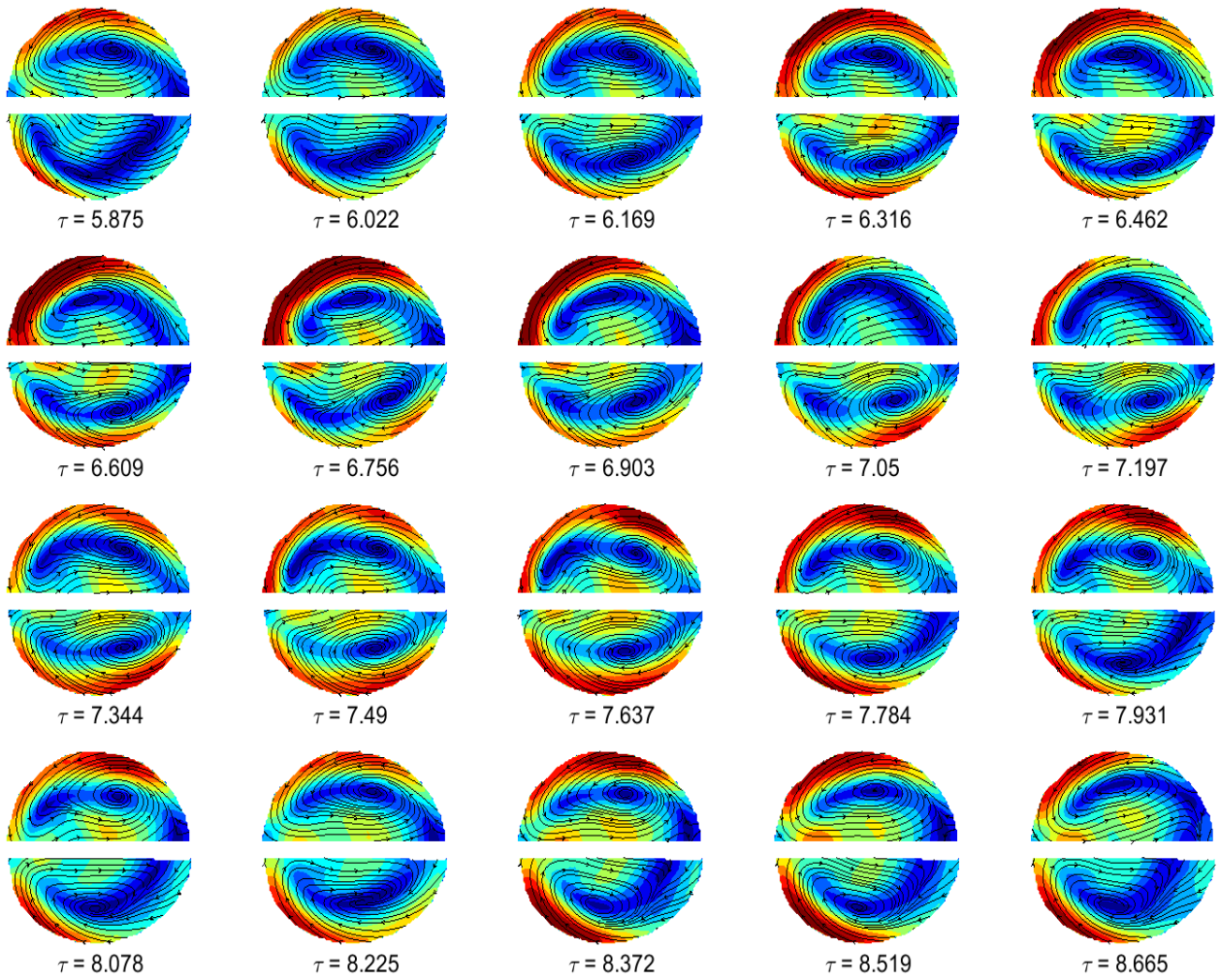

Figure B.8 Reconstruction of total velocity with 6 modes at 0.25D downstream with 360Hz from τ= 5.875-8.665.

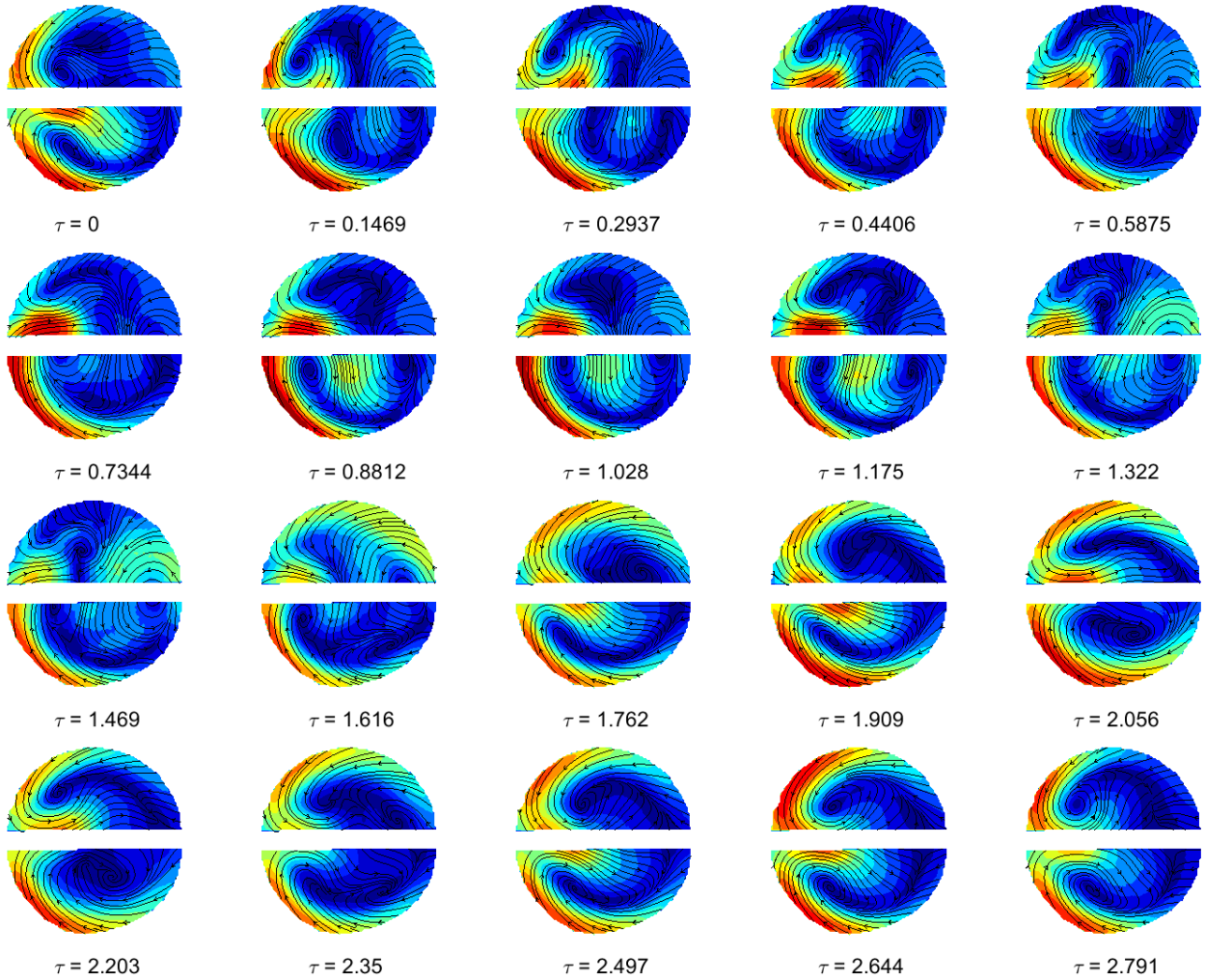

Figure B.9 Reconstruction of total velocity with 6 modes at 1Ddownstream with 360Hz from τ= 0-2.791.

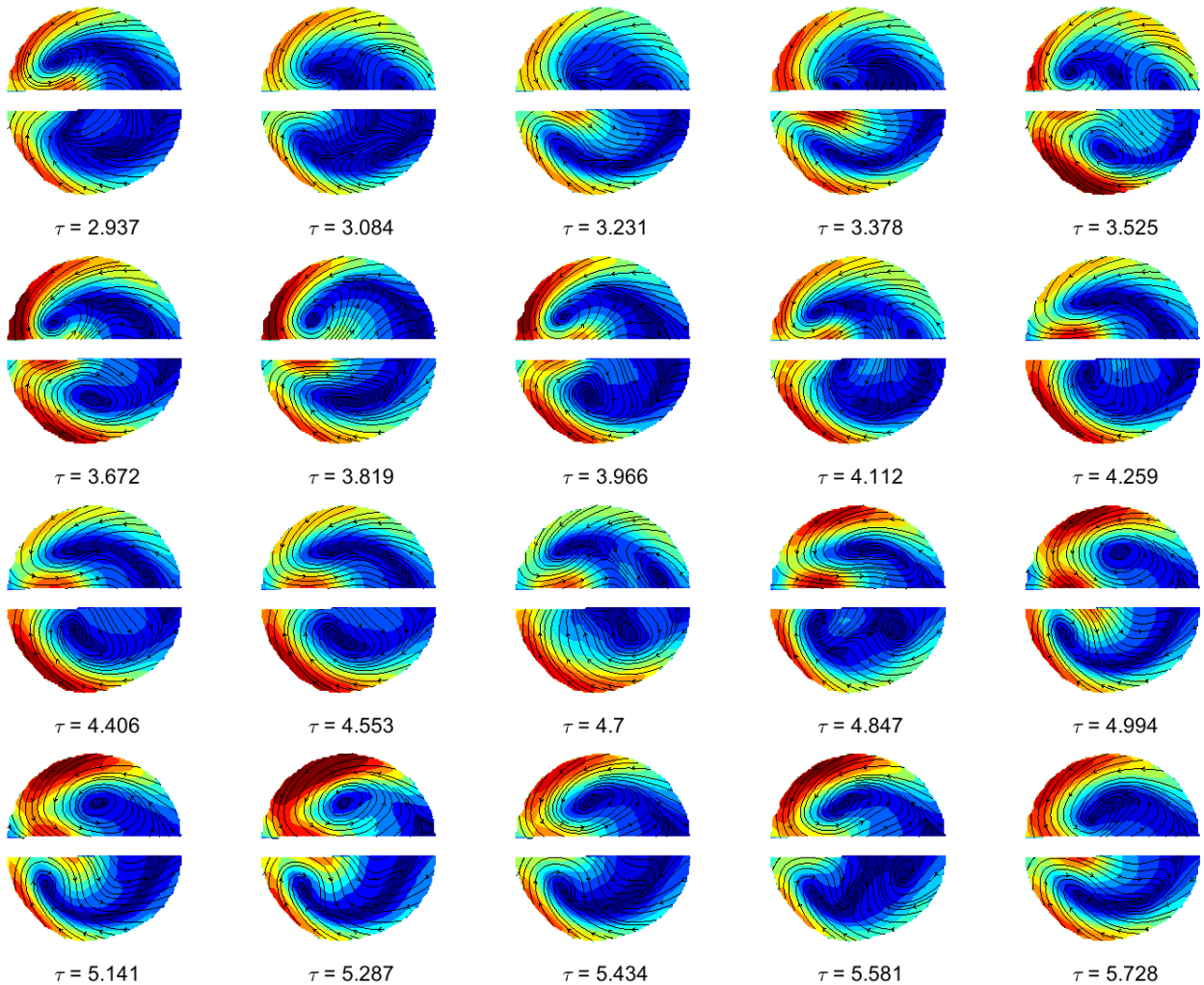

Figure B.10 Reconstruction of total velocity with 6 modes at 1D downstream with 360Hz from τ = 2.937-5.728.

Appendix C

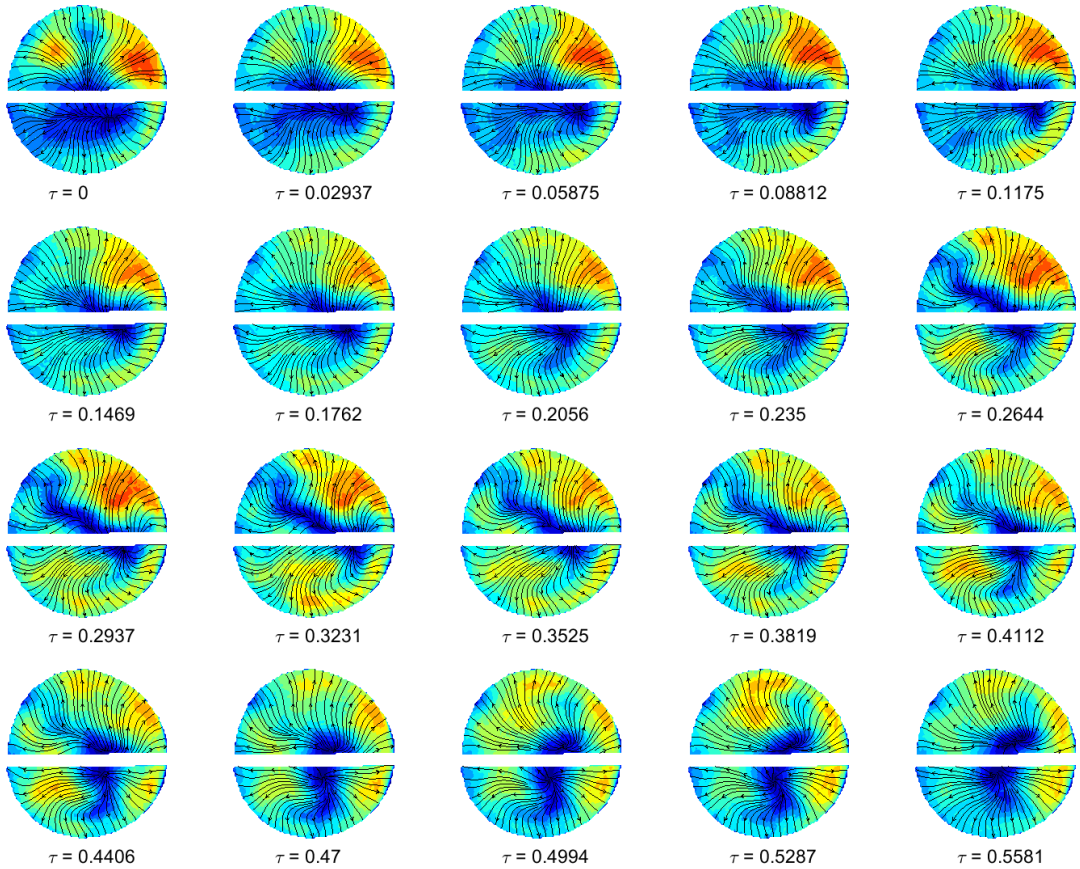

Figure C.1 Reconstruction of total velocity at 0.25D upstream with 1800Hz from tau= 0 -0.558

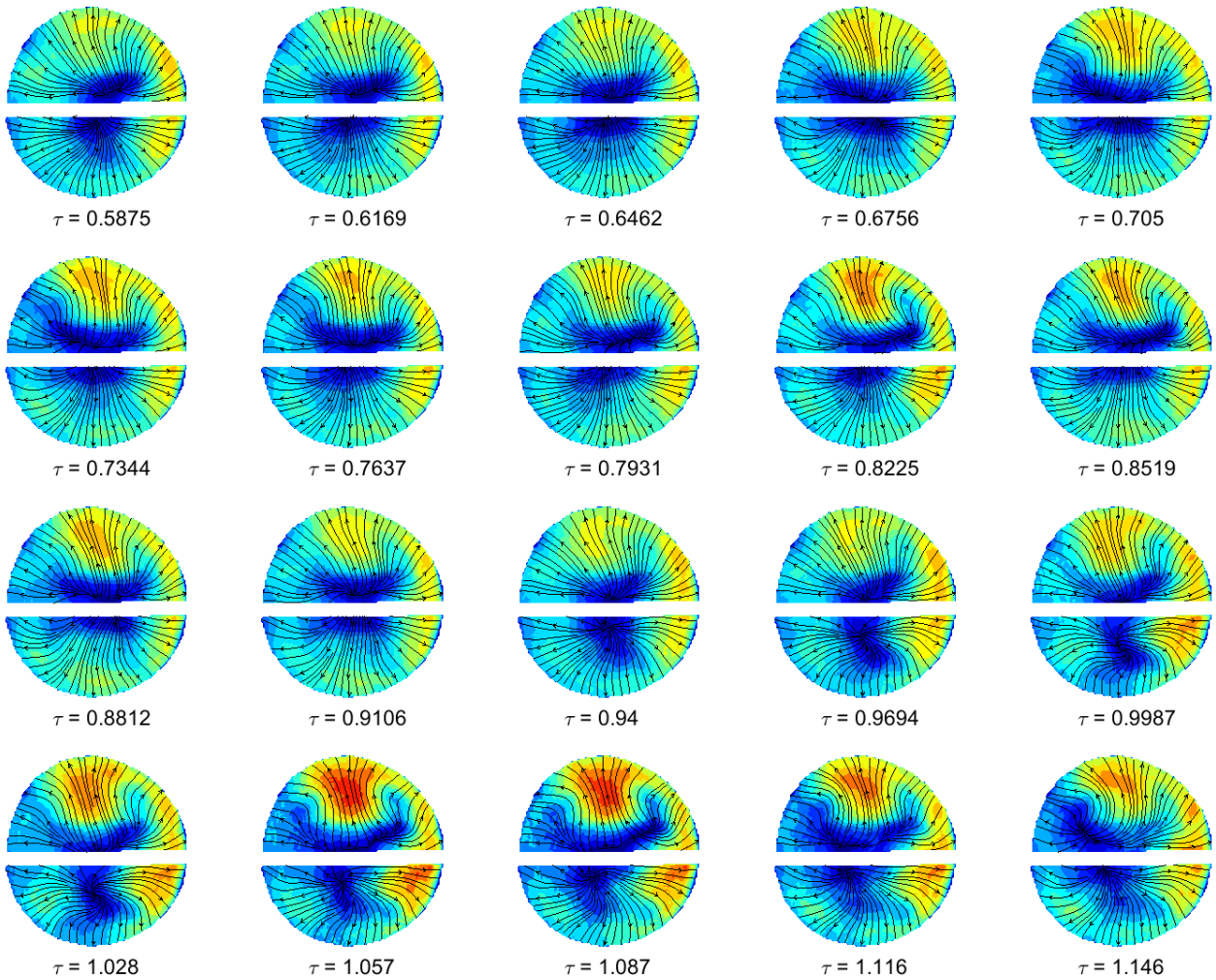

Figure C.2 Reconstruction of total velocity at 0.25D upstream with 1800Hz from tau= 0.587 -1.146

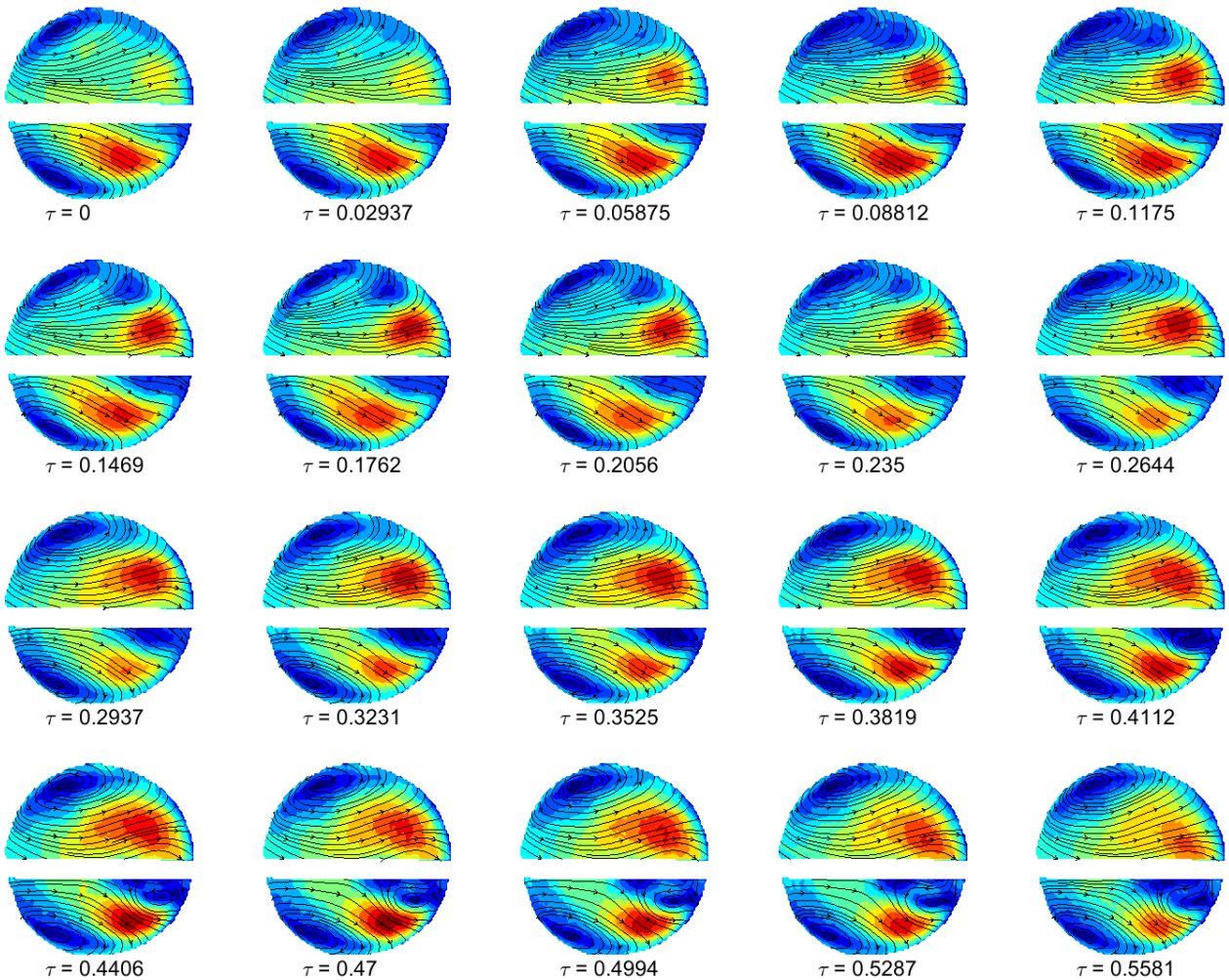

Figure C.3 Reconstruction of total velocity at 20° plane with 1800Hz from tau= 0 -0.558.

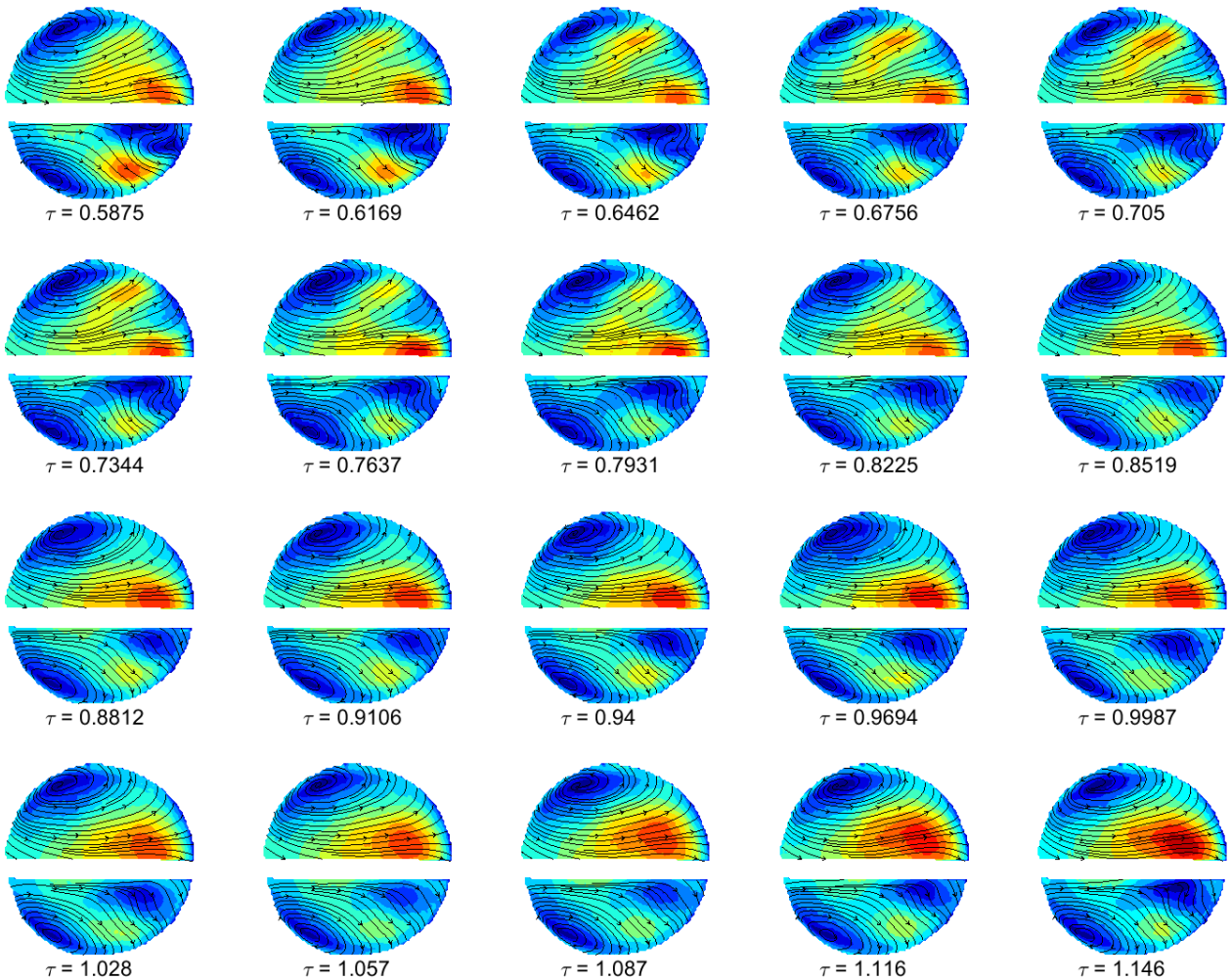

Figure C.4 Reconstruction of total velocity at 20° plane with 1800Hz from tau= 0.587 - 1.146.

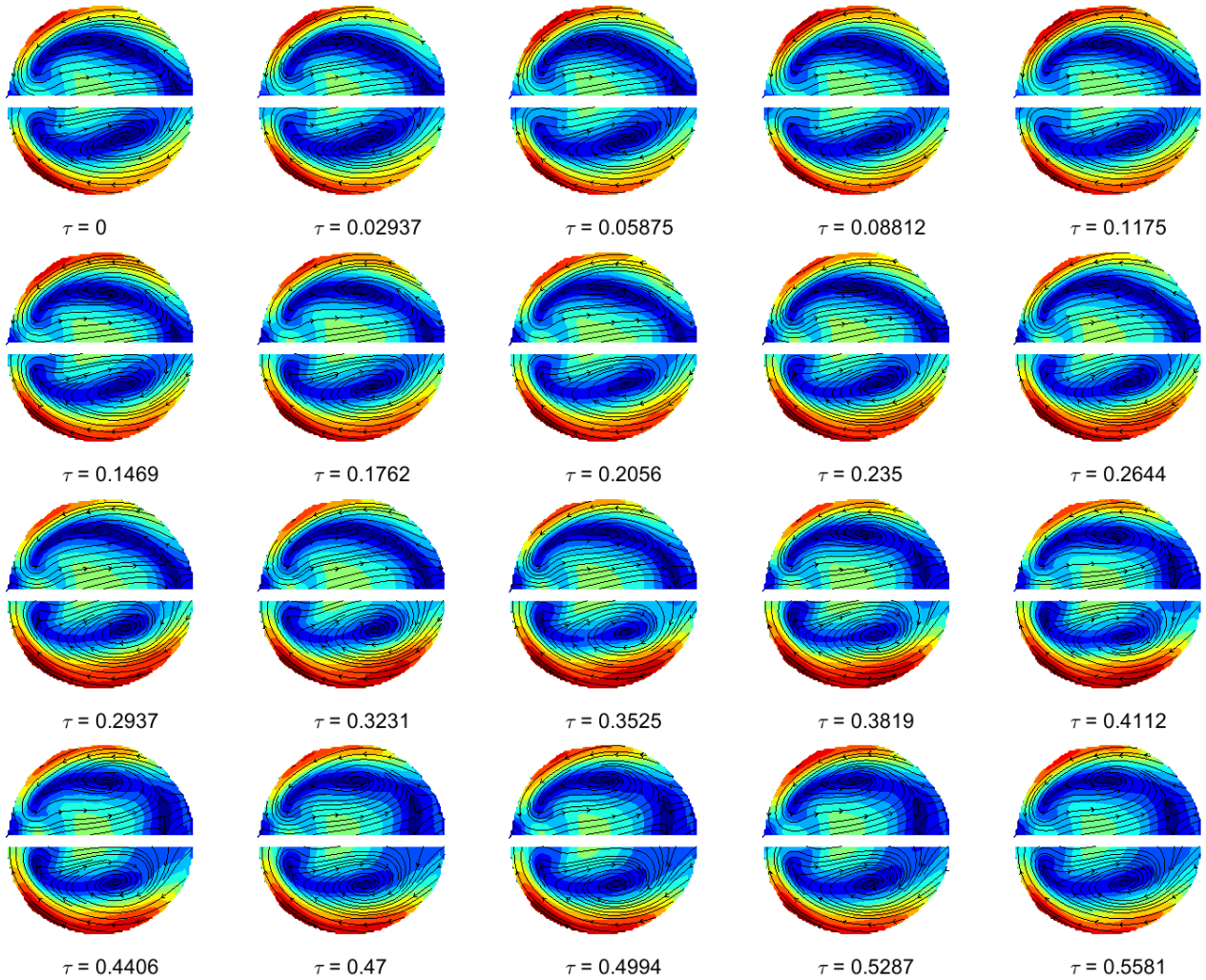

Figure C.5 Reconstruction of total velocity at 80° plane with 1800Hz from tau= 0 -0.558.

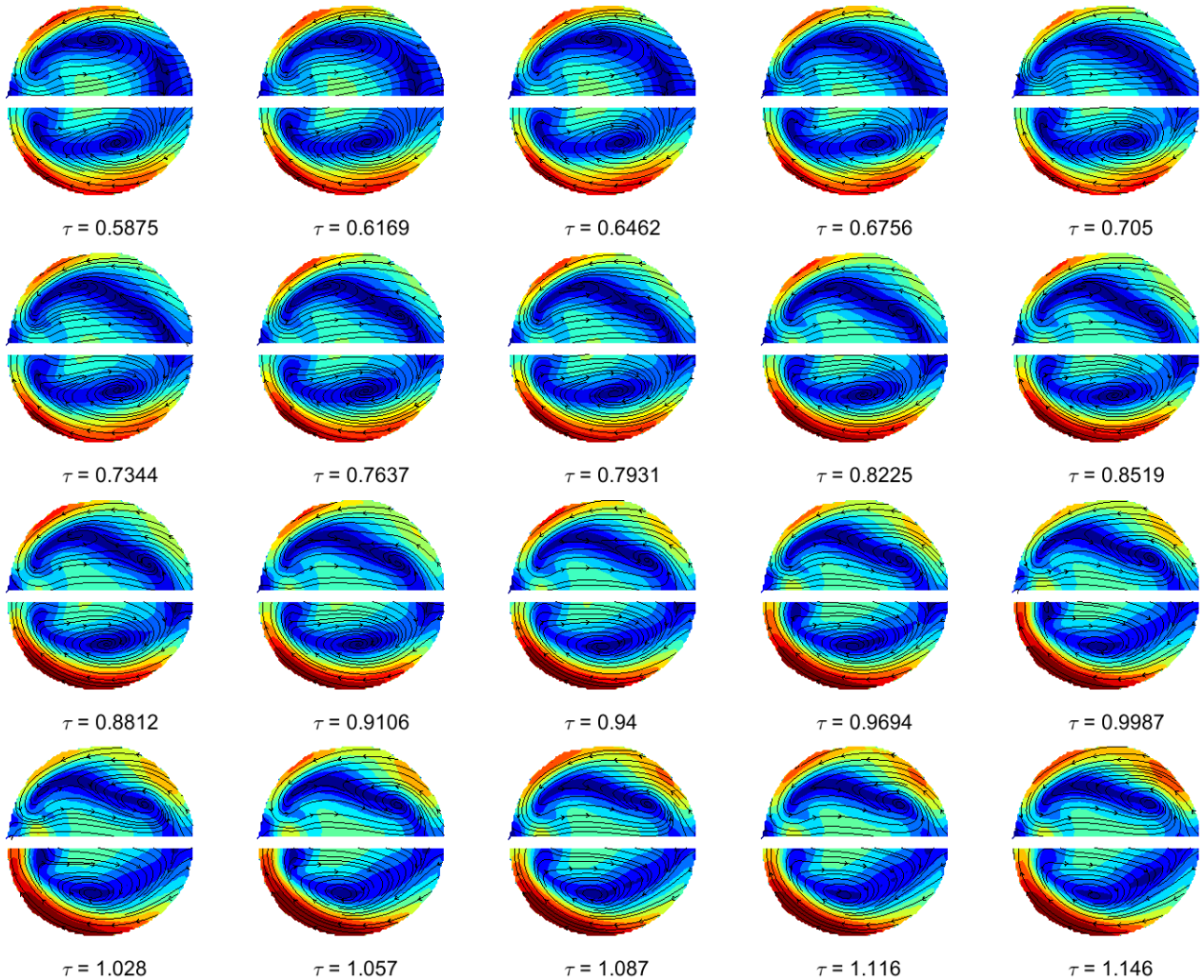

Figure C.6 Reconstruction of total velocity at 80° plane with 1800Hz from tau= 0.587 - 1.146.

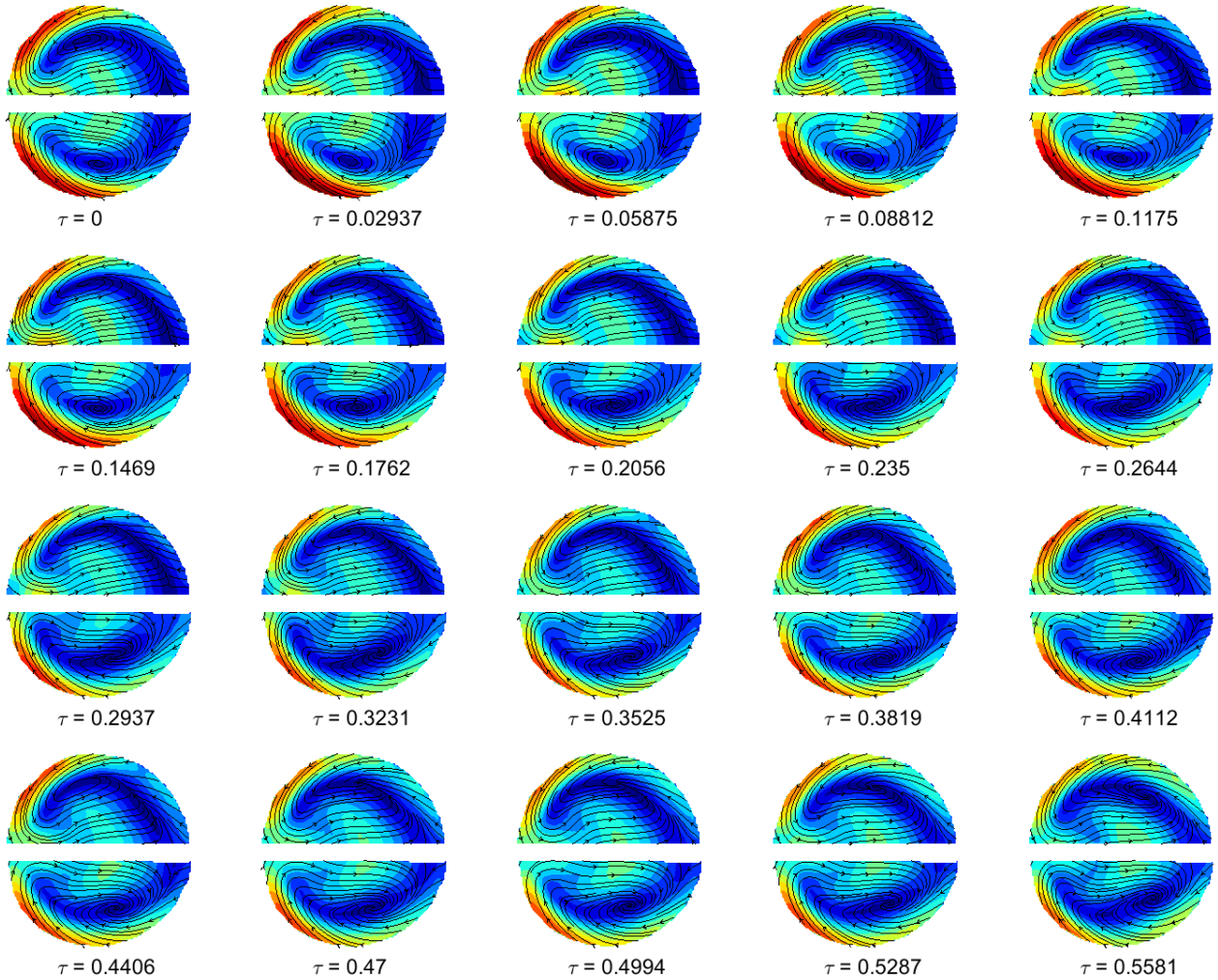

Figure C.7 Reconstruction of total velocity at +0.25D with 1800Hz from tau= 0-0.5581.

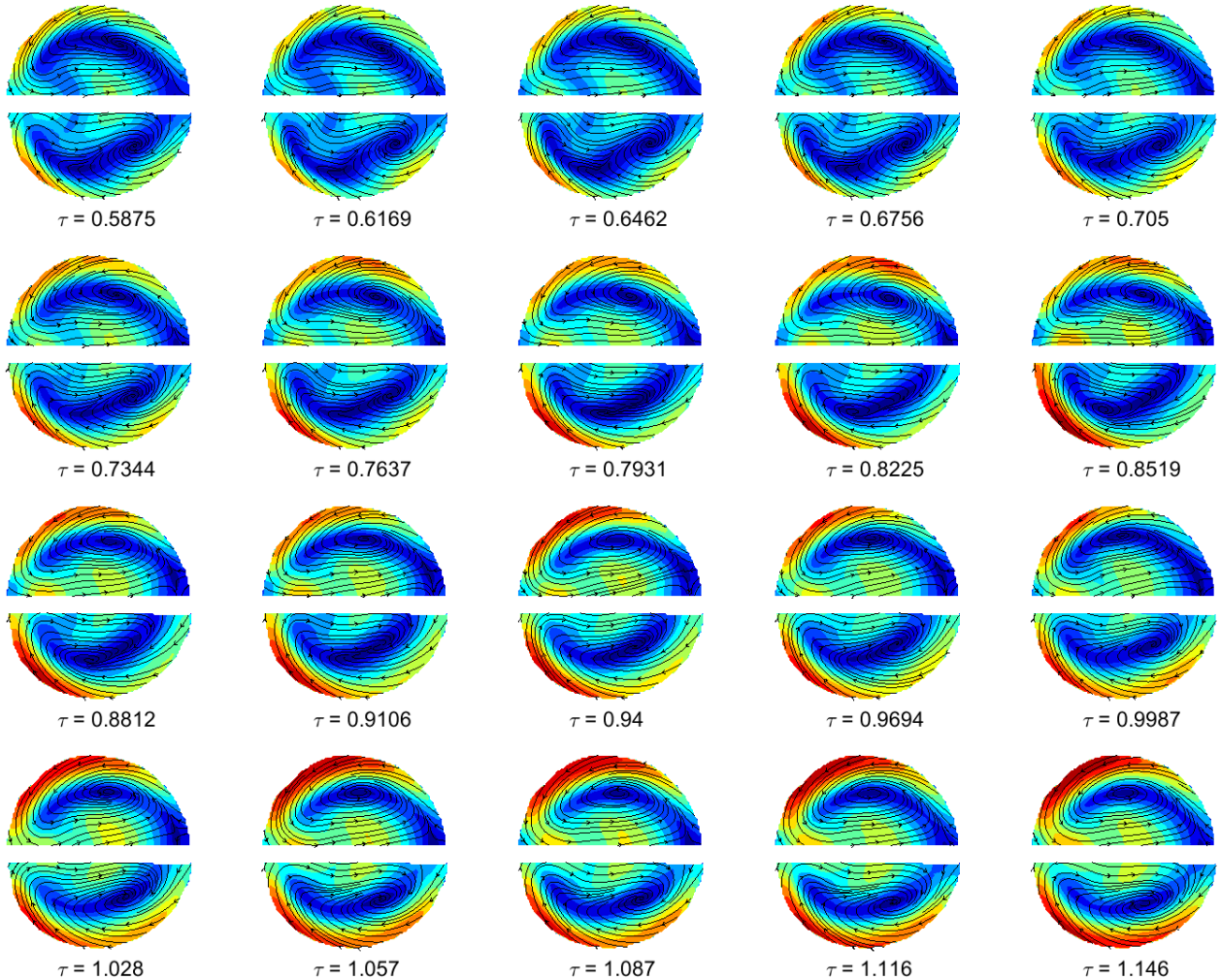

Figure C.8 Reconstruction of total velocity at 0.25D at 1800Hz for tau = 0.5875-1.146.

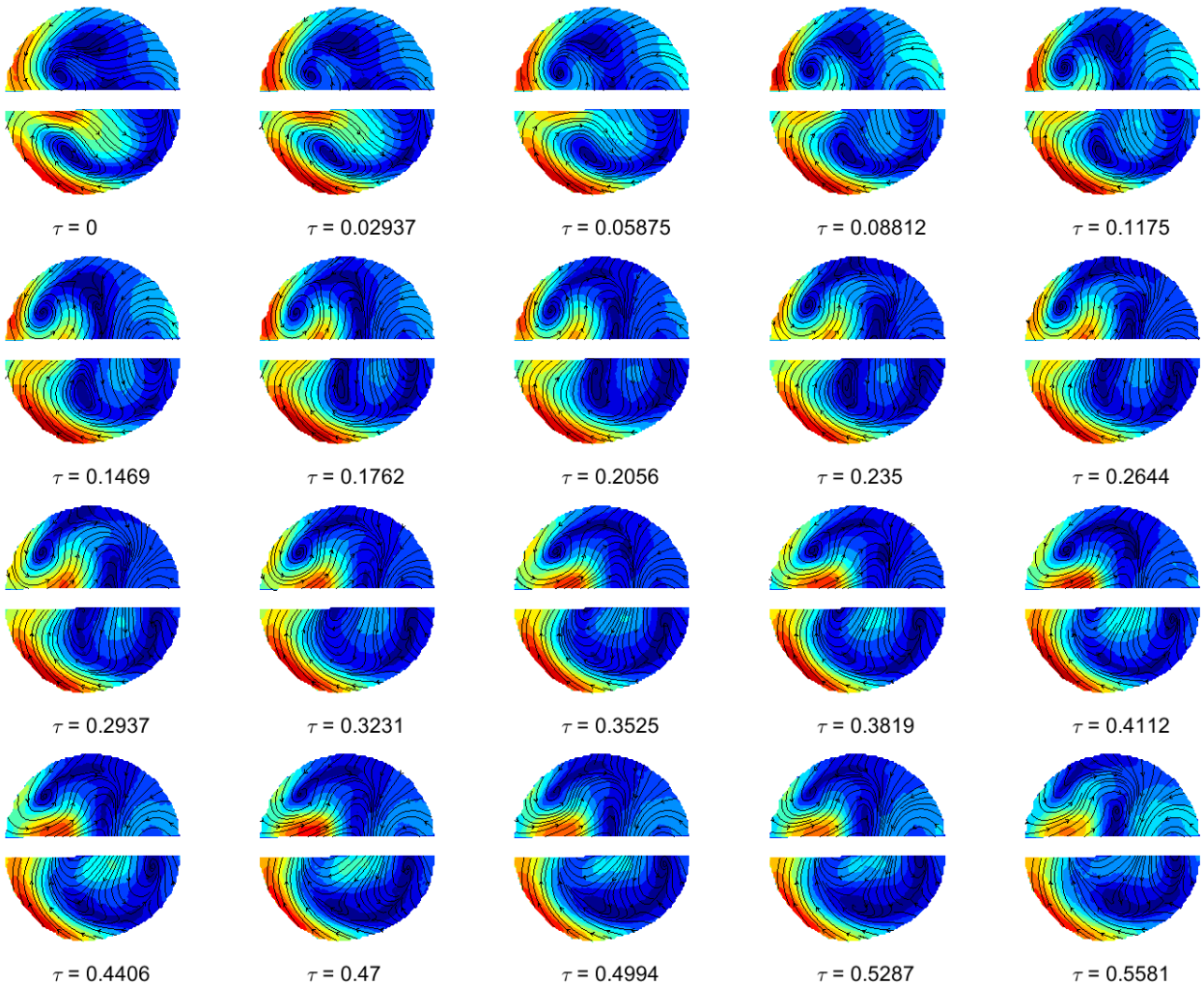

Figure C.9 Reconstruction of total velocity with 6 modes at 1D downstream with 1800Hz from τ = 0-0.5581.

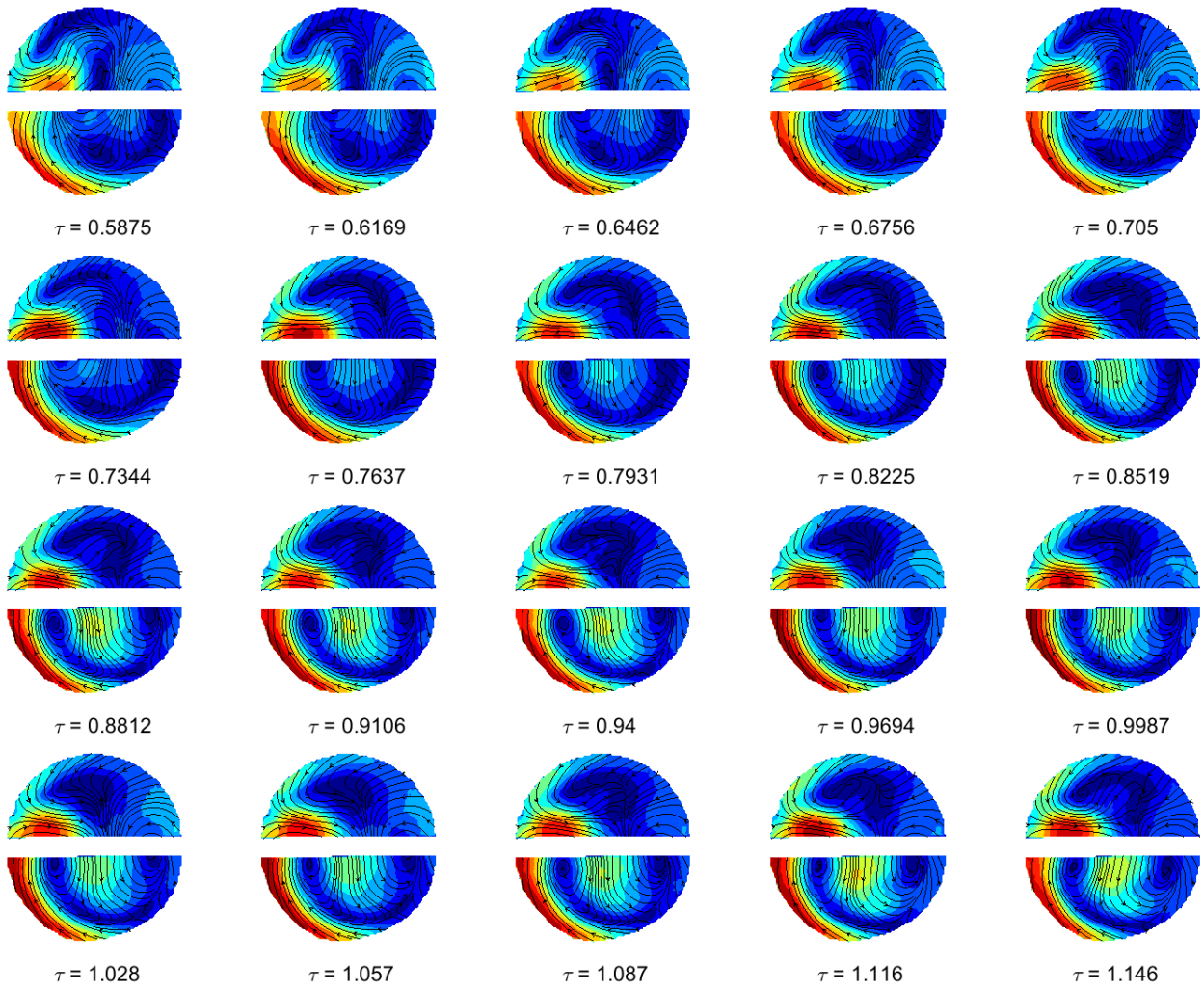

Figure C.10 Reconstruction of total velocity at 1D downstream with 1800Hz from τ = 0.5875-1.146.